# Aspects of Many-Body Systems on a Kagome Lattice: Strong Correlation Effects and Topological Order

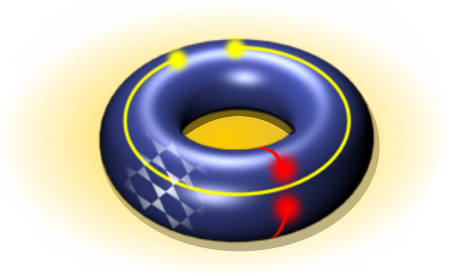

## DISSERTATION

zur Erlangung des akademischen Grades

Doctor of Philosophy
(Ph.D.)

vorgelegt

der Fakultät Mathematik und Naturwissenschaften
der Technischen Universität Dresden

von

Dipl.-Phys. Krishanu Roychowdhury
geboren am 08.07.1987 in Serampore, India

MAX-PLANCK-INSTITUT FÜR PHYSIK KOMPLEXER SYSTEME

Dresden, 2015

Eingereicht am 1. September 2015.

Gutachter:

1. Prof. Dr. Matthias Vojta (Technische Univarsitäte Dresden)
2. Prof. Dr. Roderich Moessner (Max-Planck-Institut für Physik komplexer Systeme)
3. Prof. Dr. Kirill Shtengel (University of California, Riverside)

*To my parents,*
*sister and wife.*

# Aspects of Many-Body Systems on a Kagome Lattice: Strong Correlation Effects and Topological Order

## Abstract

Strongly correlated systems on geometrically frustrated lattices can stabilize a large number of interesting phases that includes a wide array of novel Mott insulators in both bosonic and electronic systems. Charge fluctuations in a Mott insulator are suppressed due to strong mutual interaction among the particles. The presence of frustration is of particular importance as the physics it offers is often rich, unexpectedly complicated, and continues to raise many open questions. The thesis elucidates some of these issues on a kagome lattice where strong interactions among the particles in the Mott phase impose non-trivial local constraints depending on the filling fraction on the lattice. These Mott insulators, in addition to featuring unusual magnetic and/or charge ordering, can also harbor topologically ordered states of quantum matter, e.g., resonating valence bond liquids [Ande 73] realized in certain quantum dimer models on non-bipartite lattices [Moes 01a]. The dimer models can be regarded as low-energy effective theories for different types of bosonic models in the strong-coupling limit. Exploring this connection is a central theme of this thesis with the aim of realizing novel strongly correlated ground states. Past studies of these models have revealed the existence of various ordered and disordered phases with distinct signatures [Moes 01a, Ralk 05, Misg 08]. Among these low-energy phases, the presence of a stable topological liquid at a particular point, known as Rokhsar-Kivelson point [Rokh 88], in the phase diagram is notable.

The classical versions of the dimer model are also known to have garnered a vast interest in various fields ranging from problems of pure mathematical origin to ones in physical chemistry as well as statistical physics. Pioneered by Kasteleyn [Kast 61], several analytical works came forward to exactly calculate the partition function of the problem from which other physical observables can be derived. Classical numerical methods are extensively applied to these models to verify the analytical predictions. We introduce a new classical algorithm here to compute the correlation functions of a classical dimer model on a square (bipartite) and a triangular (non-bipartite) lattice based on a tensor network construction. The method, called tensor network renormalization group, turns out to be a powerful tool for simulating short-ranged gapped systems as inferred from our results benchmarked against the classical Monte-Carlo technique and compared with past analytical studies [Fend 02]. One should note that the quantum dimer model at the Rokhsar-Kivelson point can also be described as an infinite temperature canonical ensemble of classical dimers because of the particular structure of the ground state which is an equal weight superposition in the configuration manifold.

The geometry of the lattice plays a pivotal role in deciding the nature of the phases that arise in the dimer models. Many physical properties of the dimer liquid phase can be extracted in the simple classical setting which certainly allows for a deep understanding of the classical models to be developed. The liquid phase is gapped on non-bipartite lattices and gapless on bipartite lattices, which is reflected in the decay of correlation functions with spatial distances. In general on non-bipartite lattices, the topological nature of the dimer

liquid is characterized by a $\mathbb{Z}_2$ topological order which survives even when the model is perturbed away from the Rokhsar-Kivelson point [Moes 01a]. Stability of this liquid phase not only depends on the lattice geometries but notably on dimer concentrations also. In this context, we focus on a particular variant of the dimer model on a triangular lattice which is known as the quantum fully packed loop model. The model is composed of nonintersecting closed loops made of dimers and governed by the same Hamiltonian as the quantum dimer model. The loop model provides an effective low-energy description of a strongly correlated bosonic system at $1/3$ filling on the kagome lattice. The corresponding Bose-Hubbard Hamiltonian consists of nearest-neighbor hopping and all possible repulsive interactions within a hexagonal plaquette. Conspicuous features of the zero-temperature phase diagram for this model include (i) presence of a stable $\mathbb{Z}_2$ liquid even without any Rokhsar-Kivelson potential term (in distinction to the standard quantum dimer model [Moes 01a]), and (ii) an unconventional phase transition from the liquid phase to a novel crystalline phase that has nematic order (dubbed *lattice nematic*). For a deeper understanding of the physics, a mapping to an Ising gauge theory is presented. The gauge theoretic description provides a useful way to predict the nature of the quantum phase transition to lie in the $O(3)$ universality class.

Finally a fermionic model at the same $1/3$ filling is considered in which the ground state exhibits a number of exotic local orderings resulting from the spin-charge interplay of electrons. The Hamiltonian comprises nearest-neighbor hopping, strong on-site Coulomb interaction, and repulsive interaction terms only between nearest-neighbors. In the strong correlation limit, this fermionic problem maps to a two-color fully packed loop model – a model in which the loop segments carry an additional quantum number as *color* on a honeycomb lattice. The effective theory is governed by coherent three-particle ring exchanges and nearest-neighbor antiferromagnetic spin exchanges. The competition between these two leads to a phase diagram composed of a novel plaquette ordered state (known as the *plaquette phase*) that undergoes phase transition to a new kind of charge ordered state which we call a *short loop phase*. From our numerical analysis, we conclude that the plaquette phase features an unusual antiferromagnetic order with gapless spin excitations while the charge-ordered state is subjugated by spin fluctuations of localized electrons arranged in small hexagonal loops on the kagome lattice.

# List of publications

- *$\mathbb{Z}_2$ topological liquid of hard-core bosons on a kagome lattice at $1/3$ filling.*
  — **Krishanu Roychowdhury**, Subhro Bhattacharjee, and Frank Pollmann,
  Physical Review B 92, 075141, (2015).

- *Tensor renormalization group approach to classical dimer models.*
  — **Krishanu Roychowdhury**, and Ching-Yu Huang,
  Physical Review B 91, 205418, (2015).

- *Interplay of charge and spin fluctuations of strongly interacting electrons on the kagome lattice.*
  — Frank Pollmann, **Krishanu Roychowdhury**, Chisa Hotta, and Karlo Penc,
  Physical Review B 90, 035118, (2014).

- *Pseudo-spin half metals on the surface of 3D topological insulators.*
  — Sthitadhi Roy, **Krishanu Roychowdhury**, and Sourin Das,
  arXiv:1502.07871.

- *Doping effects on the magnetic frustration in the honeycomb iridates.*
  — Sujit Das, Er Jia Guo, and **Krishanu Roychowdhury**,
  arXiv:1506.08279.

- *Entanglement enabled polarised intensity interferometry : a quantum Hall realization.*
  — **Krishanu Roychowdhury**, Disha Wadhawan, Poonam Mehta, Biswajit Karmakar, and Sourin Das,
  *in submission*.

- *Transport signatures of ground state quantum fidelity*
  — Sthitadhi Roy, **Krishanu Roychowdhury**, and Sourin Das,
  *in submission*.

- *Two-particle spin Aharonov-Bohm effect : a spin Hall realization.*
  — Disha Wadhawan, **Krishanu Roychowdhury**, Poonam Mehta, and Sourin Das,
  *in submission*.

# Contents

# Chapter 1

# Introduction

The physics of strongly correlated systems is a plentiful source of challenging puzzles among which the properties of Mott insulators [Mott 49, Bran 76] cultivate a wide interest among condensed matter researches. A Mott insulating state in an electronic system arises by suppressing charge fluctuations in a metal when inter-particle Coulomb repulsion becomes very high compared to the kinetic energy of the conduction band electrons, leading to the formation of localized spin moments [Milo 89]. A bosonic version of the problem introduced by Fisher et al. [Fish 89] has become quite interesting in context of various cold-atom experiments and quantum magnets. On a lattice, the bosonic system is in a superfluid phase if the kinetic energy of the particles overpowers the on-site interaction resulting in delocalization of the bosons. In the limit of strong interaction, the particles get localized to the lattice sites forming a bosonic Mott insulator. Furthermore, in the phase diagram, this insulating state appears to be fragmented into lobes [Fish 89], each one corresponding to a fixed integer filling of bosons per site.

Certain lattice geometries provide additional intricacies rendering the situation more intriguing on frustrated lattices. These are the lattices where the structure leads to competition of interactions and the energy cannot be minimized globally. As a result, several exotic phases can be realized on frustrated lattices including so-called *quantum spin liquid* [Ande 73, Bale 10]. The Mott insulating state on such a lattice can appear even at arbitrary rational filling fractions $p/q$ of bosons whichever is commensurate with the lattice geometry. For $p < q$, however, stability of the Mott state demands long range interactions to be taken into account [Bale 05]. In this thesis, we specialize on bosonic Mott insulators at certain specific fractional fillings which can be realized on a kagome lattice geometry. The filling fractions of interest are $1/6$, $1/3$ and $1/2$ which will be discussed in details in the following chapters with specific attention to the one-third case for reasons to be clear later. The cases of fractional fillings are in general quite fascinating since the resulting insulating states are reminiscent of various valence bond crystals that appear in the low-energy sector of quantum dimer models (QDMs) [Rokh 88, Moes 01a]. These models are regarded as potential candidates to feature the aforementioned spin liquid states. In the past few decades, they have been paid particular attention for offering exciting new physics when investigated in context of high-$T_c$ superconductors (SC) [Bedn 86] — a novel state observed in the family of doped cuprates [Armi 10, Plak 10].

The theoretical attempts and advancements to describe this new superconducting state started with Anderson's early work on resonating valence bond (RVB) liquids [Ande 73, Ande 97, Ande 04] — a coherent superposition of singlet-bond states, each composed of nearest neighbor spin singlets with short-ranged correlations. Building upon these ideas, Rokhsar and Kivelson later constructed a QDM Hamiltonian [Rokh 88, Kive 87] on a square lattice to reveal the existence of a novel dimer liquid in a fine-tuned situation and with *deconfined* excitations. The dimers were representatives of short-ranged singlets and the quasiparticles in the liquid state were found to carry quantum numbers that are fractions of an electron [Ande 87a, Kive 87]. They are called *spinon* – quasiparticles with spin $1/2$ but no charge and *holon* – quasiparticles with charge $e$ but no spin [Ande 87b, Wen 02]. The low-energy dynamics of the model (QDM) is described by a compact quantum electrodynamics (QED) in $(2 + 1)$ dimensions based on a local U(1) gauge symmetry [Frad 13]. Polyakov showed that such a gauge theory (with static matter) is confining [Poly 77]. However, an RVB liquid with deconfined excitations can still exist at a special point (the so-called Rokhsar-Kivelson (RK) point) in the phase diagram as observed in the square lattice QDM. Lattice structure plays a vital role to determine the symmetries of the gauge theory which, in turn, affects the nature of the excitations in the liquid phase. The U(1) gauge theory on bipartite lattices essentially stems from their two-sublattice structure which is absent in non-bipartite lattices. Consequently, the U(1) symmetry in the former breaks down to $\mathbb{Z}_2$ in the latter [Moes 01c] owing to pair-condensation of spinons which acts as a Higgs field carrying gauge charge $2e$ [Sach 08]. The resultant gauge theory is deconfining which is the case for the QDM on a triangular lattice. The ground state of the model can support an extended gapped liquid phase in the phase diagram having the RK point at one of the corners [Moes 01a, Ralk 05, Misg 08]. A detailed discussion on the phase diagram of QDMs on different lattices will be presented in the next chapter. One noteworthy aspect of this liquid is that it possesses a nonlocal quantum order – known as *topological order* [Wen 90c, Wen 91]– which leaves distinct footprints on the low-energy physics of the model [Moes 01a]. Such an order results from long range quantum entanglement [Wen 90c] and is often characterized by discerning signatures in the entanglement entropy — a quantity to measure the degree of entanglement between two parts of a system [Li 08, Agua 08, Jian 12]. The gapped liquid phase in the QDM on the triangular lattice, for example, has a $\mathbb{Z}_2$ topologically ordered ground state as reflected in the fourfold degeneracy on a torus. Entanglement entropy for such a state obeys an *area law* behavior (scaling with the area of a subsystem instead of volume) with an additive correction [Levi 06, Kita 06, Eise 10], called the topological entanglement entropy that serves as a useful measure of the anyonic content in the theory.

QDM on a triangular lattice has intimate connections with spin models on the kagome lattice. Early work [Sach 92] on $S = 1/2$ Heisenberg antiferromagnetic model on a kagome lattice suggests a quantum-disordered ground state with no broken symmetry but deconfined excitations bearing resemblance with the liquid state of the triangular lattice QDM. The nature of the ground state for the isotropic Heisenberg model is still an open topic of debate and only recently, the existence of a $\mathbb{Z}_2$ topological liquid has been argued in numerical simulations [Yan 11, Depe 12]. The topological order remains even in the presence of certain anisotropic perturbations, *e.g.* a stable $\mathbb{Z}_2$ spin liquid is predicted in the phase diagram for an easy axis kagome antiferromagnetic model (EAKAM) with all possible spin exchanges in each of the hexagonal plaquettes of the lattice [Bale 02, Shen 05]. Such easy axis limit maps the spin model to a generalized QDM with three dimers emanating from each triangular lattice site. Increasing the dimer filling from 1/6 (QDM) to 1/2 (EAKAM) has interesting consequences such as larger extension of the topological liquid phase in the low-energy phase diagram compared to the standard QDM. However, the gauge theoretic descriptions for both the models are identical as the structure of the dual Hamiltonian rests only on the parity of the dimer number per site which is odd in both the cases. In the bosonic language these two models correspond to bosonic Mott insulators at 1/6 and 1/2 filling on the kagome lattice with the resultant dual model being a *fully frustrated transverse-field Ising model* on a honeycomb lattice [Moes 01a]. The intermediate filling of 1/3, on the other hand, is also quite interesting in this context and has not received much attention so far. It translates to a quantum fully packed loop (FPL) model on the triangular lattice which consists of nonintersecting close loops with local fluctuations of the loop segments being governed by the QDM Hamiltonian. The dual theory for the FPL model belongs to the even parity sector featuring the Hamiltonian of an unfrustrated *ferromagnetic transverse-field Ising model* that has non-trivial implications for the emergent low-energy phases. As we continue with this model, we will see the appearance of a novel lattice nematic phase which comprises parallel loops that break the rotational symmetry of the lattice.

The thesis is structured as follows. We begin with a brief review of models which realize Mott insulators on frustrated lattices in the strong correlation limit. The chapter contains basic aspects of fractional fillings particularly on a checkerboard and a kagome lattice. We then discuss the concept of topological order in context of the QDMs that can be thought as an alternative description for the low-energy insulating states of certain microscopic models of fractionally filled bosonic systems. In chapter 3, we introduce a recently developed numerical technique, called tensor renormalization group (TRG) [Levi 07, Gu 08], aimed at efficient simulations of short-ranged gapped models. Taking the example of the triangular lattice QDM we show how it applies to analyze the correlation functions in the gapped liquid phase which exists at the RK point [Royc 15b]. Pros and cons of this method for gapless systems are also discussed. In chapter 4 we explore the possibilities of realizing topological order in a generalized version of the QDM – namely the FPL model on a triangular lattice [Royc 15a] which emerges as an effective low-energy description for an extended Bose-Hubbard model on a kagome lattice at 1/3 filling with long range density-density interactions. Employing a combination of the exact diagonalization technique and tensor product state formalism we derive the ground state phase diagram of this model which features an unconventional quantum phase transition between a $\mathbb{Z}_2$ RVB liquid phase and a symmetry broken lattice nematic phase. An analytical understanding of the critical theory for such an unusual phase transition is presented in chapter 5 by establishing a connection to the Ising gauge theory followed by the projective symmetry group (a combination of lattice symmetries and gauge symmetries) analysis of the dual Hamiltonian. In chapter 6 we extend our discussion to a fermionic model on a partially filled kagome lattice which involves strong on-site and nearest neighbor Coulomb repulsions between electrons at filling fraction 1/3 [Poll 14]. The ground state for this model, although it does not have any topological order, is capable of hosting exotic magnetic and charge orderings as a result of the interplay between spin and charge degrees of freedom. We analyze the zero temperature phase diagram of this model in the strong correlation limit to demonstrate how charge fluctuations in the hexagonal plaquettes stabilize a plaquette phase with a novel antiferromagnetic order. Spin fluctuations in small loops, on the other hand, drive a first order transition to a short loop phase with local charge order. The last chapter gives a summary of all results and discusses some future research directions.

# Chapter 2

# From Frustration to Topological Order

Over the past few decades, frustrated models have received huge attention in the condensed matter community partly because they are potential hosts for novel states of matter [Diep 04]. The word *frustration* implies that interactions between the fundamental degrees of freedom cannot be simultaneously satisfied either because of the lattice geometry or due to their competing nature. In lattice spin models a frustrated plaquette corresponds to the condition that given a neighboring interaction between two spins $\vec{S}_i$ and $\vec{S}_j$ of strength $J_{ij}$ (ferromagnetic if $J_{ij} > 0$ and antiferromagnetic if $J_{ij} < 0$), the product $\prod_{\langle i,j \rangle} \mathrm{sign}(J_{ij})$ over the links of that plaquette is negative [Diep 04]. This situation often occurs in non-bipartite lattices [Wann 73] for which a clear distinction between two inter-penetrating sublattices is not possible. But in bipartite lattice models [Baxt 82], frustrations mainly appear due to different competing interactions between the constituent particles or spins [Vann 77]. Featuring an extensive ground state (GS) degeneracy [Vill 80, Kawa 84, Henl 89] frustrated systems potentially harbor a variety of exotic new phases at low temperatures for which examples are abundant in 2D and 3D. One such system in 3D is the Heisenberg antiferromagnet on pyrochlore lattice, which hosts collective excitations that form magnetic monopoles [Cast 08]. The system remains disordered at all temperatures and offers a prominent example of collective paramagnet [Vill 79] or the so-called *classical spin liquid* [Moes 98]. Quantum fluctuations in these frustrated antiferromagnets also have dramatic consequences, *viz.*, they favor a unique GS that evades any spontaneous symmetry breaking even at zero temperature [Ande 73, Shas 81]. In modern terminology, such a phase is popularized as *quantum spin liquid* [Wen 91, Rami 08, Bale 10] and characterized by fractionalized quasiparticle excitations [Ande 87a, Kive 87, Sent 01] similar to the fractional quantum Hall effect [Laug 83, Laug 88] or solitons in polyacetylene chain [Su 79]. On certain lattices this class of models has a non-trivial topological aspect associated with the many-body GS [Wen 90c] that is reflected in the quantum numbers of the quasiparticles [Wen 90a]. Along this avenue, some of the strongly correlated 2D models on frustrated lattices like kagome, checkerboard etc. have also been credited as promising candidates for having topologically ordered (to be explained later) paramagnetic ground states with fractional excitations [Moes 01c, Bale 02, Sent 04]. In the following, we briefly survey some of their discerning and notable features exemplifying the model of 2D Mott insulators on the checkerboard and the kagome lattice at different fractional fillings.

## 2.1 Fractionalization on frustrated lattices

Discovery of charge fractionalization in the context of condensed matter physics dates back to the early work of Su et al. [Su 79] on excitations in a polyacetylene chain which is composed of alternating single and double bonds between carbon atoms. An equivalent description of the model deals with noninteracting spinless fermions hopping on a 1D lattice with intra-cell hopping amplitude being different from the inter-cell one. As a result, two degenerate dimerization patterns can appear in the ground state. Removing an electron creates interfaces of these two states which can support solitonic domain wall excitations with fractional charge $e/2$. A field theoretic study for these excitations is found in Ref. [Jack 76]. In higher dimensions, charge fractionalization can be aided by strong interactions between the particles. In 2D, one such example is the fractional quantum Hall effect (FQHE) [Tsui 82, Laug 83] in which Coulomb repulsions between the electrons dominate at very low fillings restricting their motion within the lowest Landau level to form an incompressible liquid state. Robert Laughlin proposed the real space wave function for the GS evincing the emergent quasiparticles to be carrying a fractional charge of $e/m$ for a partial filling of the lowest Landau level given by the filling fraction $\nu = m^{-1}$, $m$ being odd integers [Laug 83]. Moreover, these quasiparticles obey a fractional statistics, *viz.*, the two-excitations wave function picks a phase factor of $(-1)^{\nu}$ upon interchanging their positions.

Even though, the FQHE requires application of high magnetic field at low temperatures, it turns out that this is not a necessary condition for charge fractionalization to occur. Even in absence of the external magnetic field, fractional charges can appear in certain models of interacting particles on frustrated lattices both in 2D and 3D [Fuld 02, Rung 04, Cast 12]. The situation typically arises in the strong-coupling limit of these models. The competition between different interactions in these frustrated systems often results in multiple low-energy states which are degenerate or nearly degenerate with each other. These states get mixed up due to quantum fluctuations which play a paramount role in controlling the low-energy physics of the models. In a system of interacting electrons, depending on the filling fractions, the GS can feature magnetic ordering [Poll 08] or other exotic charge patterns that breaks various symmetries [Poil 07, Trou 08] of the underlying lattice structure. While we discuss these aspects with particular attention to 2D, examples of 3D lattices [Fuld 02] should also be mentioned that can support stable fractional charges as low-lying excitations. A prominent candidate is the pyrochlore lattice in which the antiferromagnetic isotropic Heisenberg model [Cana 98, Cana 00, Moes 03, Herm 04] has been argued to host deconfined magnetic monopoles [Cast 12] as fractional quasiparticles. In what follows, we restrict ourselves to 2D only and highlight some specific frustrated lattice models which would instantiate the above phenomena in Mott insulators at certain fractional fillings in light of a generic Hubbard Hamiltonian for fermions and hard-core bosons.

**Spinless scenario.** We start with the extended Hubbard Hamiltonian [Rung 04] for spinless fermions that consists of a nearest-neighbor hopping term ($t$) and a nearest-neighbor repulsive interaction term ($V$) as

$$\mathcal{H} = -t\sum_{\langle i,j\rangle}(c_i^{\dagger}c_j + \text{H.c.}) + V\sum_{\langle i,j\rangle} n_i n_j \,, \tag{2.1}$$

where the operator $c_i^{\dagger}(c_i)$ creates(destroys) an electron at site $i$ of a lattice and the local density operator is given by $n_i = c_i^{\dagger}c_i$ with $\sum_i n_i = Nf$, $f$ being the filling fraction on the $N$-site lattice. We are particularly interested in the strong-coupling regime $|t| \ll V$ where the system is a Mott insulator, and notice that the lowest energy configurations obey some constraints imposed by the geometry of the lattice and the specific filling considered (that is how geometric frustration manifests in the model). On a checkerboard lattice (see Figure. 2.1), for example, at half filling the GS has exactly two particles in each of the crisscrossed squares [Ande 56], which is similar to what is known as the *ice rule* [Baxt 82]. The degeneracy essentially arises because of numerous ways to satisfy the constraint. The size of the GS manifold can be estimated by mapping the configurations to that of the *six-vertex model* [Baxt 82] which grows as $(4/3)^{3N/4}$ [Lieb 67]. This leads to a finite zero-point entropy per site (~0.216) characterizing the amount of frustration related to the specific lattice geometry. When an extra electron of charge $e$ is added to an allowed configuration of the system, it always violates the ice rule in two adjacent crisscrossed squares which now have three particles (Figure. 2.1) each and costs a net energy of $4V$. Once such a pair of defects are created, the violation cannot be undone by simply moving the electrons around the lattice (the defects are topological in this sense) but separating them is possible via single-particle hopping. The extra charge $e$, thus, elastically splits into two quasiparticles, each of them carrying a fractional charge of $e/2$. Their dispersion (caused by the hopping term) is related to the energy $E(\mathbf{k})$ of the added particle through $E(\mathbf{k}) = 4V + \epsilon(\mathbf{k}_1) + \epsilon(\mathbf{k}_2)$ along with the momentum conservation $\mathbf{k} = \mathbf{k}_1 + \mathbf{k}_2$. A variety of other frustrated lattices, such as kagome lattice, also shows this phenomena at $1/3$ or $2/3$ filling of the particles.

Quantum fluctuations can have drastic effects on this large GS manifold as they lift the extensive classical degeneracy by hybridizing different GS configurations. This is generally a perturbative process in terms of the single-particle hopping which generates coherent multi-particle ring exchange terms that predominantly control the low-energy physics in the strong-coupling limit. The effective Hamiltonian [Rung 04, Poll 06, Poll 07] which is relevant in the low-energy sector of the half filled case reduces to

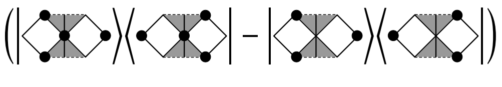

$$\mathcal{H}_{\text{eff}} = -\frac{12t^3}{V^2}\sum_{\{\hexagon\}}\Big(\big|\quad\big\rangle\big\langle\quad\big| - \big|\quad\big\rangle\big\langle\quad\big|\Big) + \text{H.c.} \tag{2.2}$$

where the sum is over all hexagons stretched in the vertical and horizontal directions on the checkerboard lattice as depicted in Figure. 2.1. Note the presence of a relative sign between the two kinds of resonating processes that differ in the occupancy of the central site. The sign results from the anticommutation relations of the fermions and is specific to the sequence in which they are ordered. The two-particle ring exchange around empty squares which is $O(\sim t^2/V)$ does not appear in (2.2) as the clockwise and anticlockwise

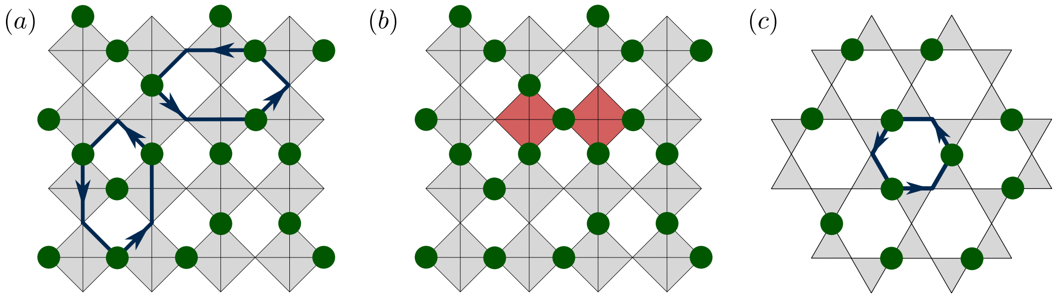

Figure 2.1: (a) A valid configuration satisfying the constraint of two electrons per crisscrossed square for the half filled case on the checkerboard lattice showing the lowest order ring exchanges around the stretched hexagons (both vertical and horizontal). (b) Charge defects (marked by red squares) created by adding an extra electron on the checkerboard lattice. The defects can move around by action of the single-particle hopping term. (c) Ring exchange processes on a $1/3$ filled kagome lattice.

processes interfere destructively for spinless fermions. However, if spin degrees of freedom are included, these processes have the largest contribution to the effective model, and hence, should be taken care of [Poil 07, Trou 08].

Inclusion of the ($\sim t^2/V$) processes in the low-energy theory is essential also for the models in which hard-core bosons are considered in lieu of spinless fermions. At quarter and half filling on the checkerboard lattice, these models can be exactly mapped respectively to the quantum dimer model (QDM) [Rokh 88] and the quantum fully packed loop (FPL) model [Batc 96] on a square lattice where the two-particle ring exchange term manifests as the flipping of parallel dimers or loop segments in an elementary square plaquette. We will exploit such a mapping later on while describing the low-energy theory for a particular class of bosonic Mott insulators. These insulators, under appropriate conditions, can anchor a non-trivial quantum order, dubbed *topological order* [Wen 90c, Wen 91], that results from long-range quantum entanglement in the system. This is true for QDMs on certain non-bipartite lattices which will be discussed in the next section with more details.

The effective model retains almost a similar form when the spinless fermions or hard-core bosons are considered on a kagome lattice (Figure. 2.1) except that the Hamiltonian now contains only one kind of ring exchange process involving three particles around a kagome hexagon. One can consider two commensurate partial fillings in this case – $1/3$ and $2/3$ which correspond to the configurations with one and two particles per kagome triangle respectively [OBri 10, Nish 10]. Both of them can be mapped to the QDM on a honeycomb lattice [Moes 01b] albeit with a subtle difference that a particle maps to a dimer for $1/3$ filling while a hole or empty site maps to a dimer for $2/3$ filling. We will resort to these dimer models on various lattices in the following section while illustrating the notion of topological order in a strongly correlated many-body GS.

**Including the spin.** Explicitly added the spin degrees of freedom to the problem, the effective model in the previously described half-filled case (two electrons per crisscrossed square) becomes a quarter filled model on the checkerboard lattice [Poil 07, Trou 08]. The ring exchange term remains the same since it *commutes* with the total spin. In addition, one needs to take into account the Heisenberg spin exchanges allowing for simultaneous charge and spin fluctuations in the theory. New kinds of charge and magnetic order can set in as a result with possibilities of phase transitions between various ordered phases in the phase diagram. Having the spin degrees of freedom adds an on-site repulsion $Un_{i\uparrow}n_{i\downarrow}$ to the Hamiltonian in (2.1) which typically sets the largest energy scale of the problem. The two-particle ring exchange term around empty squares is instrumental only when the participating electrons are of opposite spins. Hence, the effective Hamiltonian, to the leading order, takes the form

$$\mathcal{H}_\square = -g \sum_{\{\square\}} (c^\dagger_{i\uparrow} c^\dagger_{j\downarrow} - c^\dagger_{i\downarrow} c^\dagger_{j\uparrow})(c_{k\uparrow} c_{l\downarrow} - c_{k\downarrow} c_{l\uparrow}) + \text{H.c.}\,, \tag{2.3}$$

where $g = 2t^2/V$ and the sum runs over the empty squares of the lattice with the four sites of a given square enumerated cyclically as $ikjl$. One can add a diagonal term

$$\mathcal{H}_\text{W} = W \sum_{\{\square\}} \Big(\frac{1}{2} - 2\mathbf{S}_i \cdot \mathbf{S}_j\Big) n_i n_j (1 - n_l)(1 - n_k) \tag{2.4}$$

that counts the number of empty squares which $\mathcal{H}_\square$ can act upon. Note that the spin dependent prefactor in $\mathcal{H}_\text{W}$ essentially projects out the states where an empty square is diagonally filled up by two spins of same species. Another relevant term, which induces spin fluctuations, is the antiferromagnetic Heisenberg spin exchange given by

$$\mathcal{H}_\text{spin} = J \sum_{\langle i,j \rangle} \Big(\frac{1}{4} - \mathbf{S}_i \cdot \mathbf{S}_j\Big) n_i n_j \tag{2.5}$$

with $J/g \simeq 2V/U + 4t/V$ in the perturbative limit $U \gg V \gg t$. For $J = 0$, the Hamiltonian looks similar to the QDM on a square lattice which is obtained by joining the centers of the crisscrossed squares, the particles on the checkerboard lattice being interpreted as dimers on the square lattice. We shall discuss the physics of the QDMs with more details in the following section drawing concrete connections to other lattices also.

Let us now focus on the phase diagram (Figure. 2.2) of this fermionic model parametrized by $J/g$ and $W/g$. For $J = 0$ and $W/g = 1$, there exists an exactly solvable point in the model (akin to what is known as the Rokhsar-Kivelson point in context of the QDM) where the GS is an equal weight superposition of all zero-energy configurations and describes a liquid state with algebraically decaying correlations. Away from this special point on the side of $W/g < 1$, there lies an intermediate regime where the GS is twofold degenerate featuring a novel resonating singlet pair crystal (RSPC) phase that breaks the translation symmetry (Figure. 2.2) of the lattice. For sufficiently negative $W/g$, parallel chains of electrons appear along the diagonals of the void squares breaking instead the rotational symmetry of the lattice. The RSPC phase is stable even in presence of the Heisenberg term in (2.5) up to $J/g \sim 1.5$ beyond which a new four-electron plaquette order emerges. Removing an electron in this case leaves two adjacent crisscrossed squares defected which now have one electron, hence, carrying a fractional charge of $e/2$ each. The single-particle hopping term can separate the defects but a weak pairing between them still exists even when $|t|/g > 1$. For a finite doping, these effects may lead to a new supersolid phase (with

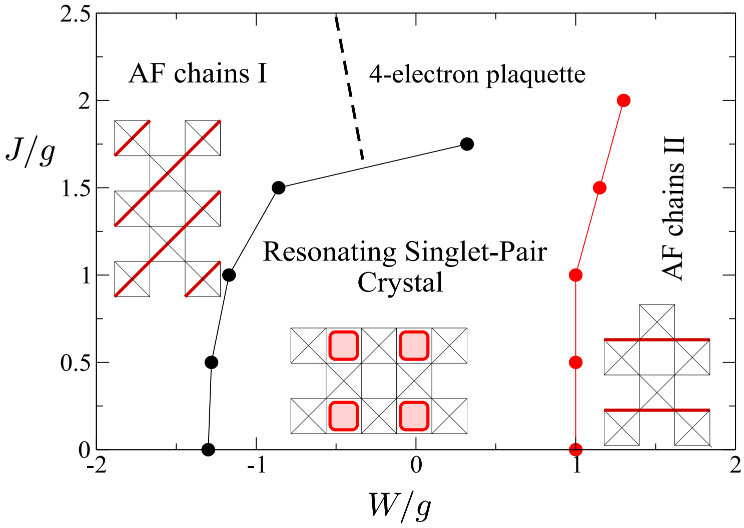

Figure 2.2: The phase diagram for the electronic model on the checkerboard lattice at quarter filling taken from Ref. [Poil 07].

no charge modulation) which inherits the broken translation symmetry from the insulating parent RSPC state.

Similarly on a kagome lattice also, a large variety of different symmetry broken phases (both charge ordered and spin ordered) appear in the phase diagram for the extended Hubbard model in (2.1) including $Un_{i\uparrow}n_{i\downarrow}$ at different commensurate partial fillings (particularly at filling fraction $1/6$ and $1/3$). In the extreme limit of $U \to \infty$ and also $V \gg t$, the GS configuration of the model has one and two electrons per triangle respectively at filling $1/6$ and $1/3$. Here we briefly describe a notable phenomenon of *kinetic ferromagnetism* on a kagome lattice [Poll 08] for the $1/6$ filling and particularly the development of a new antiferromagnetic (AFM) order for the $1/3$ filling (a more detailed discussion is deferred till chapter 6). Quantum fluctuations in these cases lead to the similar effective Hamiltonian as (2.2) that preserves the SU(2) symmetry of spin. The GS of the system is found to exhibit ferromagnetism which supposedly coexists with the symmetry broken plaquette ordered phase even in the thermodynamic limit. However, the robustness of the ferromagnetic (FM) GS can be tested by introducing the next-nearest-neighbor AFM spin exchange ($J_2$). Below a critical value $(J_2/g')_c \approx 0.2$, the FM state pursues but above this, the AFM spin fluctuations dominate to favor the state with minimum $|S^z_{\text{tot}}|$. Doubling the filling to $1/3$, the effective model in the strong-coupling limit turns out containing the nearest-neighbor AFM spin exchange in addition to the plaquette term (ring exchange of three electrons) [Poll 14]. The insulating GS at this filling can harbor different kinds of ordered phases as a result of the interplay between charge and spin fluctuations. Particularly the plaquette ordered phase develops a new AFM order whose detailed account will be presented in chapter 6. It should be noted following the work by Ferhat and Ralko [Ferh 14] that an average electronic filling of one-third on the kagome lattice can also lead to the formation of a semi-metallic state, spin-charge density modulations and many other exotic phases if the constraint of $U > V$ is relaxed. However, in chapter 6 we will focus on the limit of $U < V$ which is more realistic and can be traced efficiently in terms of an effective Hamiltonian description.

## 2.2 Topological order at fractional fillings

Topological order represents an unusual ordering pattern in the GS which cannot be captured by a local order parameter [Wen 90c]. It is to be contrasted with the conventional order that arises either due to phenomena like spontaneous symmetry breaking or symmetry mismatch in different phases. Thus, characterizing topological order falls beyond the usual Landau paradigm [Land 80, Ma 00]. This kind of exotic order generally emerges with features like GS degeneracy on a topologically non-trivial manifold and/or appearance of zero energy edge states along open boundaries [Wen 89]. The FQHE discussed in the previous section is one such example which harbors topological order on the GS [Wen 90a] which manifests through an $m$-fold GS degeneracy on a torus at filling fraction $\nu = 1/m$. The edge excitations in such a system can be modeled by the theory of a chiral Luttinger liquid [Wen 90b]. Among other 2D lattice models of interacting particles at partial fillings, QDMs and quantum spin liquids provide a fertile ground to look for a topologically ordered GS with fractionalized quasiparticle excitations. As we will see later, in the strong-coupling limit, the low-energy physics for certain classes of bosonic models, which include long-range interactions, are effectively described by these dimer models when specific filling fractions of bosons are considered.

**Quantum dimer models.** The QDM Hamiltonian on a minimal setting dictates the quantum dynamics of the dimers with a kinetic term ($t$) that flips two parallel dimers around the smallest plaquette and a potential term ($V$) that counts the number of such flippable plaquettes. While the dimers gain energy by the kinetic term which favors as many flippable plaquettes as possible, the potential term penalizes them [Rokh 88]. The competition yields various dimer ordered phases that appear in the GS phase diagram of the model at different values of $V/t$ and break different lattice symmetries with interesting implications. However, there exists a special point on the phase diagram [Leun 96] at $V/t = 1$ and known as the Rokhsar-Kivelson (RK) point (Figure. 2.3), where the model is exactly solvable and the system becomes critical. The zero energy GS has a topological degeneracy on a torus and grows linearly with the number of lattice sites which can be understood by mapping to a height model [Henl 97, Henl 04]. In each of the topological sectors, the GS is an equal weight superposition of all the dimer configurations. The state represents a U(1) liquid phase with gapless excitations known as "resonons". This degeneracy is not topologically robust (even though the state has some non-trivial quantum order which is not locally detectable) since the liquid phase is gapless having algebraically decaying dimer-dimer correlations ($C_{dd} \sim r^{-2}$). The two extremes of very large positive $V/t$ and large negative $V/t$ represent respectively the staggered phase (with isolated staggered dimer configurations) and the columnar phase [Sach 89] as reminiscent of the diagonally oriented parallel chains of electrons on the checkerboard lattice [Poil 07]. In the thermodynamic limit, the columnar state is fourfold degenerate and breaks the translation and rotational symmetry [Leun 96]. Between these two, there appears an extended region of plaquette ordered state

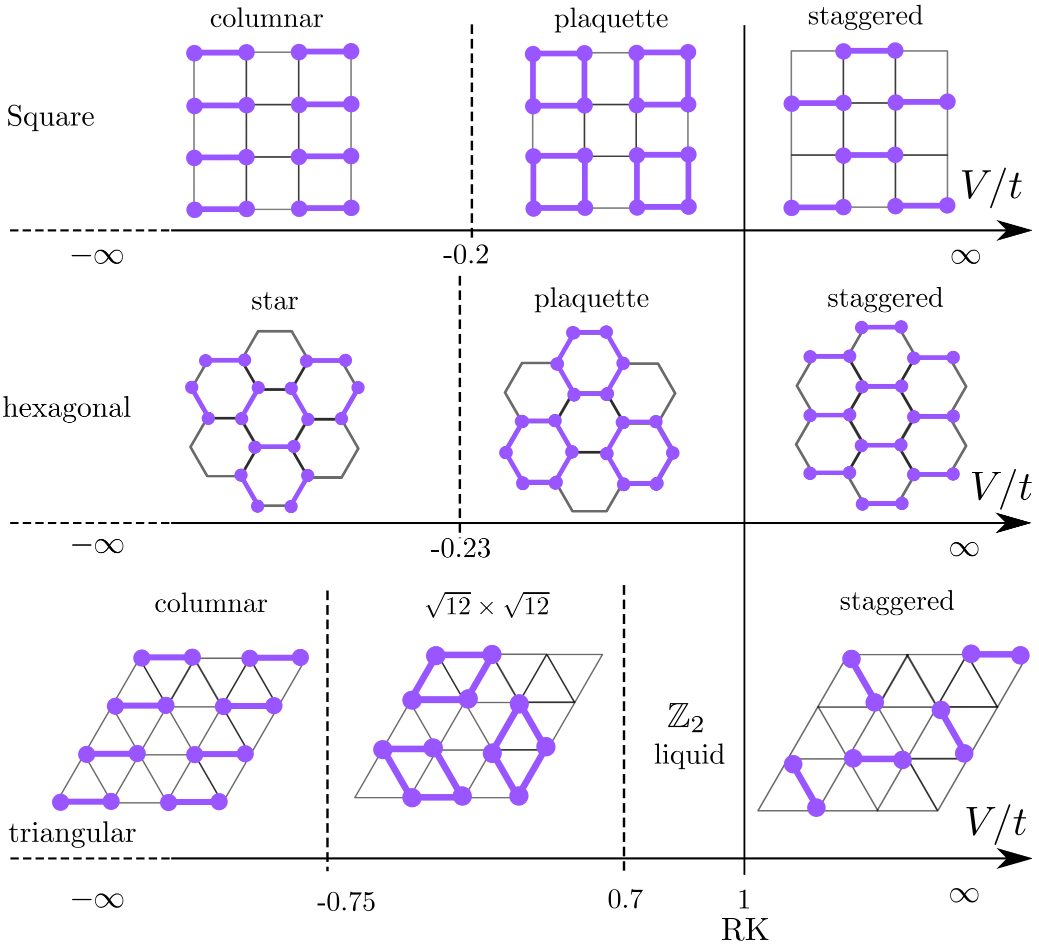

Figure 2.3: The QDM phase diagram on different lattices. Individual description for each of them is outlined in the text. Necessary details can be found in Ref. [Leun 96, Moes 01b, Moes 01a, Ralk 05].

(like the RSPC) [Leun 96, Sylj 06] separated from the staggered phase by the RK point (see Figure. 2.3). However, the exact point of transition between the columnar and the plaquette phase is still an issue of debate. While Ref. [Leun 96] indicates the transition to occur at $V/t \sim -0.2$, Ref. [Sylj 06] emphasizes on a positive value of $V/t \sim 0.6$ based on a quantum Monte Carlo study. Another recent work entirely rules out any possibilities to realize the plaquette phase in the square lattice QDM [Bane 14]. According to Ref. [Bane 14], the columnar phase persists in the entire region of $-\infty < V/t < 1$ while the staggered phase takes over right after the RK point is crossed.

However, this transition is quite prominent for the QDM on a honeycomb lattice (Figure. 2.3) [Moes 01b]. The dimer kinetic term in this case involves three dimers sitting alternatively on a hexagonal plaquette of the honeycomb lattice and shifts them by one. Besides the liquid phase at the RK point, the GS supports three crystalline phases at different values of $V/t$. At large negative $V/t$, there exists the threefold degenerate star phase (with a finite excitation gap) with maximum number of flippable plaquettes which, by tuning $V/t$ towards 1, transforms to the plaquette phase through a discontinuous transition at $V/t \sim -0.23$. The plaquette phase is also a threefold degenerate, gapped like the star phase and extends till the RK point after which the system enters the staggered phase through a supposedly continuous transition.

To this end, it is worth contrasting the discussion against the phase diagram for the QDM on a non-bipartite lattice (Figure. 2.3) which exhibits more exotic plaquette orders and offers a perfect example of topologically ordered RVB liquid in 2D. The lattice of specific interest in this context would be the triangular lattice for which the liquid state is gapped (with exponentially decaying dimer correlations) and exists over an extended region of $0.7 < V/t \leq 1$ [Moes 01a, Ralk 05]. At the RK point, there exists a fourfold degeneracy of the zero energy GS which carries the signature of a $\mathbb{Z}_2$ topological order [Moes 01c], taken the model on a torus. The four degenerate ground states can be obtained from each other by threading $\mathbb{Z}_2$ fluxes through different holes of the torus. Besides having the usual spinon and holon excitations that are discussed in the previous chapter, the $\mathbb{Z}_2$ liquid phase supports a new kind of excitations which are Ising vortex like [Read 89] and dubbed *vison* [Sent 01]. The GS is a zero vison state protected by a finite vison gap. The visons, which reside on the dual lattice, are essentially the excitations in the low-energy gauge fields which have a $\mathbb{Z}_2$ symmetry (hence described by an Ising gauge theory (IGT) [Moes 01c] as opposed to the U(1) gauge theory for the bipartite case [Frad 90, Frad 13]). This is intimately connected to the non-bipartite structure of the underlying lattice. Another manifestation of the $\mathbb{Z}_2$ topological order is the non-trivial anyonic statistics associated with the fractionalized quasiparticle excitations (visons and spinons) [Wen 90c, Wen 04]. To a spinon, the vison appears as the source of $\pi$ flux, hence, surrounding it, a spinon wave function picks up a phase factor of $(-1)$. This implies that these two quasiparticles are endowed with mutually semionic statistics (although bosonic self-statistics) which is one of the salient features of $\mathbb{Z}_2$ topological order and the underlying gauge theory. These two quasiparticles are commonly known as $e$ (spinon) and $m$ (vison) particle of the IGT [Kita 03]. It is possible to further classify the theory into an *even* and *odd* sector depending on the number of dimers emanating form a given lattice site [Moes 01c]. We will comment on this point in details later in chapter 5 while formulating the IGT in context of a quantum FPL model on the triangular lattice [Royc 15a]. It should also be noted that, besides hosting a $\mathbb{Z}_2$ liquid phase, the phase diagram for the triangular lattice QDM (Figure. 2.3) features various other symmetry broken crystalline phases such as the $\sqrt{12} \times \sqrt{12}$ plaquette ordered phase, the columnar phase at large negative $V/t$ and the trivial staggered phase for $V/t > 1$. Among other examples of topologically ordered GSs, the spin-$1/2$ kagome Heisenberg model is worth a note and only recently known to harbor a $\mathbb{Z}_2$ topologically ordered spin liquid at low temperatures [Yan 11, Depe 12, Han 12].

# Chapter 3

# Tensor Renormalization Group Approach to Dimer Models

As pointed out in the preceding chapter, the QDM Hamiltonian has a simple classical description at the RK point that it maps to a model of classical dimers at infinite temperature. These classical models have been of great interest in statistical physics long before the quantum version was introduced because of their resemblance to the solvable vertex models [Baxt 82]. In one of the seminal papers, Fisher first pointed out that the frustrated Ising model on planar lattices can be mapped to the classical dimer model on the dual lattices corresponding to the same degenerate ground state manifold [Fish 61]. The zero-temperature frustrated Ising-spin model on the triangular lattice, for example, can be translated to the dimer model on the dual honeycomb lattice where the dimers essentially represent the frustrated honeycomb links. An important step towards solving this kind of model and calculating the correlations of relevant observables in a classical setting was the introduction of the Pfaffian techniques [Kast 61, Fish 61], which turned out to be very useful for the simplest dimer problem on square lattice where a critical phase can be realized with algebraic dimer correlations [Alet 05]. The problem was further complicated by incorporating the classical dimer-dimer interactions in the model which could energetically favor parallel dimer ordering in the smallest square plaquettes [Alet 06]. The important finding of the study was to observe a temperature driven phase transition of Kosterlitz-Thouless type which separates the high-temperature liquid phase (with algebraic correlations) from a low-temperature dimer-crystalline phase with parallel dimer ordering.

Both the classical (interacting and non-interacting) and the quantum model of dimers have been extensively studied using various numerical techniques such as classical Monte Carlo (MC) [Alet 06, Fend 02], quantum Monte Carlo [Moes 01a, Ralk 05] and several others. Besides these traditional methods, a whole new series of simulation algorithms proliferated in last few years aiming at the efficient representation of many-particle quantum states based on the ideas motivated mostly from subjects of quantum chemistry and quantum information theory [Vers 02]. The family contains members such as projected entangled-pair states (PEPS) [F Ve 04], tree tensor state [Shi 06], and multiscale renormalization ansatz [Vida 07, Vida 08], all based on representing the fundamental degrees of freedom by tensors defined on the lattice. For one-dimensional quantum systems in the thermodynamic limit, the ground state wave function extracted from the density matrix renormalization group (DMRG) can be exactly expressed as matrix-product states (MPS)[Romm 97]. In the process of generalizing the concept of MPS one step further, the tensor product representation was introduced and successfully applied to some of the classical lattice models for computing the partition function along with other physical quantities in presence of local interactions [Levi 07, Zhao 10]. In Ref. [Levi 07], the authors proposed a real space renormalization of the tensors, coined as tensor renormalization group (TRG), much in the spirit of block spin scheme used in the coarse-graining of usual renormalization group (RG) approach [Ma 00] and estimated some of the critical exponents of the square lattice Ising model with good accuracy.

We adopt this scheme to study the correlations in the infinite temperature classical dimer model and compare the results with conventional Monte Carlo (MC) techniques. The specific observable of interest is the dimer-dimer correlation functions on the square lattice and the triangular lattice, even though the method can be generalized to other lattices also. The chapter starts with introducing the concept of tensor network renormalization taking the triangular lattice dimer model as an example. In the following, we will illustrate how to calculate the correlation functions in this model using such an approach. We then briefly review a recent analytical tool, called the Pfaffian method, which can be used for an exact calculation of the partition function of the model. Results of TRG method are compared with the correlation functions extracted from this analytical treatment. We will also benchmark the method (TRG) against the standard simulation techniques such as the worm algorithm used in classical Monte Carlo.

## 3.1 Tensor network renormalization

A Tensor network is a set of tensors arranged in a particular pattern aimed at efficiently representing a state of a system [Orus 14] which can also be extended to describe various classical lattice models [Levi 07]. The rank of each tensor, defined on a lattice site, is essentially the coordination number of the underlying lattice while the range of each index (i.e. the cut-off) is highly problem specific. The tensor network renormalization technique is based on real space regrouping of these tensors much in the same spirit as the standard RG scheme [Ma 00]. Assigning integer numbers to the indices of the tensors following a certain set of rules, in practice, specifies the classical configuration of interest with a given weight and contributes to the partition sum ($Z$) of the problem by that fraction. For an N-color dimer model these integers range up to $N$. In this chapter we consider the classical dimer models of a single color for which a lattice link can either be empty or occupied by one dimer only. The tensor indices can accordingly take values either 0 (empty) or 1 (occupied). Later in chapter 6, we will discuss a two-color fully packed loop model on a honeycomb lattice for which if one constructs a tensor network, the indices would take values from 0 to 2. The correlation functions in these models can be extracted numerically by relating to $Z$ which is computed by successive tensor contractions that resemble the idea of the standard block spin renormalization technique. Below we describe the procedure specific to the model of our interest which involves classical dimers on a triangular lattice.

### 3.1.1 Tensor networks

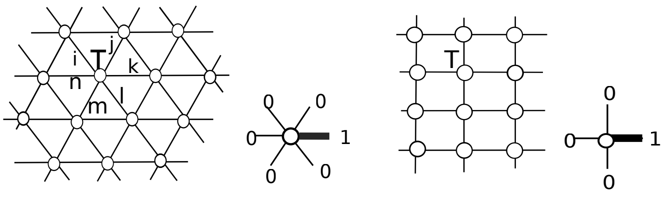

(a) (b) (c) (d)

Figure 3.1: (a) and (c) Tensor network representation for 2D lattices. Example of a dimer state (around a site) represented by tensor network on triangular lattice (b) and square lattice (d).

Configurations of the edges around each site in a valid dimer configuration can be formally described in tensor network representation $T_{ijkl...}$ with virtual indices $i, j, k, l, ... = \{0, 1\}$ on the triangular and square lattice as shown in Figure. 3.1(a-b) and (c-d) respectively. The statistical weight for a given configuration can be measured as

$$W(i, j, k \cdots) = T_{ijklmn} T_{iopgrs} \cdots , \tag{3.1}$$

where the virtual bond includes “0" and “1". The virtual index “0"(“1") indicates absence(presence) of a dimer along the edge. For a local tensor, for example, $T_{ijklmn}$ on the triangular lattice, the hard-core constraint

$$T_{ijklmn} = \begin{cases} 1 & \text{if } (i + j + k + l + m + n) = 1; \\ 0 & \text{otherwise,} \end{cases} \tag{3.2}$$

can be used to ensure each vertex to be connected to one dimer only. The partition function is the sum of the weights of all possible configurations:

$$Z = \sum_{i,j,k,l\cdots} W(i, j, k, l \cdots) = \mathrm{tTr}(T_{ijklmn} T_{iopgrs} \cdots), \tag{3.3}$$

where “tTr" means the tensor trace that all indices on connected links in the tensor network are summed over.

### 3.1.2 Renormalization algorithm

In two-dimensional systems, it is, however, difficult to calculate the tensor trace (tTr) since all indices on the connected links in the network need to be summed over. This imposes the hurdles of an exponentially hard calculation. Several approximation schemes have been proposed as solutions in this context such as iPEPS algorithm, the corner transfer matrix method (CTMRG) [Orus 09], and tensor renormalization approach [Levi 07, Gu 08] which tackle this problem essentially by scaling the computational effort down to the polynomial level of calculating the tensor trace. We use the latter approach which is akin to the real space renormalization in the way that at each step, the RG is structured by merging sites

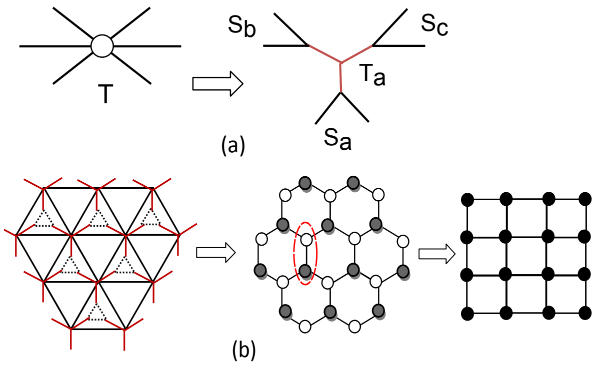

Figure 3.2: (a): Decomposing the tensor $T$ into $S_a$, $S_b$, $S_c$, and $T_a$. (b): Combining the three tensors in a dashed triangle $S_a$,$S_b$, and $S_c$ to form a new tensor $T_b$. The triangular lattice, thus, deforms into a honeycomb lattice with $T_a$ (white) and $T_b$ (black) tensors on the respective sublattices. Further grouping of the two tensors in every basis of the honeycomb lattice generates a new square lattice network of rank-4 tensors.

(by contracting respective tensors) and truncating the bond dimensions according to the relevance of the eigenvalues in the Schmidt decomposition of the old tensors. We resort to this technique for calculating the partition sum and describe the steps, for example, on a triangular lattice starting with the original local tensor $T$. In the process, we first split it into four parts, $S_a$, $S_b$, $S_c$ and $T_a$ with several singular value decompositions as shown in Fig 3.2(a), which, in turn, changes the lattice structure after the first step. The second step is to build a new rank-three tensor denoted by $T_b$ [see Figure. 3.2(b)] as follows:

$$T_{b(\alpha\beta\gamma)} = \sum_{ijk} S_{a(ij\alpha)} \times S_{b(jk\beta)} \times S_{c(ki\gamma)}. \tag{3.4}$$

The third step is to merge two sites to form a new rank-4 tensor shown in Figure. 3.2(b). The triangular lattice tensor network is now mapped to a square model where applying TRG is known to be simple and straightforward [Jian 08]. Each step of TRG reduces the number of sites by half. Eventually, the entire network collapses to only a few sites and the double tensor trace appearing in the partition function $Z$ can be calculated easily.

In the following, we briefly discuss how to calculate the dimer dimer correlation functions in this tensor network. We assume the distance between two dimers to be $r = |R_i - R_j|$ and use the dimer counting operator $d(R_i)$ for a given link $R_i$. The correlation functions $\langle d(R_i)d(R_j)\rangle$ can be represented as a tensor trace with four impurity tensors living on the sites $i, i+1$ and $j, j+1$ as shown in Figure. 3.3(a) and uniform tensors $T$ on every other sites. After the first step of TRG, we decompose these tensors and form the new rank-3 tensors as prescribed before which leads to a new network on a honeycomb lattice where the number of the impurity tensors [red dots in Figure. 3.3(b)] increases to 14. By blocking every two tensors in one, we arrive at a square lattice network comprising of the new rank-4 tensors with the impurity tensors being 10 in number. In the process of further coarse-graining, the lattice structure remains intact with the same number of impurity tensors as shown in Figure. 3.3(c)-(e), however the distance renormalizes by a factor of $1/\sqrt{2}$ in every step. Finally, we end up with a tensor network of the size we expect, and obtain the correlation

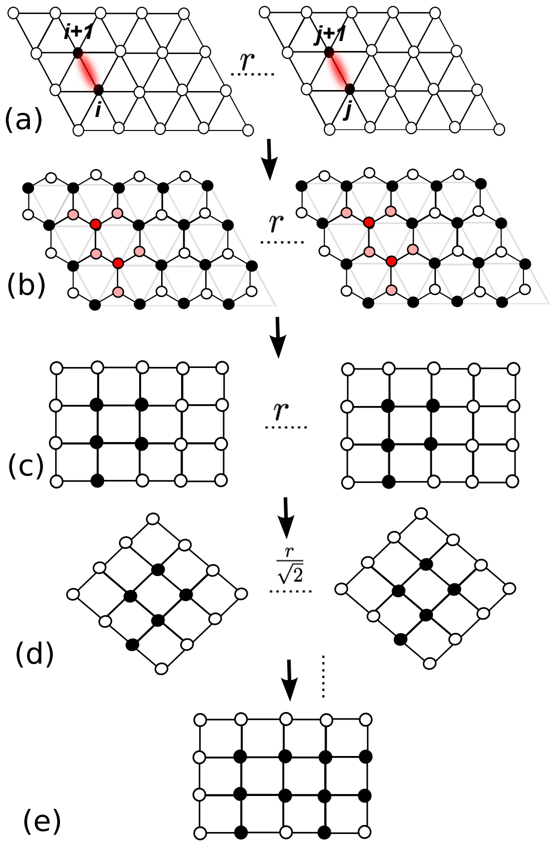

Figure 3.3: Schematic of the tensor renormalization for calculating dimer-dimer correlation function at a distance $r$. (a)(c)(d)(e):The black dots represent the impurity tensors and white dots represent the uniform tensors. (b): The red dots represent the impurity tensors while white (black) dots represent the uniform tensors on respective sublattices.

functions by performing the tensor trace. Before proceeding further to show the results of TRG, it is worth recalling some of the known results that are obtained from analytical treatments (the Pfaffian method) of classical dimer models on square and triangular lattice. We will consider a common geometry which can be interpolated between these two lattices by tuning a single parameter through which one can exactly compute the partition function of the problem.

## 3.2 Results from the Pfaffian method

Before outlining the main results let us briefly discuss the structure of the method [Fend 02] details of which is provided in Appendix A. The partition function involves construction of an antisymmetric matrix $M$ whose entries are decided by Kasteleyn's clockwise-odd rule (see Appendix A). The partition function is given in terms of the Pfaffian of this matrix which can be evaluated using Grassmann field representation. In other words, given a

| $r$ | $D(r)_{t=0}$ | $D(r)_{t=1}$ |
|---|---|---|
| 1 | 0.12505080 | 0.0466891518 |
| 2 | 0.05780328 | 0.0268276742 |
| 3 | 0.07535259 | 0.0281878353 |
| 4 | 0.06192191 | 0.0277736735 |
| 5 | 0.06695547 | 0.0277821043 |
| 6 | 0.06235789 | 0.0277783224 |
| 7 | 0.06465416 | 0.0277778197 |
| 8 | 0.06242982 | 0.0277777879 |
| 9 | 0.06375758 | 0.0277777821 |

Table I: The dimer-dimer correlation function for square lattice ($t = 0$) and for triangular lattice ($t = 1$).

Grassmann field $\psi_i$ defined on the lattice site $i$, the partition function ($Z$) is related to the quadratic Grassmann action ($S$) as

$$Z = \int [D\psi] \exp(S) \tag{3.5}$$

where $S = \sum_{i<j} M_{ij}\psi_i\psi_j$. The entries $M_{ij}$ depend on the bond fugacities $u$, $v$, and $t$ which are assigned to each of the vertical, horizontal, and diagonal bonds respectively. Note that such assignment additionally implies a two-site unit cell for which the Grassmann variables carry an extra index $\alpha = 1, 2$. In this context, a triangular lattice corresponds to the isotropic case of $u = v = t = 1$ whereas for the square lattice we set $u = v = 1$ and $t = 0$. All correlation functions, which explicitly depend on these parameters, can be calculated relating to the two-point Green function of the Grassmann variables,

$$G_{ij}^{\alpha\beta} \equiv \langle \psi_{\alpha,\vec{R}_i}\psi_{\beta,\vec{R}_j} \rangle = \frac{1}{Z}\int [D\psi]\psi_{\alpha,\vec{R}_i}\psi_{\beta,\vec{R}_j} \exp(S) \tag{3.6}$$

which implies the correlation between two Grassmann variables located at the $\alpha^{\text{th}}$ site of a unit cell at $\vec{R}_i$ and $\beta^{\text{th}}$ site of another unit cell at $\vec{R}_j$. The dimer-dimer correlation function can be then conveniently expressed as

$$D(r) = \langle \psi_{1,R_i}\psi_{2,R_i}\psi_{1,R_j}\psi_{2,R_j} \rangle, \tag{3.7}$$

where we consider the case of two parallel dimers for which $R_j = R_i + r\hat{x}$. One can apply Wick contraction to the above correlator to decompose into products of Green functions given in (3.6). Finally the quantity $\langle \psi_{\alpha,\vec{R}_i}\psi_{\beta,\vec{R}_j} \rangle$ is calculated by transforming it to a momentum space integral (see Appendix A) and reverse transforming to real space which leads to Table I. Since we are interested in studying the dimer models numerically, we adopt another simulation scheme, the classical MC, for comparing the results with TRG on clusters of different sizes of triangular and square lattice. The standard MC algorithms have been very useful in simulating many of the classical problems by stochastically sampling the configurations based on Markov chain process [Newm]. We first present a brief account

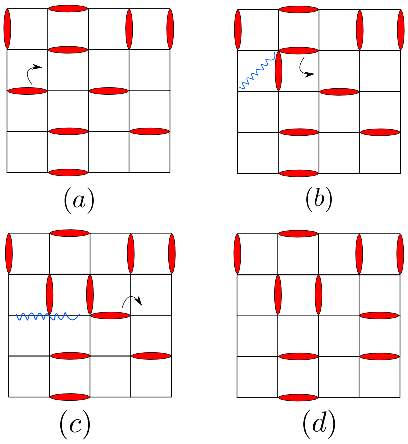

Figure 3.4: (a) Dimer covering on square lattice. The arrow denotes the first move taken in Monte Carlo. (b) Two defects, joined by the string, are created at the sites having no dimer and two dimers. (c) The defects move farther apart. (d) The final configuration achieved as consequence of the successive moves becomes a valid dimer configuration when the two defects merge at a lattice site. The arrows indicate successive dimer moves.

on implementing the MC algorithm for dimer models, then the same for the TRG construction. The details of the lattices are not very important for MC at the level of building the moves obeying two necessary conditions: detailed balance and ergodicity. The algorithm is knows as "long-loop worm algorithm" which satisfies both the conditions even for large system sizes [Newm].

## 3.3 Classical MC algorithm for dimer models

On a square lattice of extent $L$, the total number of dimers is $L^2/2$ which corresponds to a filling fraction of $1/4$ (because the number of links is $2L^2$). We choose an arbitrary dimer configuration satisfying the hard-core constraint (no two dimers can meet at a site) to start the Markov process. In the first move, a dimer is randomly chosen and flipped to one of its six empty neighboring bonds as shown in Figure. 3.4(a). This generates two defects (we call them head and tail of the worm for demonstration) one at a site with no dimer attached (tail) and the other at the site with two touching dimers (head) as depicted in Figure. 3.4(b). In the next step as in Figure. 3.4(c) we move that very dimer attached to the head which was present prior to the new dimer flipping in such that the defected head (with two dimers) always hops to a new site (we disdain the moves where it stays back even if the dimer flips to one of the empty bonds emanating from the head itself. This happens, for example, if in Figure. 3.4(b) the dimer on the horizontal bond attached to the head and denoted by the arrow, flips by an anticlockwise rotation of 90°). This way we continue with the successive moves until the defects meet each other and coincide in the very last move. This happens when one dimer always comes to fill one of the links attached to the fully emptied site generating a new valid configuration as in Figure. 3.4(d). The detailed balance is clearly satisfied as we always arrive at a new configuration (say, $\mu$)

from an old one (say, $\nu$) with a finite probability $\mathcal{P}_{\nu \to \mu}$ where $\mathcal{P}_{\nu \to \mu} \propto \frac{1}{N} \cdot \frac{1}{6} \cdot (\frac{1}{3})^{l-1}$ in a system of $N$ dimers, hence all the configurations can be reached in finite time. Note that $l$ is the total number of moves to connect two configurations $\mu$ and $\nu$. In order to calculate the dimer-dimer correlations efficiently, we construct a correlation matrix and average over all possible dimer locations along both the directions in a given configuration keeping the distance fixed. The correlation function is finally averaged over $\sim 10^{10}$ configurations in lattices up to $L = 128$.

Similarly, on a triangular lattice of size $L \times L$, the average dimer density corresponds to the filling fraction 1/6. The entire procedure carries over $mutatis - mutandis$ except, $\mathcal{P}_{\nu \to \mu} \propto \frac{1}{N} \cdot \frac{1}{4} \cdot (\frac{1}{2})^{l-1}$ and the correlation is calculated along the horizontal direction with parallel dimer ordering only.

## 3.4 TRG results

The relevant quantity of our interest is the dimer-dimer correlation which appears very useful in characterizing different phases of the classical dimer models on bipartite and non-bipartite lattices. The connected correlation function is expressed as,

$$C(r) = \langle d(R_i) d(R_j) \rangle - \langle d(R_i) \rangle \langle d(R_j), \rangle. \tag{3.8}$$

where $r = |R_i - R_j|$ and $d(R_i)$ counts 1 if a dimer is present on the link $R_i$ in a given configuration otherwise 0. Here the notation $\langle \cdots \rangle$ denotes the statistical average over all the configurations. In the asymptotic limit of large $r$, the correlation converges to the square of the average dimer concentration $\langle d(R_i) \rangle$ which is 1/16 and 1/36 on the square and triangular lattice respectively.

In the MC simulation the above function is calculated for different clusters of size up to 128×128 for both the lattices. The distance $|R_i - R_j|$ is chosen along a particular direction (one of the lattice vectors of the square/triangular lattice) and the final correlation function is averaged over all possible directions and dimer orientations. The results shown in Figure. 3.5(a) are in well agreement with the Green function (GF) calculations and indicative for a finite correlation length ~ one lattice spacing in case of the triangular lattice dimer model. The error bars are very tiny since the averaging is performed over a large number of statistical ensembles. On the other hand, the dimer-dimer correlation on the square lattice is visibly algebraic of the known form of $|C(r)| \sim r^{-2}$ for large $r$ as displayed in the lower panel of Figure. 3.5(b).

Compared to the MC results, TRG also shows similar functional form of the correlator for the dimer model on the triangular lattice. The TRG results in Figure. 3.5(a) are consistent even at large system sizes (up to 128×128) and achievable at the cost of a reasonable cut-off $\chi_c$. Although we pick up the horizontal direction as a reference along which $r$ is measured in this case (see Figure. 3.3) while coarse-graining the tensor networks, it turns out that the correlation function depends neither on it nor on the orientations of the dimers. It is only a function of the magnitude of $r$. In our case, the required convergence is obtained for $\chi_c = 20$ which certifies TRG as an extremely useful machinery for studying short-ranged gapped systems. However, for the square lattice dimer model, TRG turns out to be not so effective on account of large deviations from the exact results and MC while keeping the parameters (system size and $\chi_c$) same as the triangular lattice. When we increase the cut-off to $\chi_c = 48$, unstable values appear in the correlation at large distances. The situation, of course, improves if we push the computational effort further towards a higher cut-off $\chi_c = 64$, but certainly not to the level of MC. As it turns out, the convergence demands unusually high cut-off on the bond dimensions for such large system sizes costing a huge amount of computational resources.

In order to provide a critical assessment about the performance of TRG for simulating dimer models on different lattices, we calculate, for example, another quantity – the average dimer concentration $\langle d(R_i)\rangle$ – as a function of $\chi_c$. From the results of TRG method shown in Figure. 3.6(a), we observe that $\langle d(R_i)\rangle$ rapidly converges to $1/6$ for the dimer model on the triangular lattice as the cut-off $\chi_c$ is gradually being increased. This is evidently not the case for the dimer model on the square lattice as visible from Figure. 3.6(b). Even for small system sizes, the required stability in the numerical data requires cut-off like $\chi_c \sim 30$. If we try our hands in larger system sizes, more and more relevant information has to be stored in a pertinent basis since the convergence is attained at a much larger values of $\chi_c$. The failure is attributed to the fact that we truncate the sum over indices as in (3.4) at a threshold much below the required one, so the entanglement dies off gradually.

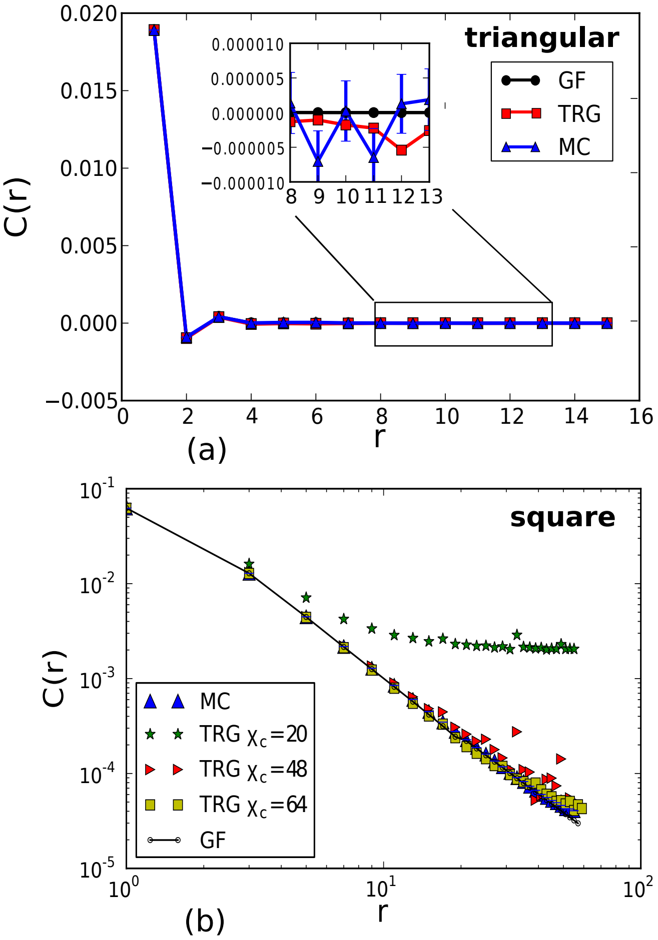

Figure 3.5: (Up): The dimer-dimer correlation on the triangular lattice as a function of the distance $r = |R_i - R_j|$. The plot shows data for an 128 × 128 cluster as extracted from the Green functions (GF), the TRG method, and the MC method. In the tensor network representation the bond dimension has been truncated at $\chi_c = 20$. (Down):The same function is plotted for a 128 × 128 square lattice cluster using the Green functions, the MC method and the TRG method with $\chi_c = 20, 48, 64$. That the cut-off is kept very high for required accuracy is attributed to the critical nature of the model on the square lattice.

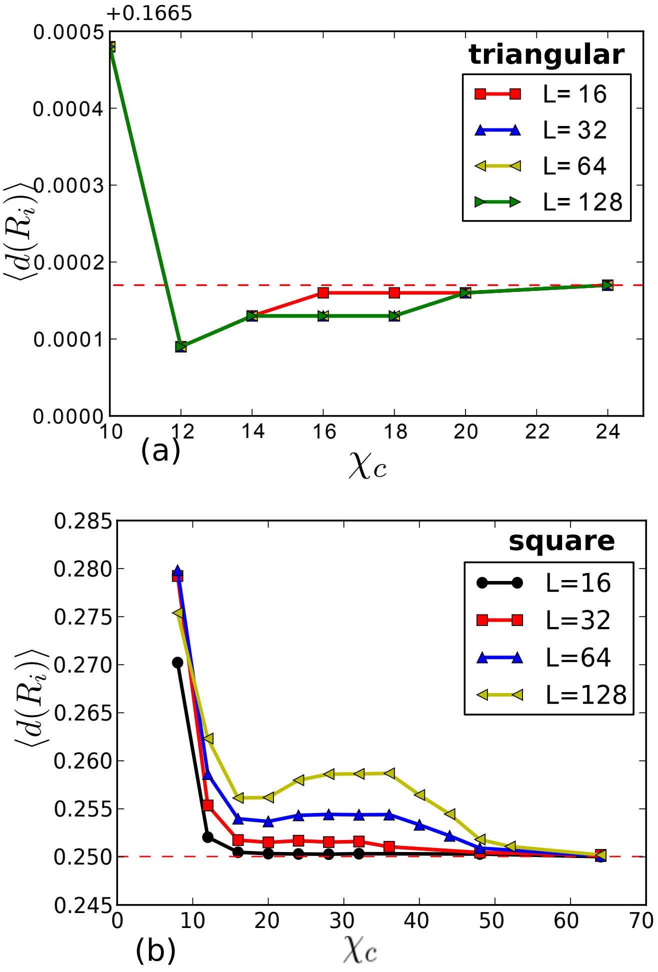

Figure 3.6: (Up): The dimer concentration as a function of the cut-off for different lattice sizes on the triangular lattice. The red dotted line indicates the average value of 1/6. (Down): Shown is the above quantity for the square lattice. The average value in this case is 1/4. Note the deviations from the dashed line for larger systems. The convergence requires larger cut-off which grows with the system size.

# Chapter 4

# Strongly Correlated Bosons on a Kagome Lattice

In the preceding chapter, we looked at the classical dimer models and analyzed their high temperature properties using tensor renormalization group technique. At low temperatures, quantum dynamics of the dimers needs to be taken into account which leads to the quantum version of the model – quantum dimer model (QDM) studied first by Rokhsar and Kivelson [Rokh 88] in context of high-$T_c$ superconductors. Rokhsar and Kivelson constructed the model on a square lattice which was later extended to non-bipartite lattices to find a novel topological order in the ground state [Moes 01a, Misg 02]. Exploring this type of orders has significant contributions to the modern age quantum computation. These dimer models provide the effective low-energy theories for different bosonic models with mutual short-range repulsions on various frustrated lattices. Over the past decades, they have attracted much attention as they present a set of rich phase diagrams [Heid 05, Isak 06b, Isak 06a]. A particularly interesting case is the kagome lattice where, for suitable fillings, a variety of numerical and analytical evidences now point to the existence of a topologically ordered $\mathbb{Z}_2$ liquid phase over an extended parameter regime [Bale 02, Shen 05]. The low-energy physics of such models in the strongly correlated limit is generically described by quantum dimer models (QDM) [Rokh 88] on triangular lattices. This latter class of Hamiltonians is known to harbor points in their parameter space, the so-called Rokhsar-Kivelson (RK) points [Rokh 88, Moes 01a], where $\mathbb{Z}_2$ topological order is present and strong numerical evidence for its stability exists [Moes 01a]. The intimate connection, on the other hand, between such hard-core boson models and $S = 1/2$ models with XXZ anisotropy [Isak 06a] also makes these models relevant to research in quantum magnetism.

In this chapter, we explore the strong-coupling physics of a hard-core boson model on kagome lattice with short-range repulsive interactions particularly for the filling factor $f = 1/3$. We show that the effective low-energy theory is given by a QDM Hamiltonian on a triangular lattice with two dimers emanating from each site of the triangular lattice. This effective theory is thus equivalent to a quantum fully packed loop (FPL) model [Blot 94] on a triangular lattice. Such kind of models in the classical version have been extensively studied on some of the bipartite lattices [Blot 89, Blot 94, Batc 94, Kond 95, Batc 96, Jaub 11]. The quantum FPL model on a square lattice has been studied by Shannon *et. al.* [Shan 04] where they showed a correspondence to the XXZ model on the checkerboard lattice in certain *easy-axis* limits. In what follows, using a combination of numerical techniques (tensor product states formalism and exact diagonalization on clusters), we analyze the FPL model on the triangular lattice. Our numerical analysis strongly advocates for a rich phase diagram consisting of an extended $\mathbb{Z}_2$ topological liquid phase as well as a crystalline phase, known as lattice nematic (LN) [Muld 10], that breaks the threefold rotational symmetry of the lattice (but not the translation symmetry). Taking clue from our numerical results, we then construct a critical theory for a continuous phase transition between the two phases. Unlike the usual theories of phase transition, this critical theory is not written in terms of the low-energy long wavelength fluctuations of the LN order-parameter, but naturally in terms of “fractionalized" Ising degrees of freedom sitting at the centers of the triangles of the kagome lattice. Mapping the problem to the language of Ising gauge theory [Kogu 79], we can isolate these critical degrees of freedom — the so-called *visons* [Sent 01] (Ising magnetic flux [Read 89]), whose condensation then describes the transition from the topological liquid to the LN. The order parameter is a bilinear in terms of the visons and hence, the above transition consists of an example of quantum criticality beyond the conventional Landau-Ginzburg-Wilson paradigm [Sent 04]. Our calculation predicts that the critical theory belongs to the $O(3)$ universality class.

## 4.1 Model Hamiltonian

We start by considering an extended Hubbard model of hard-core bosons on the sites of a kagome lattice given by the Hamiltonian

$$\mathcal{H} = \mathcal{H}_t + \mathcal{H}_V , \tag{4.1}$$

where

$$\mathcal{H}_t = -t \sum_{\langle i,j \rangle} (b_i^\dagger b_j + \text{H.c.}) \tag{4.2}$$

describes the nearest-neighbor hopping, with amplitude $t$, for the hard-core bosons that are created (annihilated) by $b_i^\dagger$ $(b_i)$ on the sites of the kagome lattice and

$$\mathcal{H}_V = V_1 \sum_{\langle i,j \rangle} n_i n_j + V_2 \sum_{\langle\langle i,j \rangle\rangle} n_i n_j + V_3 \sum_{\langle\langle\langle i,j \rangle\rangle\rangle} n_i n_j - \tilde{\mu} \sum_i n_i \tag{4.3}$$

denotes respectively the first ($V_1$), second ($V_2$) and third ($V_3$) neighbor repulsive interactions among the bosons ($n_i = b_i^\dagger b_i$) along with a chemical potential $\tilde{\mu}$ that fixes the particle number. Interesting physics emerges at rational fractional fillings $p/q$ (with $p$ and $q$ being mutually prime and $p < q$). We shall restrict ourselves to the specific fractional fillings of bosons which are $1/6$, $1/3$ and $1/2$.

At integer filling 0 or 1 there are only trivial product states possible (due to the hard-core constraint). At fractional filling factors and the presence of longer-range interactions very rich phase diagrams emerge. For example, at $1/3$ filling and strong nearest-neighbor repulsion ($V_1$), a plaquette ordered state [Isak 06a] is formed, while for $1/2$ filling a uniform

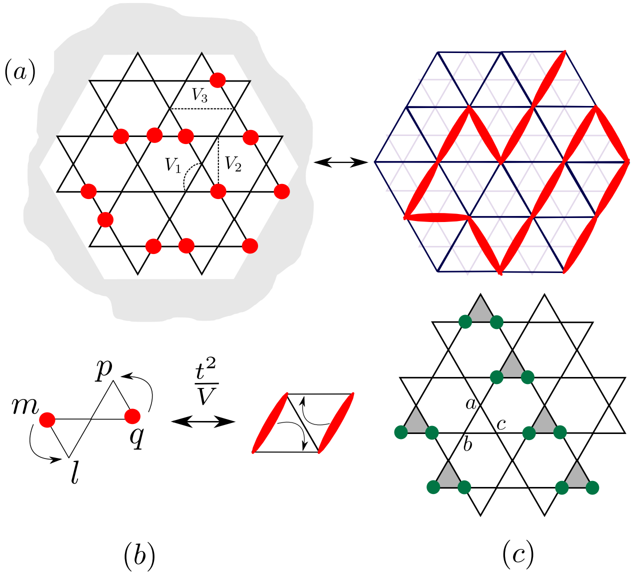

Figure 4.1: (a) Mapping from the 1/3 filled bosonic problem on kagome to FPL on the triangular lattice. Each particle on the kagome lattice is mapped to a loop segment on the triangular lattice that is obtained by connecting the centers of the kagome hexagons. The strength of the 1st, 2nd and 3rd repulsive interactions are denoted as $V_1$, $V_2$ and $V_3$ respectively. The limit of $V_1 = V_2 = V_3 = 2V$ is the focus of this paper. Panel (b) demonstrates the allowed lowest order processes in $t/V$ (see the text). (c) Shown is the sublattice used for the gauge transformation that changes the sign of $g$ in (4.5) as described in the text. The sublattice is constructed by the $b$ and $c$ sites of the shaded unit cells.

superfluid persists for all values of $V/t$. When turning on farther neighbor interactions given by $V_2$ and $V_3$, additional insulating lobes emerge at different fractional fillings [Bale 05]. Many of these bosonic insulators at fractional fillings can host interesting quantum phases with or without spontaneously broken symmetry. In the following, we focus on the strong-coupling phases occurring in the 1/2, 1/3 and 1/6 lobes, with a particular focus on the 1/3 lobe and show that topological as well as long-ranged ordered phases can emerge.

To this end we look at the strong-coupling limit of the above Hamiltonian. For $t = 0$, and $V_1 = V_2 = V_3 = 2V$, the interaction term can be written as

$$\mathcal{H}_\mathrm{V} = V \sum_{\{\hexagon\}} \left[ \left( n_{\hexagon} - \frac{\mu}{4V} \right)^2 - \frac{\mu^2}{16V^2} \right] , \tag{4.4}$$

where $\mu = \tilde{\mu} + 2V$ is the effective chemical potential and $n_{\hexagon}$ is the number of particles in each of the hexagons of the kagome lattice. It is clear from (4.4) that for $\mu = 4V, 8V, 12V$, $\mathcal{H}_\mathrm{V}$ is minimized by having 1, 2, 3 bosons per hexagon respectively (or alternatively filling fraction of $f = 1/6, 1/3$ and $1/2$ respectively). Clearly there are many different configurations of bosons that satisfy the above constraint, however, we note that since the hexagons share sites, the configurations for different hexagons are not completely independent.

An insight to the number of states spanning the ground state sector of $\mathcal{H}_V$ for the above commensurate fillings can be obtained from the one-to-one correspondence between the ground state configurations of the bosons and the hard-core dimer coverings on the triangular lattice obtained by joining the centers of the hexagons of the kagome lattice as shown in Figure. 4.1(a). Thus each site of the kagome lattice lies on a bond of the triangular lattice and the presence (absence) of a boson on that site can then be identified uniquely with the presence (absence) of a dimer on the corresponding bond of the triangular lattice. This immediately shows that at 1/6 filling, the number of ground state bosonic configurations allowed by $\mathcal{H}_V$ is equivalent to the number of hard-core dimer coverings on the triangular lattice which is known to be extensive ($\sim 1.5^N$) in the system size, $N$ (an estimate [Fend 02] based on Pauling's approximation [Paul 35] gives $\sim 1.34^N$). Similarly 1/2 filling can be cast into a 3-dimer (three non overlapping dimers emerging from each site) problem m on the triangular lattice [Bale 02] where the Pauling estimate suggests that the extensive degeneracy of the ground state is $\sim 1.84^N$.

In the case of 1/3 filling, which is the specific interest of the present paper, we obtain the equivalent fully-packed loop (FPL) model on the triangular lattice with two non-overlapping dimers emanating from each site and the dimers form non-intersecting loops as shown in Figure. 4.1(a). Here the Pauling estimate shows that the number of loop configurations scales with system size as $\sim 1.7^N$. Thus, in all the above cases, for $t = 0$, as expected, the ground state is macroscopically degenerate and has a finite zero temperature entropy (see Appendix B.1 for an estimate). Throughout the rest of this work, we shall exploit the above equivalence between the bosons and the dimers and shall mostly use the language of the dimers, translating back to the bosons whenever applicable.

### 4.1.1 Effective model in the strong-coupling limit

Small but non-zero hopping ($t$) induces quantum fluctuations that (e.g., in the form of local ring exchange around small plaquettes [Thou 65, Para 02, Bern 04, Rung 04]) can lift the extensive ground state degeneracy by quenching the entropy of the classical model ($t = 0$) either by spontaneously breaking one or more symmetries of the system (quantum *order by disorder* [Vill 80, Shen 82]) or more interestingly, by generating a long-ranged quantum entangled state that does not break any symmetry of the Hamiltonian (quantum *disorder by disorder* [Prio 01, Powa 13]) but can have non-trivial “topological order". In this work, we shall show examples of both the routes taken by the bosons on the kagome lattice.

To derive the effective Hamiltonian in the strong-coupling limit, we treat $t/V$ as a small perturbation parameter to obtain (to the leading order in $t/V$) [Bale 02]

$$\mathcal{H}_{\text{eff}} = -g \sum_{\alpha} (b_p^{\alpha\dagger} b_l^{\alpha\dagger} b_m^{\alpha} b_q^{\alpha} + \text{H.c}) \, , \tag{4.5}$$

where $g = t^2/V$ and $p$,$q$,$l$ and $m$ are the corner sites of the bow-tie labeled by $\alpha$ referring to Figure. 4.1(b). The sum includes all bow-ties that are related by the $C_3$ symmetry. The center of the bow tie may or may not be occupied by a boson in the case of 1/3 and 1/2 filling. Furthermore the sign of $g$ in (4.5) can be altered by using a simple gauge transformation that multiplies all configurations with the factor $(-1)^{N_{\text{sub}}}$ where $N_{\text{sub}}$ is the number of particles in the sublattice shown in Figure. 4.1(c).

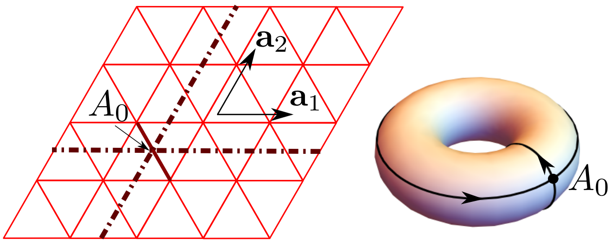

Figure 4.2: The triangular lattice is put on a torus by setting periodic boundary conditions along two independent directions given by the lattice vectors $\mathbf{a}_1$ and $\mathbf{a}_2$. $A_0$ denotes the intersection point (a link on the lattice) of the two non-contractible loops on the torus. There are four topological sectors characterized by the doublets $(0,0)$, $(0,1)$, $(1,0)$ and $(1,1)$ [Moes 01a, Ralk 05]. The local Hamiltonian in (4.7) can not mix configurations from different topological sectors hence, block diagonal in the full configuration basis.

### 4.1.2 Dimer representation of the effective Hamiltonian

We now recast (4.5) using the particle to dimer mapping mentioned in the previous section. In terms of the dimers, the effective Hamiltonian corresponds to the kinetic term of the QDM [Moes 01a],

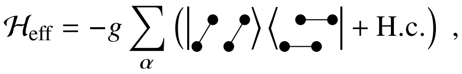

$$\mathcal{H}_{\rm eff} = -g \sum_{\alpha} \left( \big|\,/\,/\,\big\rangle \big\langle\,=\,\big| + \text{H.c.} \right) , \qquad (4.6)$$

where the sum is over all rhombus shaped plaquettes ($\alpha$) on the triangular lattice.

In addition to the kinetic term (above) the generic QDM also includes the RK potential term [Rokh 88], which energetically favors configurations with plaquettes having parallel dimers. Such potential terms are representative of higher order (four boson) terms that can be generated in the strong-coupling expansion in $t/V$ of the underlying boson model. However, here we simply use this term as a free tuning parameter in the model. The full Hamiltonian of the QDM is written as

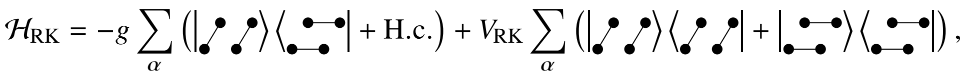

$$\mathcal{H}_{\rm RK} = -g \sum_{\alpha} \left( \big|\,/\,/\,\big\rangle \big\langle\,=\,\big| + \text{H.c.} \right) + V_{\rm RK} \sum_{\alpha} \left( \big|\,/\,/\,\big\rangle \big\langle\,/\,/\,\big| + \big|\,=\,\big\rangle \big\langle\,=\,\big| \right) , \qquad (4.7)$$

where positive (negative) $V_{\rm RK}$ denotes repulsive (attractive) interaction between the parallel dimers in a given plaquette. We emphasize that the low-energy effective Hamiltonian in the strong-coupling limit generally assumes the RK form irrespective of the filling fraction of the bosons (or the equivalent dimer models: QDM, FPL or the 3-dimer model respectively for $f = 1/6, 1/3$ and $1/2$) considered, albeit with important implications for the stability and nature of both the liquid and the solid phases which are summarized in Figure. 4.3. With this general formulation we now specialize to the physics of the Mott lobe for $1/3$ filling.

## 4.2 Numerical calculations at $1/3$ filling

We use a combination of tensor product states (TPS) formalism and exact diagonalization (ED) methods to obtain the phase diagram (Figure. 4.3 middle line) of the FPL model

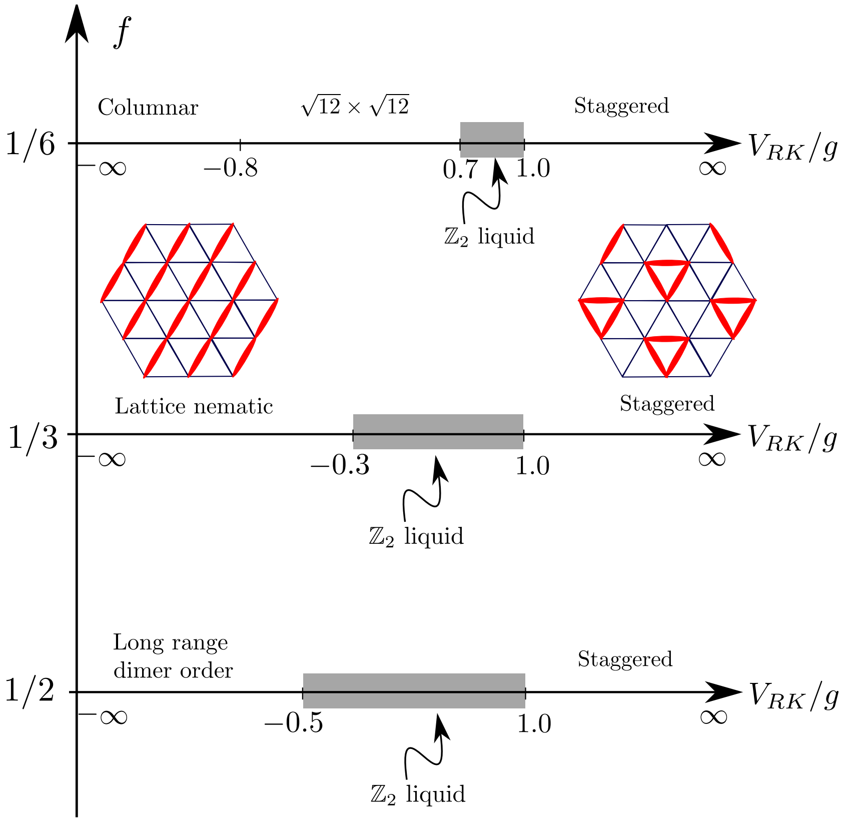

Figure 4.3: The phase diagram of the dimer models at different fractional fillings $f$ (see Ref. [Moes 01a] for $f = 1/6$ and Ref. [Shen 05] for $f = 1/2$). The important details about each of them are given in the text. The focus of the present paper is at $f = 1/3$.

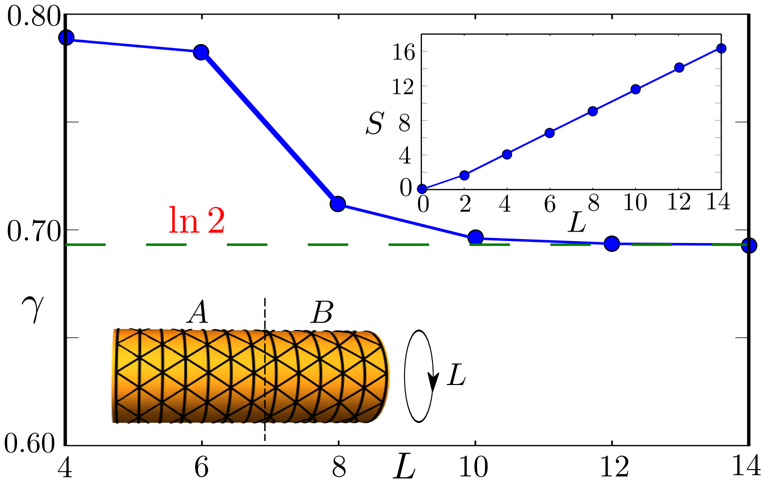

Figure 4.4: The plot shows the finite size dependence of the topological entanglement entropy $\gamma$ as a function of $L$, the perimeter of the subsystem $A$. The green dashed line corresponds to the saturated value of $\ln 2$ in the thermodynamic limit. The lattice is constructed on an infinite cylinder assuming periodic boundary condition in one direction. The black dashed line indicates the bipartition of the cylinder separating the subsystem $A$ from the rest $B$. The inset shows the linear growth of the entanglement entropy $S$ with $L$.

on the triangular lattice. Necessary details about implementing the numerical methods for different clusters are furnished in the following subsections facilitating a systematic analysis of our model. The value of $g$ is taken to be 1 which is a convenient choice for further numerical calculations.

### 4.2.1 Entanglement entropy at the RK point: the $\mathbb{Z}_2$ liquid

One notable feature of the Hamiltonian in (4.7) is the existence of the exactly solvable RK point ($g = V_{\text{RK}}$). We start by showing that at this point the ground state of our model (FPL) indeed has a topological order.

In order to characterize the topological order, an instructive quantity to look at is the entanglement entropy ($S$) for a bipartition of the system into two parts $A$ and $B$. The entanglement entropy of the reduced density matrix $\rho_A$ of subsystem $A$ is defined as $S = -\text{Tr}\left[\rho_A \log \rho_A\right]$ where $\rho_A$ is obtained from the full density matrix by tracing out all the degrees of freedom in the rest ($B$). For a gapped and topologically ordered gapped ground state, $S$ satisfies the “area law" with corrections

$$S(L) = \alpha L - \gamma + O(L^{-1}) + \cdots , \tag{4.8}$$

where $\alpha$ in the leading term is a non-universal coefficient and $L$ is the perimeter of the subsystem A. The sub-leading term $\gamma$, also known as the topological entanglement entropy [Kita 06, Levi 06, Amic 08, Eise 10], is, however, universal bearing the anyonic content of the state that reflects the topological order. This is directly related to the total quantum dimension (D) of the underlying topological field theory as $\gamma = \log D$. Since $D = 2$ for a gapped $\mathbb{Z}_2$ liquid (described by the $\mathbb{Z}_2$ gauge theory), the quantity $\gamma$ in (4.8) saturates to $\log 2$ in the thermodynamic limit i.e. $L \to \infty$.

The ground state at the RK point can be exactly represented by tensor networks (TN) using the framework of projected entangled-pair states (PEPS) [Vers 04, Cira 11]. Earlier we saw in chapter 3 that such kind of TN construction is very useful for determining the physical properties of a quantum system if the state is exactly known. There we gave a detailed account on a tensor network based algorithm, called tensor renormalization group, which can be very efficiently applied to the quantum dimer model at the RK point. In principle, the same algorithm can also be employed to find out the loop-loop correlation function in the FPL model which also, being gapped, qualifies as a suitable platform for TRG to apply. However, the quantity of interest to probe a gapped $\mathbb{Z}_2$ liquid is the topological entropy for which another TN based technique, called PEPS, proves to be extremely useful and easily implementable details of which can be found in Ref. [Orus 14]. We use this construction on a cylindrical triangular lattice (Figure. 4.4) to calculate $S$ as a function of $L$ and obtain $\gamma$ using (4.8). The subsystem $A$ is constructed by bipartitioning the semi-periodic triangular lattice with the dashed line as shown in Figure. 4.4. The circumference $L$ of the cylinder enters (4.8) as the perimeter of the subsystem and should be much larger than the maximum correlation length associated with the state [Jian 12, Jian 13]. The inset of Figure. 4.4 shows the expected linear growth of $S$ with $L$ that is predicted by the leading term in (4.8). The topological entanglement entropy ($\gamma$) is extracted from the intersection of the function $S$ on the $y$-axis when extrapolated backward and plotted against different values of $L$. The tendency of $\gamma$ to saturate at the value of $\log 2$ for large $L$ indicates to the fact that the RK point for the FPL model on the triangular lattice represents the ground state of a topologically ordered $\mathbb{Z}_2$ liquid akin to the other dimer models at $1/6$ and $1/2$ fillings [Furu 07, Isak 11]. This is one of the main results of this work.

However, away from the RK point in the accessible parameter space, the ground state is no longer exactly known. We adopt ED techniques to infer that the topological liquid is stable even away from the RK point over a finite window (see Figure. 4.3) up till when the system undergoes a quantum phase transition into the LN phase beyond a critical value of $V_{\text{RK}}$. In the following subsections, we present the ED results containing the information about the low-lying spectrum of the model and measurements of various correlation functions that reflect the salient features of the phase diagram depicted in Figure. 4.3 middle line.

### 4.2.2 Dimer-dimer correlation and the LN order

At the RK point, the loops are strongly fluctuating and the dimer-dimer correlations decay exponentially (as opposed to the algebraic decay on the square lattice) like the one in the QDM at $1/6$ filling. This indicates the lack of long-range dimer order, as expected, in the $\mathbb{Z}_2$ liquid phase. To check this, we calculate the dimer-dimer correlation function

$$C_{ij}(|\mathbf{r}_i - \mathbf{r}_j|) = \langle n(\mathbf{r}_i) n(\mathbf{r}_j) \rangle - \langle n(\mathbf{r}_i) \rangle \langle n(\mathbf{r}_j) \rangle \,, \tag{4.9}$$

using ED on different clusters. Here $n(\mathbf{r}_i)$ is the dimer occupation number on $i^{\text{th}}$ link of the triangular lattice specified by the position vector $\mathbf{r}_i$. Each cluster has an extension of $L_x$ along the unit vector $\mathbf{a}_1 = (1, 0)$ and $L_y$ along the unit vector $\mathbf{a}_2 = (\frac{1}{2}, \frac{\sqrt{3}}{2})$ (see Figure. 4.2).

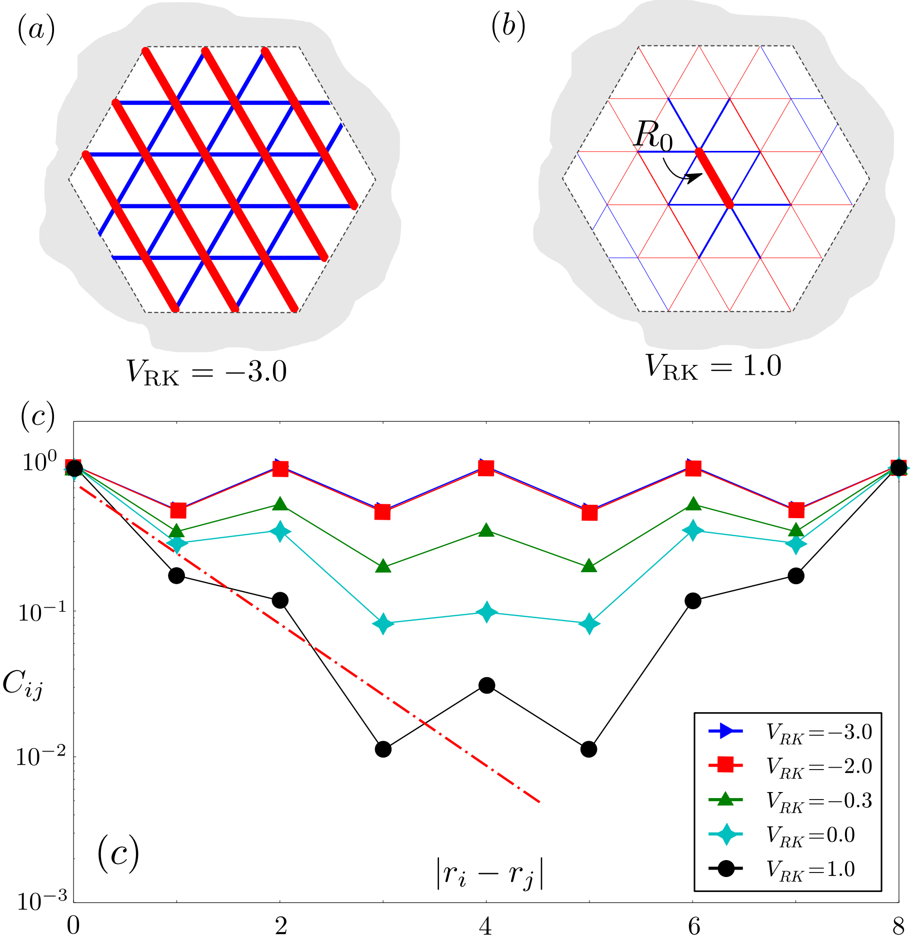

Figure 4.5: (a) The real space dimer-dimer correlation is plotted on a triangular lattice cluster at $V_{\mathrm{RK}} = -3.0$ which indicates the parallel loop pattern deep into the LN phase. (b) Same is plotted for $V_{\mathrm{RK}} = 1.0$ showing the exponential decay of the dimer-dimer correlation function in the liquid phase at the RK point. The reference link, with respect to which correlations at all the other links are measured, is denoted by $R_0$. Red and blue links stand for positive and negative correlation respectively while the width measures the correlation strength. (c) Plotted is the same correlator as a function of $|r_i - r_j|$ at different RK potential. The red dashed line represents an approximate exponential fit $e^{-r/\xi}$ for $\xi \sim 1.0$.

Although the considered clusters are small, the numerical results shown in Figure. 4.5(c) suggest that the correlator (as a function of $r \equiv |\mathbf{r}_i - \mathbf{r}_j|$) is indeed exponential at the RK point with the correlation length $\xi \sim$ one lattice spacing. This is a known result for the case of the QDM on a triangular lattice (or equivalently the $1/6$ filling) [Moes 01a]. As mentioned earlier, at the RK point the model is exactly solvable and all the quantum correlations can be calculated classically i.e. by using classical numerical techniques as explained in details in the previous chapter. The real space realization of the dimer correlation function at the RK point is shown in Figure. 4.5(b) which points to an exponentially decaying nature of the correlation function as expected. The red and blue bonds correspond to the positive and negative correlation respectively with the width of the bond being proportional to the absolute value of the correlation function.

The exponential decay disappears as $V_{\mathrm{RK}}$ is taken to large negative values till we get into a phase with long-range dimer-dimer correlations with $C(r) \simeq (-1)^r \frac{1}{4}$ (up to an offset) deep inside this phase signaling the onset of long-range dimer order. To explore the nature of this long-range ordered phase we plot the real space dimer-dimer correlation function in Figure. 4.5(a). The plot suggests that the ordered phase is characterized by parallel alignments of loops on the triangular lattice which does not break any translation symmetry but the threefold rotational symmetry (corresponding to the threefold quasi-degeneracy in the ground sate of the spectrum). Since the parallel loops do not have an orientation along the direction of their alignment, we refer to this as the LN phase.

### 4.2.3 The phase transition between the $\mathbb{Z}_2$ liquid and the LN

Having characterized the $\mathbb{Z}_2$ liquid phase (by non-trivial entanglement entropy and short-range dimer-dimer correlations) and the LN phase (by long-range dimer-dimer correlation), we now focus on the quantum phase transition between the two phases. First we study the excitation gap in the liquid with ED and observe that the gap closes only at a finite distance from the RK point (see Figure. 4.6). Thus the $\mathbb{Z}_2$ topological liquid persists over the whole region from $V_{\mathrm{RK}} = 1$ to $V_{\mathrm{RK}} \sim -0.3$ which suggests that alone the kinetic term in (4.7) can potentially stabilize the liquid phase even for $V_{\mathrm{RK}} = 0$. The continuous vanishing of the gap near $V_{\mathrm{RK}} = -0.3$ gradually destroys the liquid state driving the system into a charge-ordered LN phase as suggested from the behavior of the density-density correlation function shown in Figure. 4.5(c).

A generic way to locate the critical point within ED is to look at the response function of the system as a function of the parameters that define the Hamiltonian in (4.7). In our case, an equivalent quantity can be framed using the second derivative of the ground state energy with respect to the RK potential: $-\delta^2 E_g/\delta V_{\mathrm{RK}}^2$. This is plotted in Figure. 4.7 where the single peak in the response is visible approximately at $V_{\mathrm{RK}} \sim -0.3$. This shows that a single transition separates the topological liquid and the LN. While it is impossible to rule out the possibilities of a first order transition from our finite cluster results, the smooth and gradual increase of the response along with the absence of shoulders suggests that the transition between the liquid and the LN may be continuous or weakly first order (the system sizes considered here do not allow for a definite statement). The full energy spectrum of each of the clusters (not shown) suggests that at large negative $V_{\mathrm{RK}}$, the ground state becomes nearly threefold degenerate (the quasidegeneracy is attributed to finite-size

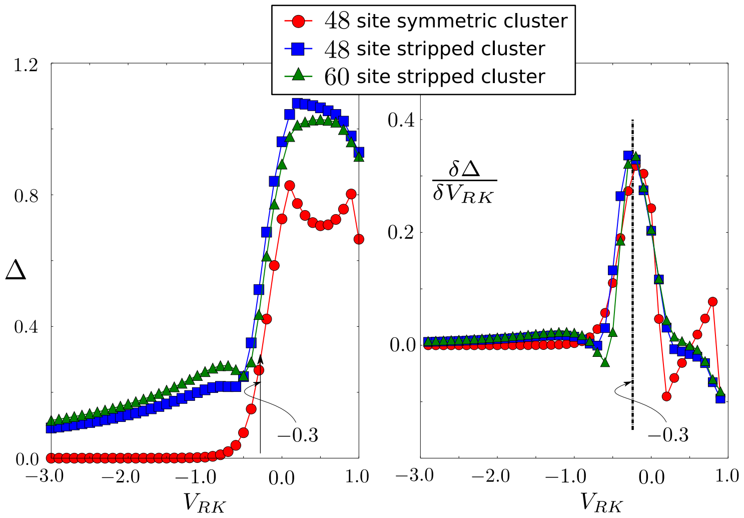

Figure 4.6: In the left panel, the gap to the first excited state tends to vanish at $V_{\mathrm{RK}} \sim -0.3$ for different symmetric and stripped clusters. The ground state always lies in the zero-flux sector (0,0) for all of them. In the right panel, the derivative of the gap is plotted as a function of $V_{\mathrm{RK}}$ to locate the transition point at $V_{\mathrm{RK}} \sim -0.3$.

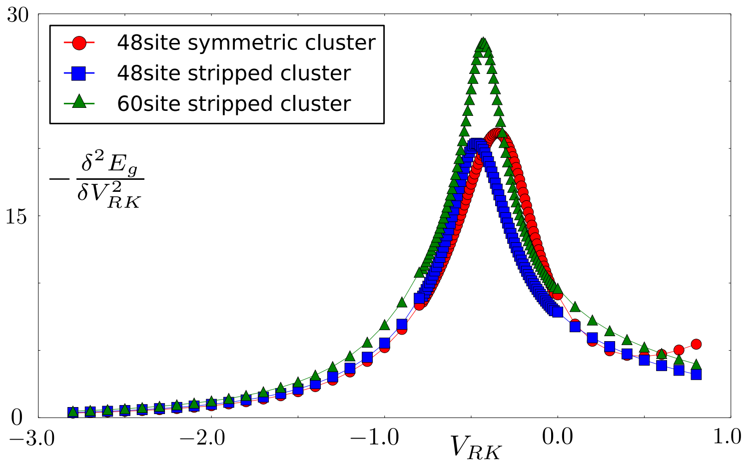

Figure 4.7: The ground state susceptibility $-\delta^2 E_g/\delta V_{\mathrm{RK}}^2$, in the (0,0) sector indicates a continuous phase transition between two phases for different clusters. The transition point is close to $V_{\mathrm{RK}} \sim -0.3$ as evident from the right panel of Figure. 4.6.

effect) where the three states are formed by superposition of the three loop patterns allowed by the $C_3$ symmetry. We conclude on our numerical results from ED by noting that as the system gradually enters the ordered phase crossing the transition point, a set of three states in the bottom of the spectrum starts separating from the rest. Deep inside the LN phase, these three states become nearly degenerate (up to the finite size effects) with a finite excitation gap which is much higher in magnitude than the liquid gap and scales linearly with $V_{\text{RK}}$. This quasidegeneracy is exact in the thermodynamic limit where the $C_3$ symmetry is spontaneously broken.

Having established the two phases and the possibility of a continuous phase transition between them, we now explore the critical theory for the predicted critical point (at $V_{\text{RK}} \sim -0.3$). We note that such a continuous transition would be very interesting in the sense that it describes the destruction of a topologically ordered phase towards the development of a conventionally symmetry broken phase.

# Chapter 5

# Gauge Theory for the Fully Packed Loop Model

Before we illustrate our FPL model in gauge theoretic language, it is instructive and worth recalling the generic gauge structure of the dimer models which is particularly important for describing the excitations in the topological liquid phase. This is partly discussed in chapter 2 where we mentioned that quantum dynamics of the QDM on a triangular lattice or the equivalent bosonic model on the kagome lattice can be effectively described by an Ising gauge theory (IGT) in $(2+1)$ dimensions [Sent 00, Moes 01c, Frad 13]. Such a gauge theory is constructed via duality mapping which transforms the original problem to a model of Ising gauge fields on the dual lattice. As an example, the Ising (or $\mathbb{Z}_2$) gauge fields ($v^z$) corresponding to the QDM on the triangular lattice are defined on the dual honeycomb lattice with the Hamiltonian [Slag 14]

$$\mathcal{H}_G = -\sum_I K v_I^x - \sum_{<IJ>} h\rho_{IJ} v_I^z v_J^z + \cdots . \tag{5.1}$$

The Ising variables $v^{x,z}$ represent the vison excitations which dwell on the sites (denoted as $I, J$) of the honeycomb lattice. The ellipsis in (5.1), in principle, includes all terms that are allowed by the projective symmetry group (PSG) thorough which the visons transform. The gauge potential $\rho$ satisfies a crucial constraint on the hexagonal plaquette of the honeycomb lattice: $\prod_{\langle IJ\rangle \in \hexagon} \rho_{IJ} = \pm 1$ which subdivides the Ising gauge theory into the even$(+1)$ and the odd$(-1)$ classes. The QDM on the triangular lattice belongs to the odd Ising class for which the gauge theory represents a *fully frustrated transverse field Ising model* whereas our FPL model belongs to the even Ising class corresponding to the *ferromagnetic transverse field Ising model*. In what follows, we will see that the classification has important implications in the low-energy physics of the models which reflects in the phase diagram given in chapter 4. Particularly for the FPL model, the gauge theory indicates to a direct transition from the topological liquid phase to the crystalline LN phase in contrast to the intervening plaquette phase for the QDM. In this chapter we focus on such an unconventional quantum phase transition and attempt the critical theory within the Landau-Ginzburg prescription [Land 80, Ma 00]. To construct a theory for the continuous phase transition between the $\mathbb{Z}_2$ liquid and the LN phases, we now introduce an alternative spin representation of the hard-core boson model (or the equivalent dimer model) which is the first crucial step to see the emergence of the IGT in the FPL model. We note that the procedure is generically true for all the filling fractions which we considered in chapter 4.

## 5.1 Spin representation and the gauge theory

To obtain such a description, we first identify a spin $1/2$ degree of freedom on each site of the kagome lattice by virtue of the well known mappings: $b_i^\dagger = \sigma_i^+$, $b_i = \sigma_i^-$ and $n_i = (\sigma_i^z + 1)/2$ where an up (down) spin represents the presence (absence) of a boson at the lattice site. Equation (4.4), then, becomes

$$\mathcal{H}_{\rm V} = V \sum_{\{\hexagon\}} (\frac{1}{2}\sigma^z_{\hexagon} + h)^2 - \mu^2 N_{\hexagon}/16V \;, \tag{5.2}$$

where $N_{\hexagon}$ is the total number of kagome hexagons and $h = 3 - 6f$. The sum of all spin moments in a given hexagon is denoted by $S^z_{\hexagon} \equiv \frac{1}{2}\sigma^z_{\hexagon}$ where $\sigma^z_{\hexagon} = \sum_{i\in\hexagon}\sigma^z_i$. Clearly in the spin description, different fillings of bosons $(f)$ correspond to different integer values of $h$ which essentially plays the role of an external magnetic field. Lowest energy configurations of the spin system specified by (5.2) satisfy the constraint that sum of the moments in every hexagon is exactly opposite to $h$ which depends on the filling factor $f$. Thus for $f = 1/6, 1/3, 1/2$; $h = 2, 1, 0$ and hence the potential term is satisfied if the total magnetization per hexagon at these fillings is $S^z_{\hexagon} = -2, -1, 0$ respectively, corresponding to having one, two or three up spins (which means the presence of one, two or three bosons as expected) per hexagon.

## 5.2 Effective spin model

In terms of the spins, the effective Hamiltonian (in [4.5]) representing the dynamics within the degenerate ground state manifold of $\mathcal{H}_{\rm V}$ is given by,

$$\mathcal{H}_{\rm eff} = \sum_{\alpha} \hat{\mathcal{P}}_\alpha \left[ -g \prod_{\alpha} \sigma^x + V_{\rm RK} \right] . \tag{5.3}$$

Each term in (5.3) involves a product of four spins that form a bow-tie, as shown in Figure. 5.3(a). The projector which selects out the flippable bow ties is expressed as [Bale 02]

$$\hat{\mathcal{P}}_\alpha = \sum_{\xi\pm 1} \prod_{a\in\alpha} \left( \frac{1}{2} + \xi(-1)^a \sigma^z_a \right), \tag{5.4}$$

and we have also added the potential term in (5.3) to recover the RK Hamiltonian given in (4.7).

When the first term in (5.3) dominates, the system prefers to align all the spins in the $\sigma^x$ direction and hence the boson number per site fluctuates. This is indeed the salient feature of a $\mathbb{Z}_2$ liquid phase (see below). On the other hand when the second term dominates, the system prefers to choose a pattern to order in the $\sigma^z$ direction and we have a long-range order in the boson density which turns out to be the LN phase that we discussed before. The actual magnitude of the coupling constants for which the transition between the two phases takes place depends on the details of the microscopic model.

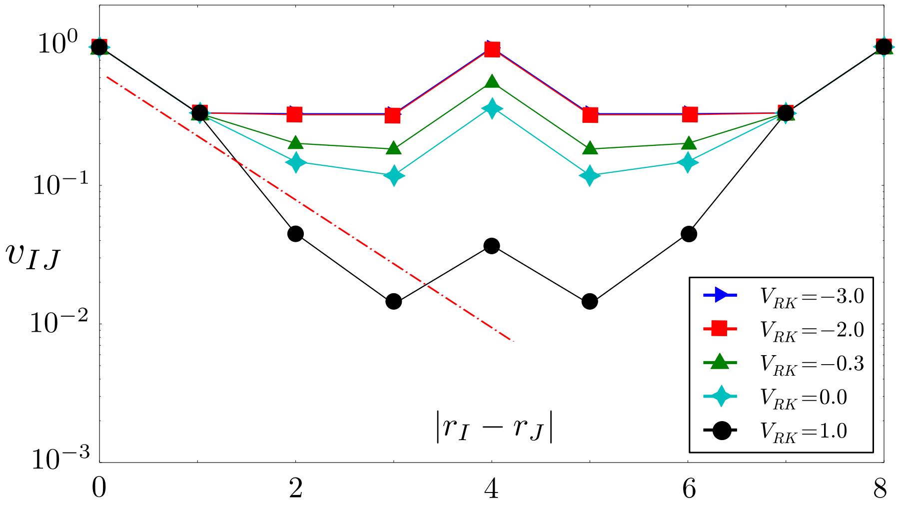

Figure 5.1: The two-vison correlator as a function of $|r_I - r_J|$ at different values of $V_{\mathrm{RK}}$ for a symmetric cluster of $L = 4$. The red dashed line represents an exponential decay: $e^{-|r_I - r_J|/\xi}$ for $\xi \sim 0.7$.

## 5.3 Ising gauge theory, visons and vison correlator

Each spin sitting at the site of the kagome lattice is a part of two hexagonal plaquettes. We can define the Ising variables $\epsilon_h = \pm 1$ for each such hexagonal plaquette. Clearly the Hamiltonian in (5.3) is invariant under the $\mathbb{Z}_2$ gauge transformation [Bale 02]

$$\sigma_i^x \to \epsilon_h \sigma_i^x \epsilon_{h'} \;, \tag{5.5}$$

where $h$ and $h'$ denotes the two hexagons of which the site $i$ is a part of. Such an Ising gauge structure, generated by the gauge transformations $\mathcal{G}_h = \exp[i\pi S^z_{\hexagon}]$, is an emergent property of the low-energy subspace [Bale 02] of the original microscopic bosonic Hamiltonian in (4.1) in the strong-coupling limit ($V \gg t$). Indeed the above Hamiltonian represents an Ising gauge theory where the plaquette term $\mathcal{F}_{\triangle} = \left(\sigma_1^x \sigma_2^x \sigma_5^x\right)$ and $\mathcal{F}_{\triangledown} = \left(\sigma_5^x \sigma_3^x \sigma_4^x\right)$, shown in Figure. 5.3(a), measures the Ising magnetic flux through each triangle of the kagome lattice.

The operator $\sigma_i^z$ creates two such magnetic fluxes on the two triangles of the kagome lattice of which it is a part of. Such Ising flux excitations have been dubbed *visons* as we noted in chapter 2. One can create a single vison excitation [Bale 02] by applying a product of $\sigma^z$ operators along any path $C$ starting from any site of a given triangle of the kagome lattice to infinity:

$$v_I^z = \prod_C^{I\to\infty} \sigma_i^z \;, \tag{5.6}$$

where $i$ is a kagome lattice site encountered on the path $C$ which runs from the corresponding triangular kagome plaquette $I$, where the vison resides, to spatial $\infty$. Since the path operators *commute* with each other, it is straightforward to show that the two-vison wave function is symmetric under the exchange of the visons, or in other words, the visons are bosons themselves. With reference to the dimer covering, the above operator is nothing but the number of dimer variables encountered along the path. This immediately implies that the vison-vison correlator is given by [Ivan 04, Stru 11]

$$\langle v_I^z v_J^z \rangle = \langle \prod_{C}^{I \to J} \sigma_i^z \rangle \equiv v_{IJ} \ , \tag{5.7}$$

(where the path $C$ runs from $I$ to $J$) which translates to

$$\langle v_I^z v_J^z \rangle = \langle (-1)^{N_{IJ}} \rangle \ , \tag{5.8}$$

where the operator $N_{IJ}$ counts the total number of dimers encountered on the path $C$ from $I$ to $J$ in any given dimer configuration. It is easy to verify that the explicit expressions of the vison operators in terms of the spins given in (5.10) are independent of the contour $C$ up to an overall sign that can be fixed by measuring the correlator with respect to a fixed reference dimer configuration.

In the $\mathbb{Z}_2$ liquid phase, where $\mathcal{F}_\triangle = \mathcal{F}_\triangledown = +1$, the vison excitations have a finite gap and the ground state does not contain free visons. On the other hand, the phase characterized by $\langle \sigma^z \rangle \neq 0$, which we shall show is the LN phase, is a vison condensate. Thus we expect that the transition between the $\mathbb{Z}_2$ liquid and the LN is described by the closing of the vison gap leading to the vison condensation. Hence, the ground state expectation value of the vison correlator should also decay exponentially in the liquid phase with a length scale proportional to the inverse of the vison gap while it should have asymptotically reached a constant value in the LN phase.

In Figure. 5.1 we show the two-vison correlation function at different values of $V_{\text{RK}}$. The data at $V_{\text{RK}} = 1.0$ fits well with the exponential curve $e^{-|r_I - r_J|/\xi}$ for $\xi \sim 0.7$. As $V_{\text{RK}}$ is decreased further, the system gradually enters the ordered phase and the two-vison correlator becomes asymptotically constant. This behavior is expected, as we shall show below. Note that in Figure. 5.1, close to $V_{\text{RK}} = -0.3$ the value of $v_{IJ}$ changes by an order of magnitude much in a similar way that the density-density correlation does in Figure. 4.5.

## 5.4 Lattice description for the visons

Our numerical results indicate that the phase transition between the $\mathbb{Z}_2$ liquid and the LN phase, driven by the condensation of vison excitations, is possibly continuous. We shall now derive an effective critical theory for such a continuous transition. This would then compliment our numerical understanding of the phase diagram of the microscopic model.

In the spirit of the universality of continuous phase transitions, to this end, we perform a series of mappings to isolate the vison degrees of freedom which we use to describe the critical theory for the transition. The effective Hamiltonian in (5.3) can be obtained (see Appendix B.2) from

$$\tilde{\mathcal{H}}_{\text{eff}} = -g_{\text{eff}} \sum_{\alpha} (\mathcal{F}_\triangle^{(\alpha)} + \mathcal{F}_\triangledown^{(\alpha)}) + V_{\text{eff}} \sum_{\hexagon} \left( S_{\hexagon}^z + h \right)^2 + u_{\text{eff}} \sum_{\alpha} \mathcal{P}_\alpha \tag{5.9}$$

in the limit of $g_{\text{eff}}/V_{\text{eff}}, u_{\text{eff}}/V_{\text{eff}} \to 0$ ($g_{\text{eff}}, V_{\text{eff}} > 0$) where the leading term is obtained in the second order perturbation theory with $g \sim g_{\text{eff}}^2/V_{\text{eff}}$ and $u_{\text{eff}} \sim V_{\text{RK}}$. We immediately note that the last two terms in (5.9) *commute* with each other as expected and hence, in the regime $|u_{\text{eff}}| \gg g_{\text{eff}}$ (and $V_{\text{eff}}$ being the largest energy scale), the above model is rendered classical and the $u_{\text{eff}}$ term chooses an appropriate order that is consistent with the filling (i.e., allowed by $V_{\text{eff}}$). For $u_{\text{eff}} < 0$, this favors the order as depicted in Figure. 5.3(c). On the other hand, when $|u_{\text{eff}}| \ll g_{\text{eff}}$, this order is expected to melt due to the quantum fluctuations in the spins. In particular, a state which allows flipping of spins in closed loops while maintaining the filling constraint becomes favorable. This is indeed consistent with the picture of the $\mathbb{Z}_2$ liquid of the microscopic model which is exact at the RK point.

To arrive at the critical theory describing the vison condensation, we exploit the gauge structure, described in the last sub-section, of the effective theory to isolate the vison degrees of freedom. At this point, we introduce the honeycomb lattice which is the medial lattice of the kagome lattice as shown in the left most panel in Figure. 5.2. On the sites of this medial lattice, we define the Ising variables $v^z = \pm 1$ and on its links we define the Ising gauge fields $\rho^z = \pm 1$. The mapping from the $\sigma$ to the $v$ and $\rho$ variables is defined as follows,

$$v_J^x = \prod_{\triangle} \sigma_a^x \sigma_b^x \sigma_c^x \ ; \ \ \sigma_a^z = v_I^z \rho_{IJ}^z v_J^z \ . \tag{5.10}$$

Clearly, with the insight of (5.6), in the above mapping the $v_I^z$s are nothing but the visons (with conjugate momenta given by $v_I^x$). Since they carry Ising magnetic charge, they couple to the dual Ising gauge potential, $\rho_{IJ}^z$ and transform under a projective representation (that forms the PSG) of the symmetries of the underlying spin Hamiltonian. We note that the product of the dual gauge fields around the hexagonal plaquette is given by

$$\prod_{\hexagon} \rho_{IJ}^z = \prod_{\hexagon} \sigma_a^z = \pm 1 \ , \tag{5.11}$$

where the first product is over each honeycomb hexagon and the second one is on each kagome hexagon.

Though not directly relevant to this work, we would like to point out that the presence of the dual magnetic flux, is nothing but the Ising electric charges (*spinons*):

$$\prod_{\hexagon} \rho_{IJ}^z = \prod_{\hexagon} \sigma_a^z = -1 \ , \tag{5.12}$$

which sit at the center of the hexagonal plaquettes. In terms of the original bosons, these represent hexagons where the constraint of having two bosons is violated (see Figure. 5.2). Evidently, such "defect hexagons", are created in pairs and are energetically very costly in the strong-coupling limit. It is clear from the above equation that the visons see the spinons as a source of $\pi$-flux and hence the dual gauge potential naturally captures the mutual semionic statistics between the visons and the spinons [Bale 02]. Now note that at 1/3 filling, we have two bosons per hexagon. Hence, we must have

$$\prod_{\hexagon} \rho_{IJ}^z = \prod_{\hexagon} \sigma_a^z = 1 \ . \tag{5.13}$$

This just means that there are no spinons at low energies because they are too costly. Hence, on circling the plaquettes of the medial honeycomb lattice, the "flux" seen by the $v^z$-spins

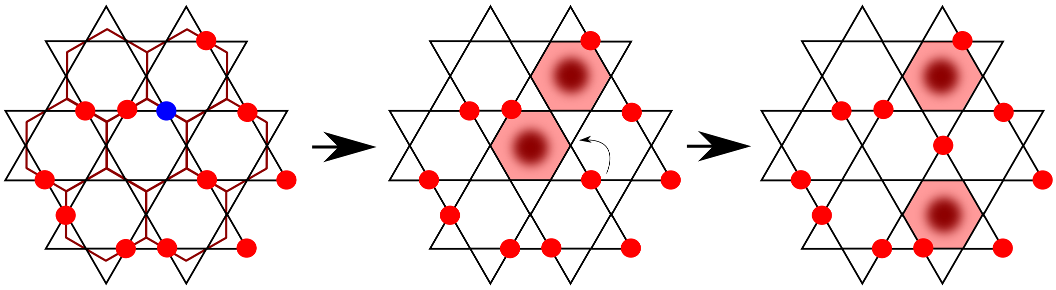

Figure 5.2: The medial honeycomb lattice is shown along with the original kagome lattice. Removal of the blue-colored boson creates two spinon excitations sitting at the centers of the adjacent shaded hexagons (the “defect hexagons") which violate the constraint of having two bosons. By virtue of the single-particle hopping term, these two defects can separate farther apart; however their creation is energetically suppressed in the strong-coupling limit.

is zero. This type of Ising gauge theory (IGT) is called an even IGT as opposed to the odd IGT that arises in the case of $1/6$ or $1/2$ filling when the $v^z$-spins sees a $\pi$-flux in each honeycomb plaquette.

With the mapping in (5.10) the Hamiltonian in (5.9) becomes (we put $u_{\rm eff} = 0$ for the moment)

$$\mathcal{H}_{\rm dual} = -g_{\rm eff}\sum_I v_I^x + V_{\rm eff}\sum_{\hexagon}\left(\frac{1}{2}\sum_{\langle I,J\rangle\in\hexagon} v_I^z\rho_{IJ}^z v_J^z + h\right)^2, \tag{5.14}$$

expanding which we get,

$$\mathcal{H}_{\rm dual} = -g_{\rm eff}\sum_I v_I^x + hV_{\rm eff}\sum_{\langle I,J\rangle} v_I^z\rho_{IJ}^z v_J^z + \frac{V_{\rm eff}}{2}\left[\sum_{\langle\langle II'\rangle\rangle} v_I^z\rho_{II'}^z v_{I'}^z + \sum_{I,J,I',J'\in\hexagon} v_I^z\rho_{IJ}^z v_J^z v_{I'}^z\rho_{I'J'}^z v_{J'}^z\right] \tag{5.15}$$

up to a constant. Until now we have ignored the potential term in the RK Hamiltonian. This term, in the spin language, has the form

$$V_{\rm RK}\sum_\alpha O_\alpha \tag{5.16}$$

where $\alpha$ refers to all bow-ties and has the typical form, for the bow-tie in Figure. 5.3(a), of

$$O_\alpha = \frac{1}{8}\left[-\sigma_1^z\sigma_2^z - \sigma_3^z\sigma_4^z - \sigma_1^z\sigma_4^z - \sigma_2^z\sigma_3^z + \sigma_1^z\sigma_3^z + \sigma_2^z\sigma_4^z - \sigma_1^z\sigma_2^z\sigma_3^z\sigma_4^z\right]. \tag{5.17}$$

This, under the mapping to the $v_I$ variables, augments the second neighbor as well as the four-spin terms along with providing the interactions between four spins, two each on adjacent hexagons. As remarked earlier, the $v^z$ fields transform under a PSG and in general a third neighbor Ising term for the $v_I^z$ fields would also be allowed by the PSG of an even-IGT. These term, would arise, for instance, on integrating out the four spin interactions which would also renormalize the nearest and the second neighbor interactions. In addition, a Maxwell term for the $\rho^z_{IJ}$ fields of the form $\prod_{\bigcirc} \rho^z_{IJ}$ is also allowed and these terms renormalize the energy of the spinons, but due to the constraint in (5.11), such terms are trivial and hence left out. Now, Because of the constraints in (5.11) (i.e., no spinons), it is possible to choose a gauge where

$$\rho^z_{IJ} = +1, \quad \forall I, J \; . \tag{5.18}$$

Hence the general form of the model is given by

$$\mathcal{H}_{\text{dual}} = J_1 \sum_{\text{n.n}} v^z_I v^z_J + J_2 \sum_{\text{n.n.n}} v^z_I v^z_J + J_3 \sum_{\text{n.n.n.n}} v^z_I v^z_J - \Gamma \sum_J v^x_I \; . \tag{5.19}$$

Thus, the minimal gauge theory for the FPL model is dual to the ferromagnetic transverse field Ising model on the honeycomb lattice with first, second and third neighbor Ising interactions.

In the large $\Gamma$ limit we can neglect the $J$ terms and the $v$-spins are polarized in the $x$ direction with the finite vison gap $\sim 2\Gamma$. The underlying $\sigma^z$ spins are thus fluctuating allowing for the boson number per site to fluctuate. This paramagnetic phase is nothing but the $\mathbb{Z}_2$ liquid in the dual description.

On increasing the Ising couplings ($J_{1,2,3}$), the visons gain dispersion and if the minima of the dispersion touches zero, they can condense leading to $\langle v^z_I \rangle \neq 0$. The nature of the ordering depends on the relative signs and magnitude of the Ising couplings and the phase diagram in the limit of large $J_{1,2,3}/\Gamma$ is shown in Figure. 5.3(d). Setting $J_2/J_1 = t_1$ and $J_3/J_1 = t_2$ and $\Gamma/J_1 = \tilde{\Gamma}$ with $J_1 = 1$, in (5.19), the soft vison modes [Blan 84b, Blan 84a] can be obtained from the Fourier transform of the Ising terms. This is given by

$$\mathcal{H}_{\text{dual}} = \sum_k J(k) \Psi^\dagger_k \Psi_k \; , \tag{5.20}$$

where $J(k)$ is the Fourier transform of the adjacency matrix of the Ising terms in (5.19):

$$J(k) = \begin{pmatrix} 2t_1\delta & \gamma + t_2\eta \\ \gamma^* + t_2\eta^* & 2t_1\delta \end{pmatrix} \tag{5.21}$$

and $\Psi_k = (v^x_{1k} \;\; v^x_{2k})^T$ and $\Psi^\dagger_k = (v^x_{1-k} \;\; v^x_{2-k})$. The momentum dependence of the parameters goes as

$$\begin{aligned} \delta &= \cos k_1 + \cos k_2 + \cos(k_1 + k_2) \\ \gamma &= 1 + e^{ik_1} + e^{-ik_2} \\ \eta &= 2\cos(k_1 + k_2) + e^{i(k_1 - k_2)} \; , \end{aligned} \tag{5.22}$$

where $k_i = \vec{k} \cdot \vec{s}_i$ with $\vec{s}_1 = (\sqrt{3}/2, -3/2)$ and $\vec{s}_2 = (\sqrt{3}/2, 3/2)$ being the basis vectors of the honeycomb lattice shown in Figure. 5.3(c). For an extended range of positive $t_1$ and $t_2$, as highlighted by the yellow region in Figure. 5.3(d), the minima of the energy dispersion $J(k)$ occur at the three inequivalent $M$ points – $M_1$, $M_2$ and $M_3$ in the Brillouin zone [see Figure. 5.3(b)] whose coordinates are $(\pi/\sqrt{3}, -\pi/3)$, $(\pi/\sqrt{3}, \pi/3)$ and $(0, 2\pi/3)$

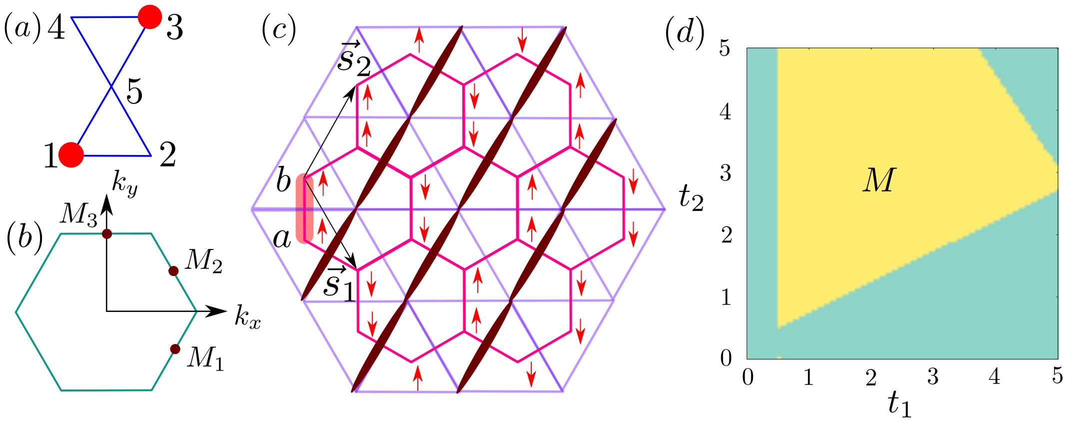

Figure 5.3: (a) A flippable bow tie. (b) The first Brillouin zone of the honeycomb lattice showing $M$ points. (c) Loop ordering at $M_1$ point. A loop segment is placed on the link of the triangular lattice whenever it crosses a honeycomb bond joining antiparallel spins which represent the vison degrees of freedom. (d) The yellow region qualitatively shows the allowed ranges of $t_1$ and $t_2$ for which the minima of $J(k)$ lie in the vicinity of the $M$ points within an energy window of $10^{-3}$. The vertical phase boundary indicates to the case when the minima are exactly on the $M$ points corresponding to the LN phase for $V_{\text{RK}} \ll 0$.

respectively. This extended region of the phase diagram, where the ordering occurs at the $M$ points of the Brillouin zone of the medial honeycomb lattice, yields to a $v_I^z$ ordering pattern which is shown in Figure. 5.3(c). Translating back [using (5.10) and $n_i = (1+\sigma_i^z)/2$], this gives rise to the ordering pattern for $V_{\text{RK}} \ll 0$. There are three such patterns (for the three $M$ points) which corresponds to the three LN phases related by the $C_3$ symmetry as obtained from our previous numerical calculations.

While it is not possible to calculate the values of the Ising couplings in terms of the couplings of the underlying RK Hamiltonian in (4.7), we observe that, the effective model allows phases that are observed in the microscopic model together with the possibilities of a direct continuous quantum phase transition from the $\mathbb{Z}_2$ liquid to the LN phase. Since the symmetries of the actual QDM and the effective gauge theories are identical, we expect that the transition, which is attributed to the condensation of the visons, in each model belongs to the same universality class. We now attempt to find the structure of the critical theory which can predict the nature of this transition.

## 5.5 Continuous transition between the $\mathbb{Z}_2$ liquid and LN and the critical theory

Approaching the transition point from the liquid side [$\Gamma > J$ in (5.19)], we can write down the critical theory in terms of the vison modes that go soft at the transition. These soft modes can be written as [Huh 11]

$$\Psi(\vec{r}) = \sum_{j=1}^{3} \psi_j(\vec{r})\mathbf{v}_j e^{i\vec{M}_j\cdot\vec{r}} , \tag{5.23}$$

where $\psi_j$ are the amplitudes of the three soft modes occurring at the three $M$ points of the Brillouin zone. To construct the Landau-Ginzburg action in terms of the soft modes we need to figure out the transformation of $\psi_j$ ($j = 1,2,3$) among themselves under various symmetries of the Hamiltonian. These are: (1) $\mathbb{T}_1$: lattice translation along $\vec{s}_1$, (2) $\mathbb{T}_2$: lattice translation along $\vec{s}_2$, (3) $\mathbb{I}$: bond inversion or parity, (4) $\mathbb{C}_6$: rotation of $\pi/3$ about the center of a plaquette, and (5) global $\mathbb{Z}_2$ symmetry under which $v^x \to -v^x$. On a point of specific coordinates $\{x,y\}$, the actions of the above symmetries are the following:

$$\begin{aligned}
\mathbb{T}_1 &: \{x,y;a,b\} \to \{x+1,y;a,b\} \\
\mathbb{T}_2 &: \{x,y;a,b\} \to \{x,y+1;a,b\} \\
\mathbb{I} &: \{x,y;a,b\} \to \{-x,-y;b,a\} \\
\mathbb{C}_6 &: \begin{cases} \{x,y;a\} \to \{x-y+1,x;b\}, \\ \{x,y;b\} \to \{x-y,x;a\}. \end{cases}
\end{aligned} \tag{5.24}$$

The transformation matrices of the three critical modes corresponding to different lattice symmetry operations and the global $\mathbb{Z}_2$ are as follows:

$$\begin{aligned}
&\mathcal{R}_{\mathbb{T}_1} = \begin{bmatrix} -1 & 0 & 0 \\ 0 & 1 & 0 \\ 0 & 0 & -1 \end{bmatrix} ; \; \mathcal{R}_{\mathbb{T}_2} = \begin{bmatrix} 1 & 0 & 0 \\ 0 & -1 & 0 \\ 0 & 0 & -1 \end{bmatrix} ; \\
&\mathcal{R}_{\mathbb{I}} = \begin{bmatrix} 1 & 0 & 0 \\ 0 & 1 & 0 \\ 0 & 0 & -1 \end{bmatrix} ; \quad \mathcal{R}_{\mathbb{C}_6} = \begin{bmatrix} 0 & 0 & -1 \\ 1 & 0 & 0 \\ 0 & 1 & 0 \end{bmatrix} ; \\
&\mathcal{R}_{\mathbb{Z}_2} = \begin{bmatrix} -1 & 0 & 0 \\ 0 & -1 & 0 \\ 0 & 0 & -1 \end{bmatrix} .
\end{aligned} \tag{5.25}$$

These five matrices generate a 24-element finite subgroup of $O(3)$ which is isomorphic to $C_2 \otimes A_4$ [The ]. Respecting all the above projective symmetry transformations, the most general Landau-Ginzburg (LG) functional in (2 + 1)-dimensional Euclidean space-time assumes the following form,

$$\mathcal{S} = \int d^2\mathbf{r} d\tau \, \mathcal{L} , \tag{5.26}$$

where the Lagrangian density (up to 6th order) is given by

$$\mathcal{L} = \nabla\vec{\psi}\cdot\nabla\vec{\psi} + \partial_\tau\vec{\psi}\cdot\partial_\tau\vec{\psi} + r\vec{\psi}\cdot\vec{\psi} + \tilde{u}(\vec{\psi}\cdot\vec{\psi})^2 + \tilde{v}(\vec{\psi}\cdot\vec{\psi})^3 + a(\psi_1^4 + \psi_2^4 + \vec{\psi}_3^4) + b(\psi_1\psi_2\psi_3)^2 \tag{5.27}$$

with $\psi = (\psi_1, \psi_2, \psi_3)^T$. If $a = b = 0$, (5.27) represents the usual soft spin $O(3)$ action (or the $N = 3$ linear $\sigma$ model). The $a$ term introduces cubic anisotropy in the system.

Evidently, for $a < 0$, the ordering occurs at one of the soft modes preferentially; i.e., the functional is minimized when one of the components (among $\psi_1$, $\psi_2$, and $\psi_3$) takes a finite value while other two remain zero. Three such possibilities give rise to three symmetry-oriented loop orderings. For example, the order at $M_1$, which corresponds to $\psi_1 \neq 0$ and $\psi_2 = \psi_3 = 0$, can be read from the structure of the full eigenvector $\mathbf{v}_1 = (1, 1)^T$ of $J(k)$ in (5.21) set to the momentum $M_1 = (\pi/\sqrt{3}, -\pi/3)$. The resultant $v^z$-spin configuration is shown in Figure. 5.3(c) and the loop covering of the dimers can be obtained using (5.10) which is equivalent to replacing the antiferromagnetic bonds of the honeycomb lattice by a loop segment on the underlying triangular lattice. This gives back the loop ordering which does not break any translation symmetry (because $M_1$ and $-M_1$ are identical and related by the momentum space lattice vectors) but spontaneously breaks the rotational symmetry. Similarly the ordering at other $M$ points are related to the present one by the spontaneously broken $C_3$ symmetry. This way the critical theory captures the ordering patterns obtained in the numerical calculations of the microscopic model.

For $b = 0$, leading order $\epsilon = 4 - d$ expansion suggests that the cubic anisotropy is irrelevant and the critical point is of $O(3)$ Wilson-Fisher type [Ahar 73, Ketl 73, Brez 74] (however, higher order expansion suggests that it may belong to the cubic critical point with critical exponents very close to the $O(3)$ class [Klei 95]). The 6-th order anisotropy term (denoted by $b \neq 0$) is also irrelevant at such a point along with the $O(3)$ invariant 6th order term, $\tilde{v}$ in (5.27). These considerations suggest that the phase transition between the $\mathbb{Z}_2$ liquid and the LN phase, as seen in the microscopic model, may belong to the $O(3)$ universality class and the anisotropy terms are dangerously irrelevant at this critical point.

It is important to note that the critical theory is not written in terms of the order parameter of the LN phase, as the conventional theory of phase transition would suggest [Land 80, Ma 00]. Instead, it is naturally written in terms of vison fields and the order parameter is bilinear in terms of such vison fields. Hence we should expect large anomalous dimensions in the scaling dimension of the LN order parameter [Sand 07, Isak 12]. Such large anomalous dimensions are characteristics of these types of unconventional phase transitions.

# Chapter 6

# Spin-Charge Interplay in a Frustrated Fermionic Model

The quantum dimer model (QDM) and its several other variants are intimately related to different particle models on frustrated lattices at commensurate fractional fillings because of many striking similarities observed in their low-energy phase diagrams. For example, we have already learned from chapter 2 that spinless fermionic models on a kagome lattice at $1/3$ and $2/3$ filling can be mapped to a QDM on the honeycomb lattice having similar kinetic term in the low-energy effective Hamiltonian. If spin-$1/2$ fermions are considered instead at filling factor $1/3$, the resultant dimer model becomes a two-color fully packed loop model where an important and interesting question arises about the interplay between the spin and charge degrees of freedom. In this chapter we study the effects of such interplay on a kagome lattice and observe that spin fluctuations in the model can actually drive the system through a phase transition into a charge ordered phase. The approach starts systematically from an extended Hubbard model for which we first derive an effective low-energy Hamiltonian using degenerate perturbation theory. By considering different limiting cases, we then obtain some insight into the different phases of the model. In the limit where antiferromagnetic spin fluctuations dominate, a “short loop” phase is formed in which the charges align around hexagons. On the other hand, if the charge fluctuations dominate, we find a “plaquette ordered” ground state. For the latter limit (no spin fluctuations), we find a very peculiar conservation law, namely, the Hamiltonian conserves the magnetization on dynamic sublattices. To get a picture of the whole phase diagram, we perform a large scale exact diagonalization study of clusters up to $N = 36$ sites in which we calculate the energy spectrum and different correlation functions from which help us conclude about the phase diagram.

## 6.1 Model Hamiltonian

We take up the extended Hubbard model on the kagome lattice with on-site and nearest-neighbor repulsive interactions, $U$ and $V$, respectively, with a Hamiltonian

$$\mathcal{H} = -t \sum_{\langle i,j\rangle,\sigma} \left( c^{\dagger}_{i\sigma} c_{j\sigma} + \text{H.c.} \right) + V \sum_{\langle i,j\rangle} n_i n_j + U \sum_{i} n_{i\uparrow} n_{i\downarrow}. \tag{6.1}$$

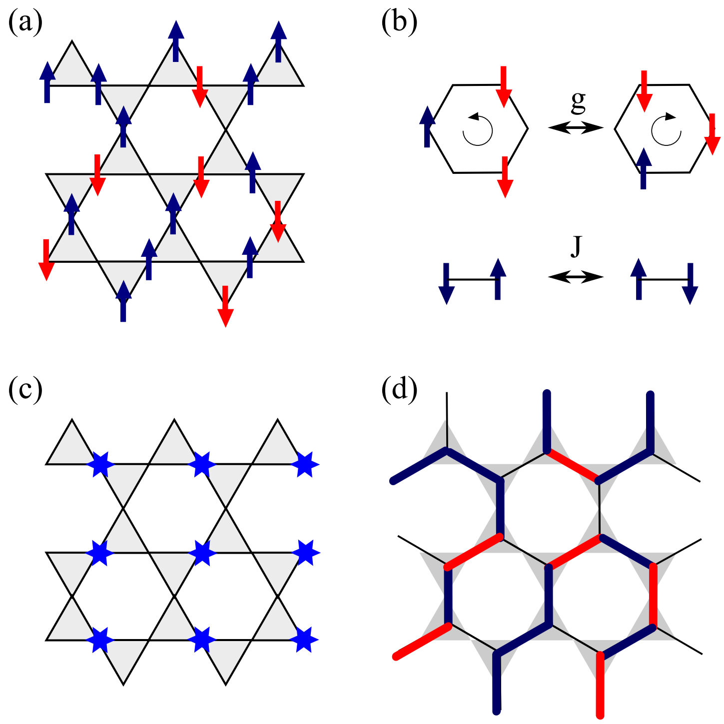

Figure 6.1: (a) A configuration satisfying the constraint of zero or one electron per site and two electrons of arbitrary spin per triangle. (b) Quantum fluctuations allow tunneling between different degenerate configurations of spins and charges: ring exchange with amplitude $g$ and spin exchange with amplitude $J$. The ring exchange processes change the number of electrons on the starred (blue) sublattice shown in panel (c) always by two. This is crucial for gauging away the sign of $g$ explained in the text. (d) All allowed configurations can be expressed in terms of a two-color fully packed loop model on the honeycomb lattice; as an example, we show a representation of the configuration presented in (a).

The operators $c_{i\sigma}$ ($c^{\dagger}_{i\sigma}$) annihilate (create) an electron with spin $\sigma$ on site $i$, $n_i = n_{i\uparrow} + n_{i\downarrow}$ is the electron number operator with $n_{i\sigma} = c^{\dagger}_{i\sigma}c_{i\sigma}$, and the notation $\langle i, j\rangle$ refers to pairs of nearest-neighbors. Throughout this chapter, we focus on the case of $1/3$ filling, in the strongly correlated regime, where $|t| \ll V < U$. At this filling there are two electrons on each triangle on average (i.e., the total number of electrons is $N_e = 2N/3$, where $N$ is the number of lattice sites).

In the strong-coupling limit, when the hopping amplitudes are set to zero and $0 < V < U$, the energy is minimized if there are *exactly* two electrons in each triangle of the kagome lattice with no double occupancy – this is analogous to the case of magnetite as discussed in Ref. [Ande 56]. An example configuration fulfilling these constraints is shown in Figure. 6.1(a). The number of such configurations is macroscopically degenerate: in addition to the trivial $2^{2N/3}$ spin degeneracy, the number of charge configurations also grows exponentially with the system size. The ground state configurations on the kagome lattice can be mapped to two-color fully packed loop configurations on the honeycomb lattice. Particles are sitting here on the links of the honeycomb lattice, and the two different colors encode the spin orientations [see Figure. 6.1(d)]. The charge degrees of freedom (i.e, neglecting the color) can be equivalently described by a dimer model of the honeycomb lattice by simply replacing empty bonds by occupied ones and occupied by empty ones. Using this mapping, the degeneracy of different charge configurations can be calculated exactly using Pfaffians [Fish 63], and is given as $\sim 1.1137^N$ for a honeycomb lattice with $N$ bonds (corresponding to $N$ kagome sites). The total degeneracy is then the product of the spin degeneracy and the charge degeneracy, i.e., $\sim 2^{2N/3} \times 1.1137^N$.

This macroscopic ground-state degeneracy is lifted when quantum fluctuations are taken into account. The effective Hamiltonian that connects a manifold of degenerate states can be obtained from a perturbative expansion of the Hamiltonian (6.1) in $t/V$ and $t/(U-V)$. By keeping only the lowest order of non-vanishing terms, one obtains the effective Hamiltonian as a sum of two parts:

$$\mathcal{H}_{\text{eff}} = \mathcal{H}_{\text{ring}} + \mathcal{H}_{\text{spin}}. \tag{6.2}$$

The first term describes a ring exchange of three electrons occupying every other site on a hexagon of the kagome lattice, and is given as

$$\mathcal{H}_{\text{ring}} = -g \sum_{\{\hexagon\}} h_{\hexagon} \tag{6.3}$$

with an effective ring-exchange amplitude $g = 6t^3/V^2$ and

$$h_{\hexagon} = \sum_{\{\sigma,\sigma',\sigma''\}} \left( c^\dagger_{n\sigma''} c_{m\sigma''} c^\dagger_{l\sigma'} c_{k\sigma'} c^\dagger_{j\sigma} c_{i\sigma} + \text{H.c.} \right). \tag{6.4}$$

The sum in (6.3) is performed over all kagome hexagons and that in (6.4) is over all spin orientations in a given hexagon. The indices $i, j, k, l, m, n$ are sites oriented clockwise on a hexagon yielding the dynamics sketched in Figure. 6.1(b), i.e., three electrons hopping collectively either clockwise or counter-clockwise around the hexagons. Clearly, this ring exchange process preserves the number of electrons on each triangle, and if applied to a state that belongs to the ground state manifold, the resulting state will also be a member of the same manifold. Notice that the fermionic sign in expression for $\mathcal{H}_{\text{ring}}$ can be gauged away, yielding a bosonic model [OBri 10]. Furthermore, the overall sign of $g$ can be transformed by a simple gauge transformation which multiplies all configurations with the factor $i^{N_{\text{star}}}$, where $N_{\text{star}}$ is the number of electrons on the sublattice shown in Figure. 6.1(c).

The second term in the effective Hamiltonian (6.2) is the nearest-neighbor Heisenberg exchange

$$\mathcal{H}_{\text{spin}} = J \sum_{\langle i,j \rangle} \left( 2S_i S_j + \frac{1}{2} n_i n_j \right), \tag{6.5}$$

where

$$J = \frac{2t^2}{U-V} + \frac{2t^3}{V^2}. \tag{6.6}$$

In the ground state manifold, each electron has two occupied neighboring sites (one on each of the two corner sharing triangles), so that closed loops are formed in a system with periodic boundary conditions. These loops are like spin chains and the exchange Hamiltonian $\mathcal{H}_{\text{spin}}$ acts on the spins of the electrons in these closed loops without modifying the charge configuration. The length of the loops is always even, and the shortest loop length is six. For $U \gg V$ the first term in (6.6), proportional to $t^2$, becomes small compared to the term that is $\propto t^3$, so that the sign of the exchange depends on the sign of the hopping amplitude $t$, allowing antiferromagnetic as well as ferromagnetic exchanges (analogous to the one-dimensional case considered in Ref. [Penc 96]). One important aspect of effective model in (6.2) is that $g$ and $J$ can be regarded as nearly independent variables: one can tune the value of $J$ by changing $U$, without affecting $g$. We can reparametrize them by a single variable

$$\alpha = \frac{|g|}{|g| + |J|} , \tag{6.7}$$

which falls within $0 \leq \alpha \leq 1$. In the limiting case $\alpha \to 0$ we can neglect the effect of the ring exchange term. This happens when $V \to U$ (but still $V < U$), as due to the divergence in (6.6), the effective exchange becomes much larger than $g$. In the limit of $V \ll U$, $\alpha \to 3/4$ since

$$\alpha = \frac{3}{4} - \frac{3V^2}{16tU} + O(1/U^2) . \tag{6.8}$$

However, the overall behavior is not so simple and in the following, we consider the different signs of the hopping ($t$) separately: Figure. 6.2 shows the contour plot of $\alpha$ on the $U$-$V$ plane (more precisely, $t/U$ and $t/V$) for $t > 0$ and $t < 0$, respectively. For $t > 0$, the exchange is always antiferromagnetic and $0 < \alpha \leq 3/4$. To increase the $\alpha$ from $\alpha = 0$ limit at $U = V$, we need to increase $U$ compared to $V$, and from (6.8) we find the upper bound as $3/4$.

The situation is more involved when $t < 0$: we encounter both ferromagnetic and antiferromagnetic $J$, and $\alpha$ can take the values $0 < \alpha \leq 1$. The line $\alpha = 1$ in Figure. 6.2(b) is determined by the antiferromagnetic $\propto t^2$ term, canceling the ferromagnetic $\propto t^3$ term in $J$ [see (6.6)]. When the effective exchange is ferromagnetic, the values of $\alpha$ are limited to $3/4 \leq \alpha < 1$: as $U$ increases from the $\alpha = 1$ line, $\alpha$ decreases down to $3/4$ for $U \gg V$ as per (6.8). The antiferromagnetic exchange is realized by decreasing $U$ from the $\alpha = 1$ line toward $U = V$, which decreases $\alpha$ down to zero. These factors indicate that, by a suitable choice of the values of the interactions and hoppings, we can select antiferromagnetic exchange with arbitrary value of $0 < \alpha < 1$. To this end, let us mention that we can link our model to the *flat band ferromagnetism*: the Hubbard model with $t > 0$ and $n \leq 1/3$ has been proven to be ferromagnetic for any $U > 0$ and $V = 0$ [Miel 92, Miel 93]. Furthermore, the $n = 1/3$ case with $|t| \ll V \ll U$ is also proven to exhibit a ferromagnetic ground state [Poll 08] – thus here we extend the possibility of a ferromagnetic ground state also to filling factor $n = 1/3$.

In the remainder of the chapter, we will consider how the effective Hamiltonian lifts the degeneracy of the ground state manifold in the strong-coupling limit.

## 6.2 Limiting cases

It is instructive to first consider the two terms in the effective Hamiltonian (6.2) separately. This corresponds to the setting $\alpha = 1$ and $\alpha = 0$. Understanding these two limits will help

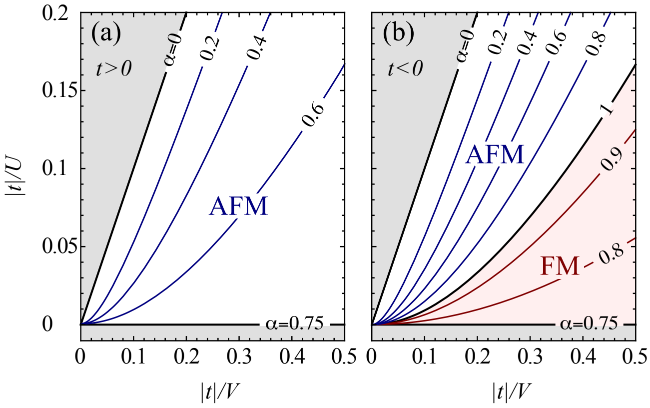

Figure 6.2: The values of the parameter $\alpha$ defined in (6.7) set the contour plots on the plane of $|t|/U$ and $|t|/V$. (a) For $t > 0$ the exchange is always antiferromagnetic, (b) while for $t < 0$ the exchange becomes ferromagnetic (red region) for large on-site repulsion $U$, as it follows from the perturbative expansion up to third order in the hopping, (6.6). The effective Hamiltonian describes the region close to the origin in the unshaded region $U > V$ and $U > 0$. The grey-shaded region denotes the case of $U < V$.

us get a picture of the full phase diagram.

### 6.2.1 Plaquette phase

At $\alpha = 1$, the effective Hamiltonian reduces to $\mathcal{H}_{\text{ring}}$ given by (6.3). We first use the mapping to the two-color fully packed loop model [see Figure. 6.1(d)] to understand the charge dynamics. Second, we discuss a hidden symmetry of this model that yields large degeneracies.

#### Resonating plaquettes and winding numbers

When the spins of the electrons are all pointing in the same direction (e.g. up, $S = S^z = S_{\text{tot}}^{\text{max}}$), the spins can be omitted and the relevant degrees of freedom are the positions of the charges. As described in Sec. 6.1, the charge problem can be mapped to a dimer model on the honeycomb lattice. The QDM on the honeycomb lattice with resonances on the neighboring disjunct hexagons has been shown to have a gapped, plaquette ordered ground state with an off–diagonal order parameter [Moes 01b] – the so-called *plaquette phase* discussed in chapter 2. The ground state is threefold degenerate in the thermodynamic limit, breaking the translation symmetry of the lattice. The plaquette phase, when mapped back to the kagome lattice model, hosts electrons resonating around the hexagons (see Figure. 6.8). Then, one can define conserved quantities (winding numbers) that can be used to classify the states in the Hilbert space, similar to the QDM on a square lattice [Rokh 88]. In our case, $\mathcal{H}_{\text{ring}}$ conserves the number of electrons along the straight lines parallel to the edges of the hexagons in the kagome lattice. Actually, the number of linearly independent winding numbers is only two when the system is put onto a torus (i.e., when considering standard periodic boundary conditions). The Hilbert space is divided into subspaces (sectors), as

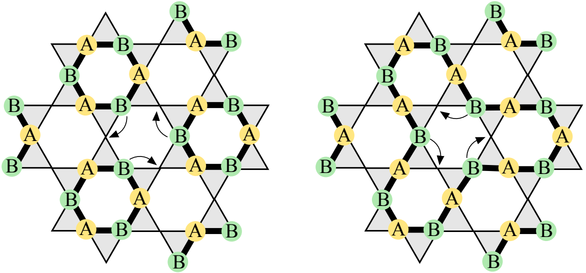

Figure 6.3: Dynamic sublattice structure defined on a loop of charges, consisting of even number of sites. The effective ring exchange denoted by arrows preserves the magnetization on each of the dynamic sublattices $A$ and $B$ (see Appendix C.1 for details).

only states having the same winding numbers are connected by $\mathcal{H}_{\text{ring}}$.

### Hidden conservation law

In what follows, we investigate the effect of the ring exchange on the spins of electrons in the loops. We will show that, in addition to the trivial conservation of total $z$-component $S^z_{\text{tot}}$ and the total spin $S_{\text{tot}}$, a *hidden conservation law* emerges which we describe below.

Let us introduce the *"dynamic two-sublattices"* which are defined on top of the electron loops (Figure. 6.3): starting from an arbitrary choice of loop configuration of electrons, we assign the bipartite labels, $A$ and $B$, to each electron in the loop – this is possible because loops consist of even number sites. To be more precise, the rules to construct the dynamic sublattice are simple: (i) neighboring electrons have different sublattice labels and (ii) next-nearest-neighbor electrons have the same sublattice label on each loop on the kagome lattice. For example, we find hexagon configurations which are completely filled ($ABABAB$ as we go around the hexagon), or depleted hexagons such as $AOAOAO$, $ABAOAO$, and $ABABAO$ (here the $O$ denotes empty sites). Once we have the configuration which fulfills (i) and (ii), the effective Hamiltonian $\mathcal{H}_{\text{ring}}$ obeys this rule: After operating $\mathcal{H}_{\text{ring}}$ arbitrary times, one finds that the bipartite configuration is perfectly kept – each electron can be assigned not only the spin, but also the label denoting the dynamic sublattice. The proof of this conjecture is given in Appendix C.1. Here, notice that even if we come back to the same charge configuration at some point, the sites that were occupied by $A$ electrons could all be replaced to $B$ and vise versa. In fact, even though the bipartite sublattice rule is kept in the loops, the absolute location of $A$ and $B$ are not fixed, which is the reason why we call them "dynamic".

Next, we assign the spins to the electrons in the loops. Since the electrons in the $A$ and $B$ sublattices never exchange with each other, the total $S^z_A$ and $S^z_B$ on each of the dynamic sublattices is a conserved quantity, hence, a good quantum number. This is not only true for the $z$ component, but also for the $\mathbf{S}_A$ and $\mathbf{S}_B$. As a consequence, the Hilbert subspaces of a fixed winding number are further divided into sectors that do not mix the spin $S^z$ on the two sublattices. For a system with the magnetization $S_{max} - n$ we find $\lfloor n/2 + 1 \rfloor$ disconnected sectors, e.g., if we take $S_{max} - 2$, namely flipping two spins from a fully spin polarized configuration, we can either flip both spins on one of the dynamic sublattices or one on

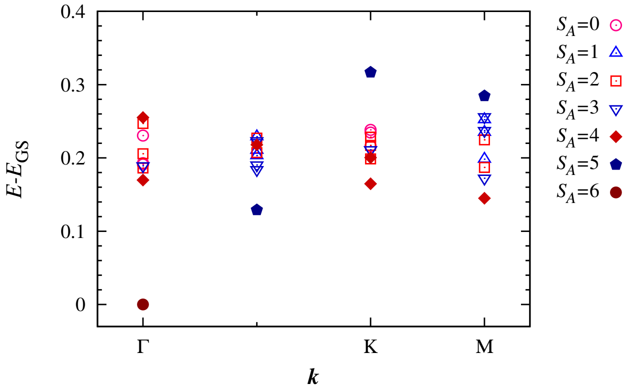

Figure 6.4: Energy spectrum of the $N = 36$ cluster at $\alpha = 1$. We set one of the two dynamic sublattices to be fully polarized as $S_B = 6$, while varying the spin $S_A$ of the other sublattice. The ground state is realized at Γ-point for $S_A = 6$, indicating that both dynamic sublattices hold maximal spins.

each yielding two disjoint sectors. In fact, by keeping $S^z_{\text{tot}} = S^z_A + S^z_B$ fixed, the number $\lfloor n/2 + 1 \rfloor$ is equal to the number of ways one can add two integers.

The hidden conservation law yields a spin degeneracy. To show this, we introduce the $P_{AB}$ operator that exchanges the $A$ and $B$ sublattice labels of the electron operators (note that this operator does not change the charge configuration). Since $P^2_{AB} = 1$, the wave functions are either even or odd with respect to $P_{AB}$, with eigenvalues $\pm 1$. The ring exchange Hamiltonian and the $\mathbf{S}_A + \mathbf{S}_B$ commute with the $P_{AB}$, while the $\mathbf{S}_A - \mathbf{S}_B$ does not. However, we can define the operator,

$$Q^{\mu\nu} = (S^\mu_A - S^\mu_B)(S^\nu_A - S^\nu_B) \tag{6.9}$$

which commutes both with $P_{AB}$ and $\mathcal{H}_{\text{ring}}$ (where $\mu, \nu = x, y, z$). The $Q^{\mu\nu}$ has non-vanishing matrix elements between total spin states that differ by 2, so these states are also degenerate in energy (more precisely, the $Q^{\mu\nu} + Q^{\nu\mu} - (2/3)\delta_{\mu\nu}Q^{\eta\eta}$ is a rank two tensor operator). For example, applying the $Q^{--}$ to the highest weight state of the maximal spin we create a state that is a linear superposition of the $S^{\text{max}}_{\text{tot}}$ and $S^{\text{max}}_{\text{tot}} - 2$, and is degenerate with the $S^{\text{max}}$. Regarding the ground state, we find that the total spin on $A$ and $B$ dynamic sublattices is maximal, $S_A = S_B = N/6$. This could be observed explicitly for the $N = 36$ site cluster shown in Figure. 6.4: There, we keep one of the two sublattices polarized as $S_B = 6$, and vary the total spin of the other sublattice ($S_A$). We find that the ground state does in fact have a maximal $S_A$. The two "giant" spins can be combined to make $S^{\text{max}}_{\text{tot}} - 2m$ spin states that are even with respect to $P_{AB}$, all having the same minimal energy (here $m$ is an integer). Similarly, the $S^{\text{max}}_{\text{tot}} - 2m - 1$ spin states are also degenerate, and are odd eigenstates of $P_{AB}$. In other words, in the ground state the two giant spins on the two dynamic sublattices behave as noninteracting spins (except for the parity effect with respect to $P_{AB}$ that disappears in the thermodynamic limit). To this end, a qualitative difference between the one–third and the one–sixth filled case becomes clear. In the one–sixth filled case ($n = 1/3$), the effective Hamiltonian $\mathcal{H}_{\text{ring}}$ connects all spin configurations

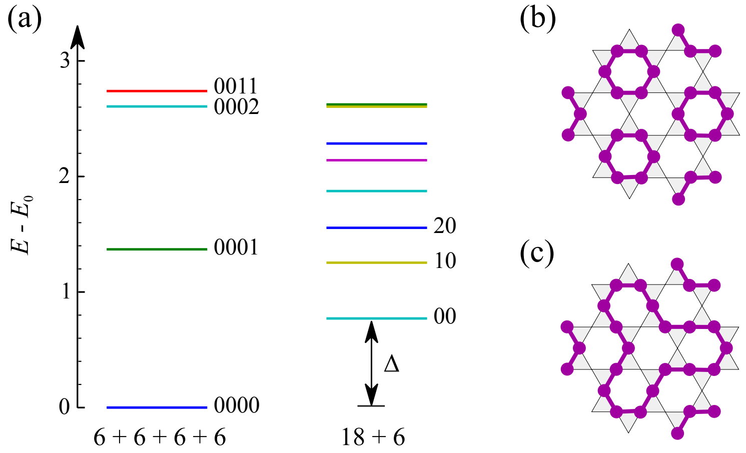

Figure 6.5: (a) Excitation energies of the spin Hamiltonian ($\mathcal{H}_{\text{spin}}$) for two different loop configurations of the 36-site cluster: one consisting of four short-loops of length-six, and the other consisting of one 18-site loop and one six-site loop. The numbers next to the levels indicate in which state each loop is, e.g., 0001 means that three loops are in a ground state and one of them is in the first excited spin state.

within the zero winding sector yielding a ferromagnetic ground state [Poll 08][1].

This is no longer the case for the one–third filled case: the ground state is degenerate, and the ferromagnetic state as well as the singlet state are among the ground states. However, the dynamic sublattices $A$ and $B$ are still ferromagnetic: our system can be thought of putting together two one–sixth filled systems, each of them living on the $A$ and the $B$ dynamic sublattices of the ground state manifold.

### 6.2.2 Short loop phase

At $\alpha = 0$, the effective Hamiltonian is reduced solely to $\mathcal{H}_{\text{spin}}$. Since the fluctuations of electron occupation vanish, the ground state is the one which minimizes the spin exchange interactions along the closed electron loops. This is achieved with short hexagonal loops giving rise to a *short loop phase*, shown in Figure. 6.8. The finite size correction for the ground state energy per site of a periodic antiferromagnetic Heisenberg chain of length $L$ is [Woyn 87]

$$e_L - e_\infty = -\frac{\pi^2}{12L^2} \tag{6.10}$$

in a leading order in $1/L$, where $e_\infty = 1/4 - \ln 2 \approx -0.4431$ is the energy density in the thermodynamic limit. Thus, the shorter the loop is, the lower the energy density becomes. The shortest loop on the kagome lattice is of length $L = 6$ with energy density $e_6 \sim -0.4343$, and these loops are arranged in a regular pattern, as shown in Figure. 6.5(b), with a hexagonal unit cell consisting of 9 sites. A variational estimate of $e_6$ and the corresponding

---

[1] This can be traced back to the number of fermions taking part in the effective ring exchange: for odd number of fermions high spin is favored, while for even number of electrons a low spin state (singlet) is lower in energy, as, e.g., in Ref. [Poil 07] for a quarter filled checkerboard lattice.

ground state wave function using a valence bond approach [Faze 99] is provided in Appendix C.3. This ground state is threefold degenerate and breaks the translation symmetry. The lowest energy excitation of this charge ordered phase is realized by the formation of a $L = 18$ loop out of three adjacent hexagonal loops [Figure. 6.5(c)] with an energy gap of $\Delta = E_{18} - 3E_6 = 0.771$. In Figure. 6.5(a) the energies of different charge (or loop) configurations on a 36-site cluster are shown.

## 6.3 Numerical results

We have already found that the two extreme cases of $\alpha = 0$ and $\alpha = 1$ show different orderings. The transition between the two phases can be understood by using the analogy to the QDM on the honeycomb lattice[2]. As discussed in detail in Ref. [Moes 01b], the two different orderings have centers of rotational symmetry that lie in distinct places when forming domains of one phase with the other (in fact, the precise nature of the phase transition might be either a first order one, or two phase transitions with coexisting order parameters, as suggested in Ref. [Ralk 08] for the QDM on a square lattice). Thus we expect a phase transition between them when tuning the parameter $\alpha$ from 0 to 1.

In order to pin down the transition point and to verify the above mentioned two characteristic phases, we employ numerical exact diagonalization on the effective Hamiltonian $\mathcal{H}_{\text{eff}}$ on finite clusters of sites $N = 27$ and 36. We simulate $\mathcal{H}_{\text{eff}}$ within the Hilbert space spanned by the allowed configurations. Furthermore, we reduce the Hilbert space size by making use of the spatial symmetries given in Appendix C.2. The results are summarized in Figure. 6.8 which shows the phase diagram we obtain from our numerical analysis: we observe a first order phase transition from a "short loop" to a "plaquette ordered" phase at $\alpha \approx 0.6$. Both phases have a charge gap but only the former has a spin gap. The details of the numerical simulations are described below.

However, before presenting our numerical findings, we shall mention that the strong-coupling limit of the Hubbard model (more precisely $t-J$ model) at the same filling as ours, but without the nearest-neighbor $V$ term has been discussed in Ref. [Inde 06]. It has been found that the ground state is formed by a resonance of two electrons in the singlet state on disjunct triangles, making a crystal. The ground state is twofold degenerate, depending if the resonances are taking place on the up or down pointing triangles. The crucial difference with respect to our model is that the number of electrons in the triangle is not restricted to be precisely two, but only on average. In fact, the electron number strongly fluctuates in the triangles connecting the resonating pairs which costs energy due to the $V$ term and leads to destabilization of the state. The Hubbard model for the one-third filling case has been studied in Ref. [Wen 10] using a Hartree-Fock mean field theory which provides a rich phases diagram: our short loop phase can be recognized as the CDWIII phase in their work, while our plaquette phase is missing as the quantum fluctuations stabilizing the resonance of charges are beyond the reach of the Hartree-Fock approach.

---

[2] Even though the effective Hamiltonian in (6.2) is more complex than the quantum dimer model, they both have the same symmetry properties with respect to the charge degrees of freedom. The short-loop phase can be mapped to the columnar phase and plaquette phases can be identified in both the models.

### 6.3.1 Anderson tower

As for the case of $\alpha = 1$, we have seen that the conservation of the spin on the $A$ and $B$ dynamic sublattice leads to a degenerate ground state manifold. The spins on the two dynamic sublattices take the maximal value $S_A = S_B = N/6$, and as they do not interact, the states spanned by the two "giant" spins constitute the ground state manifold (Figure. 6.4 reveals that states with lower sublattice spin $S_A$ and $S_B$ are higher in energy). Once the $\mathcal{H}_{\text{spin}}$ is turned on, the hidden conservation law does not hold any longer, and the spins on the $A$ and $B$ sublattice start to interact with each other:

$$\mathcal{H}_{\text{LM}} \propto \frac{J}{N} \mathbf{S}_A \cdot \mathbf{S}_B \ , \tag{6.11}$$

similar to a Lieb-Mattis model [Lieb 62], as the kinetic term $g \gg J$ decouples the wave function and each spin on the $A$ sublattice interacts with each spin on the $B$ sublattice with an effective coupling $\propto J/N$. Denoting by $S_{\text{tot}}$ the total spin of the system, the energy of this Hamiltonian is simply described as,

$$\mathcal{E}_{\text{LM}} \propto \frac{J}{N} \left[ S_{\text{tot}}(S_{\text{tot}} + 1) - S_A(S_A + 1) - S_B(S_B + 1) \right] \ . \tag{6.12}$$

Indeed, the degeneracies at $\alpha = 1$ are quickly removed when decreasing $\alpha$ (see Figure. 6.7). When plotted against $S_{\text{tot}}(S_{\text{tot}} + 1)$, the spectrum shows low-energy states whose energy is $\propto J/N S_{\text{tot}}(S_{\text{tot}} + 1)$, as shown in Figure. 6.6. These states form the Anderson tower, which is the clear signature of an antiferromagnetic ordering [Bern 92]. In this case, the texture of the antiferromagnetic order is quite peculiar, as schematically shown in right part of Figure. 6.8: a large effective spin-3/2 of resonating charges on a hexagon is surrounded by "localized" spin-1/2 electrons. The resonating plaquette can occupy either of the three inequivalent hexagon sublattices, thus the state is threefold degenerate regarding the space group symmetries. This is reflected in the irreducible content of the states in the Anderson tower in Figure. 6.6; IR1 and IR5 for the 36 site cluster (see Appendix C.2 for the whole chart of the irreducible representation). With increasing system size, the slope of the lowest energy levels approaches zero as $1/N$ and become degenerate in the thermodynamic limit. The finite size gap of the states above the Anderson tower also goes to zero — in the case of antiferromagnetic ordering we expect that the scaling follows $1/\sqrt{N}$, which, however, could not be checked in our problem due to rapidly growing dimension of the Hilbert space. The spin excitation spectrum becomes gapless, in contrast to the short loop phase when $\alpha \approx 0$.

### 6.3.2 Energy spectrum

We now consider the ground state and lowest excited states over the full range $\alpha \in [0, 1]$. Figure. 6.7 shows the energy spectra as a function of $\alpha$ for the $N = 27$ and 36 site clusters. At $\alpha = 0$, the excitation gap above the threefold degenerate ground state corresponds exactly to the value of $\Delta$ obtained by diagonalizing the Heisenberg chains in section 6.2.2. Due to finite size effects, the threefold degeneracy of the ground state is lifted immediately for any $\alpha > 0$. A level crossing in the lowest excitations is prominent near $\alpha = 0.6$ for both the clusters, indicating that the system undergoes a first order quantum phase transition at $\alpha \approx 0.6$ [Sach 07, Zamf 02, Aria 03].

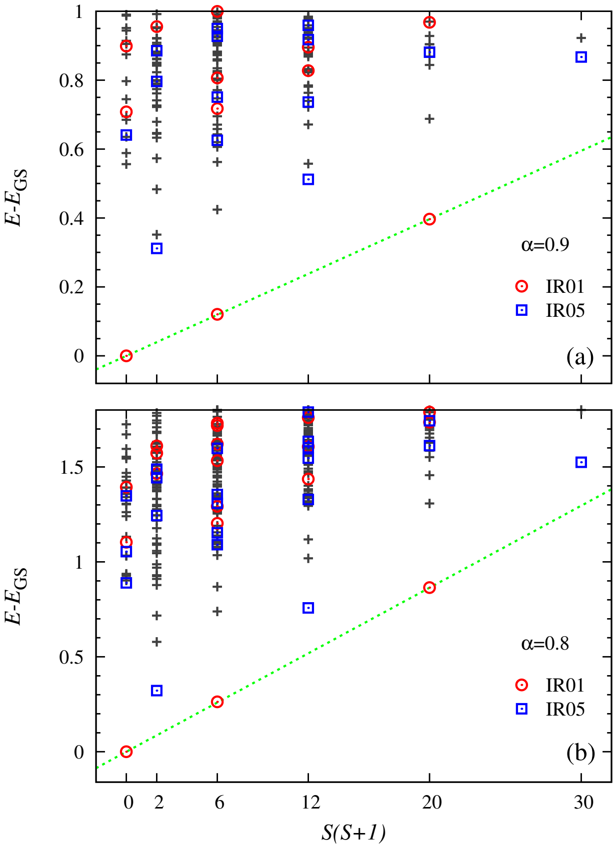

Figure 6.6: Anderson tower for the $N = 36$ cluster for (a) $\alpha = 0.9$ and (b) $\alpha = 0.8$. The energies of the low lying two series of states belonging to different irreducible representations, IR01 and IR05 (see AppendixC.2), which are even and odd with respect to $P_{AB}$, behave proportional to $S(S + 1)$. As $\alpha$ increases and/or the system size increases, their gradient decreases toward zero, at which all these points fall onto the same horizontal line (become degenerate). Such behavior is the strong indication of the antiferromagnetic ordering.

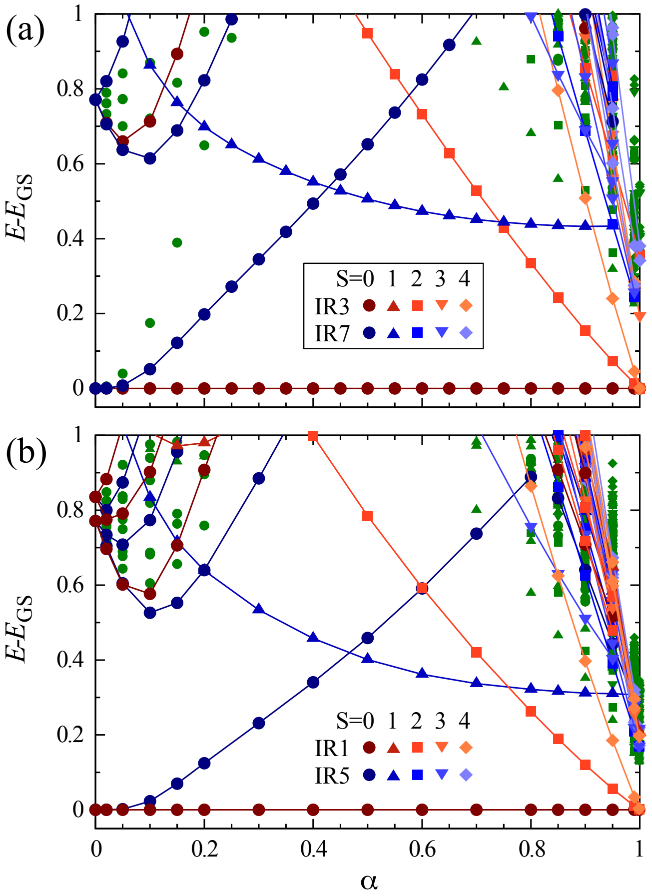

Figure 6.7: Energy spectra for two different clusters $N = 27$ and 36. The level crossing occurs at $\alpha_c \approx 0.6$ between the energy levels of the same quantum number for both the clusters, which indicates the possible quantum phase transition. All the energies are measured from the lowest energy singlet state.

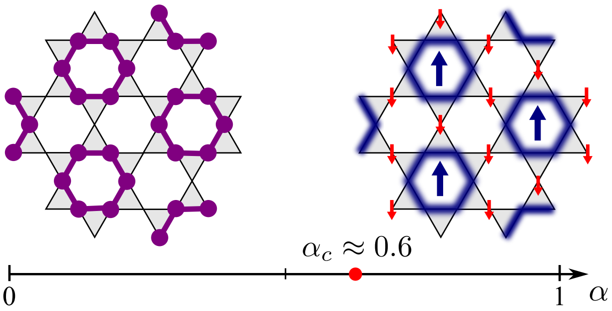

Figure 6.8: Ground state phase diagram of (6.2). With increasing $\alpha$, the short-loop phase undergoes the first order quantum phase transition into the plaquette phase at around $\alpha \sim 0.6$. The solid hexagons on the upper left panel denote the short loops formed by the neighboring electrons, and the blurred hexagons on the upper right panel indicate the presence of the resonating plaquettes.

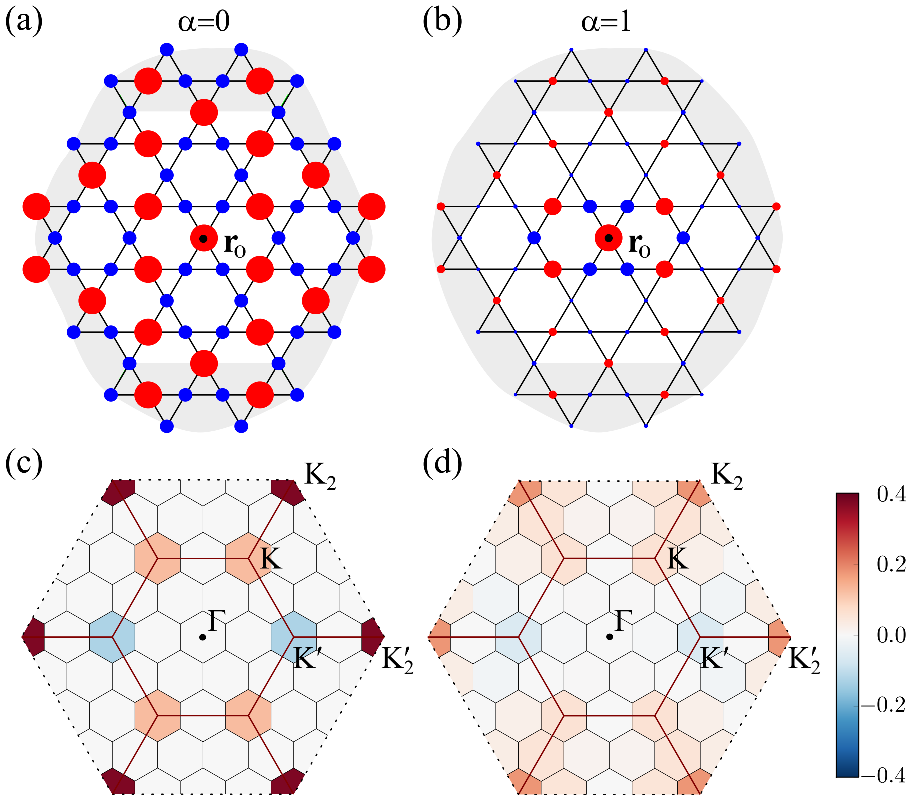

Figure 6.9: Panels (a) and (b) show the charge-charge correlation function in real space for $\alpha = 0$ and 1, respectively. The correlations are calculated with respect to the marked site $\mathbf{r_0}$ at the center. The radius of the dots is proportional to the absolute value of the correlation, while the color encodes the sign (red/blue corresponds to positive/negative value). Panels (c) and (d) display the same data in momentum space in the extended Brillouin zone. The maxima in panel (c) is found at $\mathbf{Q} = (8\pi/3, 0)$ and symmetry related points (high symmetry points denoted by $K_2$ and $K_2'$).

Combining the findings of the previous sections and the exact diagonalization data in Fig 6.7, we reach the phase diagram shown in Figure. 6.8. Two phases are separated by a first order phase transition. For $\alpha \approx 0.6$ we find the "short loop phase", representing a charge ordered phase that has both a charge and a spin gap.

### 6.3.3 Correlation functions and structure factors

We calculate several different kinds of correlation functions for the $N = 36$ cluster which serve as characteristic fingerprints of the phases. We begin by studying the charge-charge correlation functions,

$$C^c(\mathbf{r}_0, \mathbf{r}_j) = \langle n(\mathbf{r}_0) n(\mathbf{r}_j) \rangle - \langle n(\mathbf{r}_0) \rangle \langle n(\mathbf{r}_j) \rangle, \tag{6.13}$$

where $\mathbf{r}_0$ and $\mathbf{r}_j$ are the positions of charges on the kagome lattice and the expectation values are taken with respect to the ground state. The $n(\mathbf{r}_j)$ is the occupation number operator which measures whether a charge is present at $\mathbf{r}_j$ regardless of its spin orientation. Figure. 6.9(a) shows the density plot of $C^c(\mathbf{r}_0,\mathbf{r}_j)$ at $\alpha = 0$, which describes the charge order of the "short loop phase". The charges on the hexagons, which form short loops, are perfectly correlated. With increasing $\alpha$, this order gradually melts toward $\alpha = 1$ at which only the short-range correlations remain as shown in Figure. 6.9(b). The corresponding structure factor,

$$S^c(\mathbf{q}) = \frac{1}{N}\sum_j e^{-i\mathbf{q}\cdot(\mathbf{r}_j-\mathbf{r}_0)}\, C^c(\mathbf{r}_0,\mathbf{r}_j) \tag{6.14}$$

is calculated in the extended Brillouin zone and shown in Figure. 6.9. Note that we do not average the structure factor over the entire unit cell but instead calculate it for a specific center. Thus we have both positive and negative contributions. In experiments, one would observe the averaged structure factor. The ordering wave vectors $\mathbf{Q}$ of the "short loop phase" lie at the corners ($K_2$ and $K_2'$) of the extended Brillouin zone where the sharp peaks are observed.

Next we consider the plaquette-plaquette correlation function

$$C^h(\mathbf{R}_0,\mathbf{R}_j) = \langle h_{\bigcirc}(\mathbf{R}_0)h_{\bigcirc}(\mathbf{R}_j)\rangle - \langle h_{\bigcirc}(\mathbf{R}_0)\rangle\langle h_{\bigcirc}(\mathbf{R}_j)\rangle, \tag{6.15}$$

where the operators $h_{\bigcirc}(\mathbf{R}_0)$ and $h_{\bigcirc}(\mathbf{R}_j)$ are those representing the resonance, as defined in (6.4) on the hexagons centered at positions $\mathbf{R}_0$ and $\mathbf{R}_j$, respectively. The centers of these hexagons form a triangular lattice. At $\alpha = 0$, $C^h(\mathbf{R}_0,\mathbf{R}_j)$ vanishes except for $\mathbf{R}_0 = \mathbf{R}_j$, as shown in Figure. 6.10(a). This is because the charges are perfectly localized on short loops, and thus, cannot resonate. By contrast, we find a clear sign of the plaquette ordering at $\alpha = 1$ in Figure. 6.10(b), whose spacial pattern are exactly the one expected in Figure. 6.8. The structure factor $S^h(\mathbf{Q})$ for both cases is calculated analogously to (6.14) and is displayed over the first Brillouin zone in Figure.. 6.10(c) and 6.10(d). The one at $\alpha = 0$ is structureless, whereas at $\alpha = 1$ we observe sharp peaks at the corners of the first Brillouin zone.

Finally we consider the spin-spin correlation function,

$$C^s(\mathbf{r}_0,\mathbf{r}_j) = \langle \mathbf{S}(\mathbf{r}_0)\mathbf{S}(\mathbf{r}_j)\rangle - \langle \mathbf{S}(\mathbf{r}_0)\rangle\langle \mathbf{S}(\mathbf{r}_j)\rangle, \tag{6.16}$$

where the operator $\mathbf{S}(\mathbf{r}_j)$ is the spin-1/2 spin operator at site $\mathbf{r}_j$. For $\alpha = 0$ the spins living on different short-loops are uncorrelated, and this is clearly seen in $C^s(\mathbf{r}_0,\mathbf{r}_j)$ which vanishes once the distances are $|\mathbf{r}_0 - \mathbf{r}_j| > 2$ [see Figure. 6.11(a) and its corresponding structure factor in Figure. 6.11(c)]. The spin structure becomes more distinct as $\alpha$ goes to 1 [see Figure..6.11(b) and 6.11(d)], and its textures in real and reciprocal spaces follow those of the charge in Figure.. 6.9(b) and 6.9(d). As we discussed earlier, the spins living on two dynamic sublattices form large ferromagnetic spins, $S_A$ and $S_B$, and one will find large correlation between the spins belonging to the same sublattice, if the dynamic sublattice could be extracted. However, in real space, the strong spin fluctuations will cause the mixing of the two dynamic sublattices, and quite a large part of the real space correlations are canceled out.

In Figure. 6.12 we show how the amplitudes of different structure factors at the respective ordering wave vectors (the $\mathbf{Q}$-point which has the largest amplitude of the structure

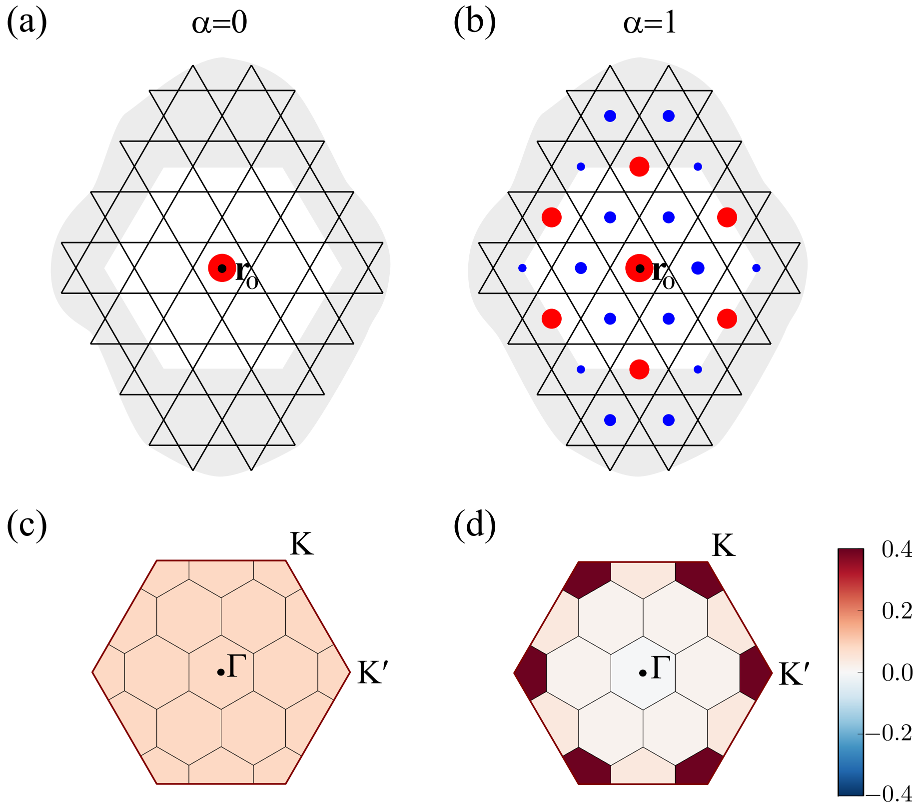

Figure 6.10: Panels (a) and (b) show the plaquette-plaquette correlation function in real space for $\alpha = 0$ and 1, respectively. The correlations are calculated with respect to the marked site $\mathbf{r_0}$ at the center. The radius of the dots is proportional to the absolute value of the correlation while the color encodes the sign (red/blue corresponds to positive/negative value). Panels (c) and (d) show the same data in momentum space in the first Brillouin zone. The peaks in panel (d) are found at $K$ and $K'$ points, with $\mathbf{Q} = (2\pi/3, 2\pi/\sqrt{3})$ and $\mathbf{Q} = (4\pi/3, 0)$, respectively.

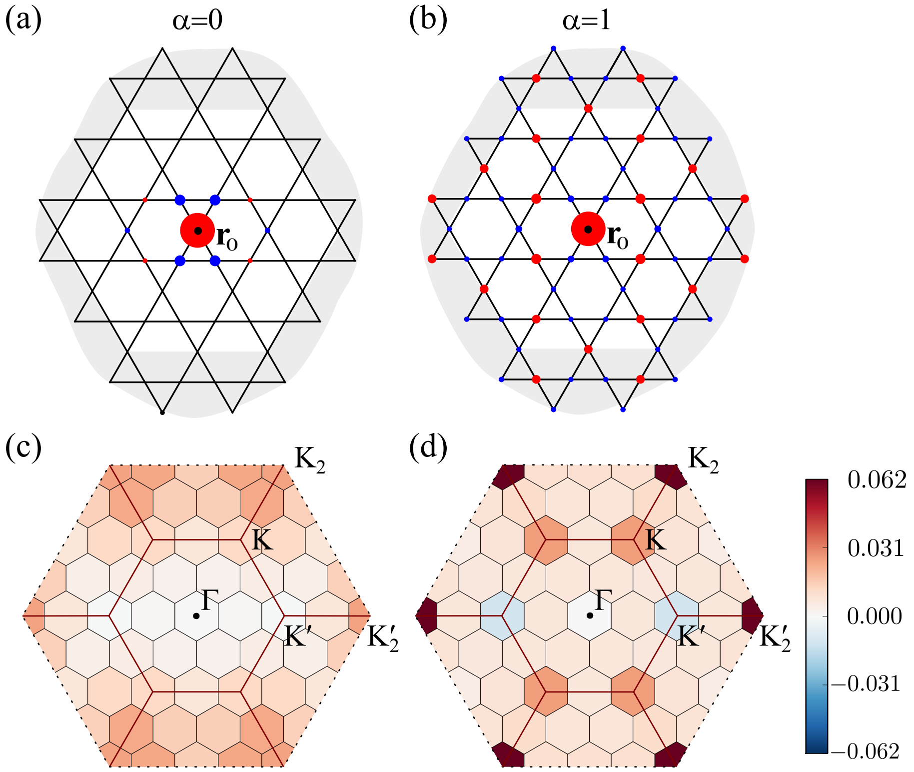

Figure 6.11: Panels (a) and (b) show the spin-spin correlation function in real space for $\alpha = 0$ and 1, respectively. The correlations are calculated with respect to the marked site $\mathbf{r_0}$ at the center. The radius of the dots is proportional to the absolute value of the correlation while the color encodes the sign (red/blue corresponds to positive/negative value). Panels (c) and (d) show the same data in momentum space in the extended Brillouin zone.

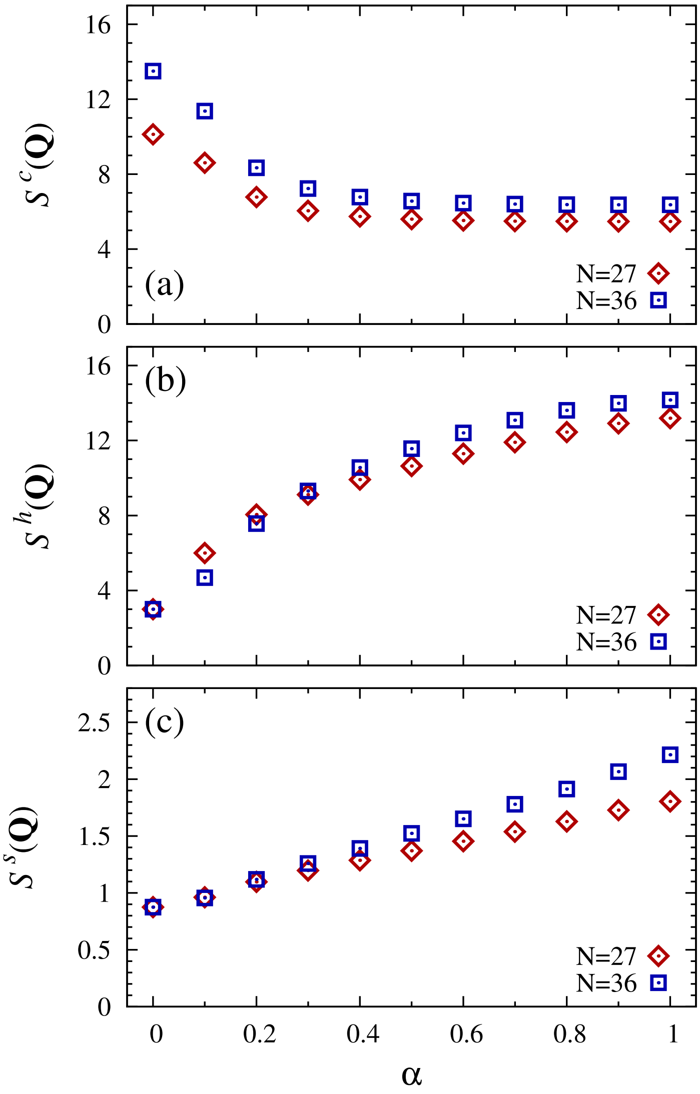

Figure 6.12: Amplitudes of the (a) charge, (b) plaquette, (c) and spin structure factors, shown in Figure..6.9-6.11, at the corresponding ordering wave vectors **Q**. The gradual changes in all three panels indicate the melting of different kinds of ordering as the parameter $\alpha$ is varied.

factors) evolve. Here we multiply the amplitudes by the system size $N$, in order to compare the results of different sizes on the same ground, assuming that the sum rules are fulfilled. While the general tendency is clear, it is difficult to identify the phase transition point between the two phases in the correlation functions, presumably due to finite size effects.

# Chapter 7

# Summary and Outlook

**Summary.** The thesis studies strongly correlated fermionic and bosonic models on a kagome lattice at different fractional fillings aiming to realize novel Mott insulating phases at low temperatures in presence of geometric frustrations. The strong correlation limit implies the neighboring repulsions between the particles to be much stronger than their kinetic energy. This can describe the family of Mott insulators which potentially harbors exotic phases with conventional and topological orders in the ground state. As we see in a fermionic model, stability of the conventionally ordered phases relies on the interplay of spin and charge degrees of freedom of the electrons. On the other hand, certain long-range interactions in some bosonic models on frustrated lattices can pin topological order on the ground state with their low-energy theories being described by a quantum dimer model (QDM) Hamiltonian. In this thesis we considered a generalized version of the QDM, called the quantum fully packed loop (FPL) model, on a triangular lattice which, alongside a topological liquid phase like the standard QDM, also realizes a novel lattice nematic phase under proper tuning of the parameters that appear in the low-energy effective model. Main findings noted in the previous chapters are summarized as follows.

In chapter 3 we start by reviewing the properties of classical dimer models on different lattices which have been of great importance in various branches of physics and studied extensively as and when required. Understanding these classical models has involved several analytical and numerical works till date. A critical disordered phase is observed at high temperatures when the dimer model is considered on a bipartite lattice. The corresponding correlation functions show algebraic decay with spatial distances. The situation is different on non-bipartite lattices as the disordered phase becomes gapped and the correlation functions are exponentially decaying. It is to be noted that the liquid phase in QDM at the Rokhsar-Kivelson (RK) point has similar properties which can be addressed in classical simulation techniques, as it can be described in terms of classical dimers at infinite temperature. In this spirit, we apply a recently developed tensor network based algorithm, called tensor renormalization group (TRG), to probe the behavior of the dimer-dimer correlation functions in the classical dimer models on a square and a triangular lattice. The results are benchmarked against the standard classical Monte Carlo technique and show agreement with the theoretical predictions of Pfaffian method [Fend 02]. It turns out that TRG performs quite efficiently to desired numerical accuracy when applied to a short-ranged gapped system with the correlation functions well reproduced for the triangular lattice dimer model. However, the performance is less impressive for a gapless phase as the convergence slows down due to rapid loss of entanglement within the network. Consequently a huge amount of data storage is required which is the case for the square lattice dimer model.

In chapter 4 we introduce the quantum FPL model on a triangular lattice as a generalization of QDM, and describe it from the standpoint of a microscopic bosonic model governed by an extended Bose-Hubbard Hamiltonian. This Hamiltonian is defined on a kagome lattice at filling fraction $1/3$ and yields a novel Mott insulating state in the strong interaction limit. The low-energy excitations of the model can be effectively described by nonintersecting closed quantum loop coverings on the triangular lattice (on the same footing, the triangular lattice QDM corresponds to the $1/6$ filling of hard-core bosons on the kagome lattice). Using the previously described tensor-network based methods and exact diagonalization techniques, we show that the system (FPL model) has an extended $\mathbb{Z}_2$ topological liquid phase as well as a lattice nematic phase, the latter breaking lattice rotational symmetry. The liquid ground state is protected by a gap to the vison excitations that remains finite even if the RK potential term is absent in the Hamiltonian. This reminds of the case of an easy axis kagome antiferromagnetic model [Bale 02] (EAKAM) which also realizes a topological liquid of same nature and can be derived from a microscopic bosonic model at $1/2$ filling on the kagome lattice.

Low-energy physics of these three bosonic insulators (QDM, FPL model and EAKAM) can be effectively described using a common framework of Ising gauge theory. Depending on the filling fractions, the structure of the theory can be further classified into an odd and an even sector that can distinguish the FPL model from the others in various aspects. For example, a lattice nematic order can be realized for the FPL model which belongs to the even Ising class, while plaquette orderings take place for the other cases that belong to the odd Ising class. We establish the connection to the gauge theory in chapter 5, and performing duality transformations, show that the even Ising gauge theory for the quantum FPL model is dual to a ferromagnetic transverse-field Ising model on a honeycomb lattice. The dual model is further analyzed by means of projective symmetry group approach to study the quantum phase transition (QPT) between the topological liquid phase and the symmetry broken lattice nematic phase. Such a transition is unconventional and cannot be described in terms of the lattice nematic order parameter, instead the dual vison fields. We also construct the critical theory for the QPT which predicts this continuous transition to belong to the $O(3)$ universality class.

The last chapter concerns about a strongly correlated fermionic model at $1/3$ filling on the kagome lattice which has an interesting resemblance to a two-color quantum fully packed loop model on the honeycomb lattice. The dynamics of the electrons is described by an extended Hubbard Hamiltonian with on-site and nearest-neighbor repulsion terms. As a consequence of the commensurate filling and large interactions, each triangle has precisely two electrons in the effective low-energy description, and these electrons form chains of different lengths. The model is endowed with an intriguing phase diagram at low temperatures. The low-energy effective Hamiltonian includes the ring exchanges around the hexagons as well as the nearest-neighbor Heisenberg interactions. Using large scale exact diagonalization, we find that the effective model exhibits two different phases. If the charge fluctuations are small, the magnetic fluctuations confine the charges to short loops around the hexagons, yielding a gapped charge ordered phase. When the charge fluctuations dominate, the system undergoes a quantum phase transition, characterized by a level crossing in the spectrum, to a resonating plaquette phase with ordered spins and gapless spin excitations. We find that a peculiar conservation law is fulfilled — the electrons in the chains can be divided into two sublattices, and this division is conserved by the ring exchange terms.

**Outlook.** The results of this thesis serve as strong motivation for various future works concerning different aspects of bosonic and electronic Mott insulators that are studied here and also have experimental relevance. The kagome lattice structure is of particular importance as some of the recent experimental results on Mo-based cluster magnets such as $\mathrm{LiZn_2Mo_3O_8}$ [Shec 12] are suggestive of the physics to be described by hopping electrons on an anisotropic kagome lattice with nearest-neighbor repulsions at $1/6$ filling of electrons [Chen 14, Chen 15]. In this class of materials, a spin liquid cluster Mott state is likely to exist at low temperatures for which the spinon dispersion has distinct footprints in the magnetic susceptibility measurements featuring two distinct Curie-Weiss regimes. Feasibility studies to realize such state for our one-third filled fermionic case on an anisotropic kagome lattice surely compose an interesting problem for future. The consequences of the spin exchange term in this case is expected to play a crucial role in deciding the fate of the spinon Fermi surface and other low-energy excitations.

The bosonic models also open up quite a few new avenues including the search for novel supersolid phases at incommensurate fillings on the kagome lattice. Quantum Monte Carlo simulations for these models would be helpful to explore the full phase diagram at arbitrary ratios of the hopping to the interactions and also to unfold structural details about the phase transitions between various ordered and disordered phases. Another nice aspect of the FPL model is related to the dynamics of the fractional charge excitations in the lattice nematic phase. We have already learned that doping the insulating state with a single boson would lead to two dispersive fractional excitations whose motions are aided by ring exchange processes of other bosons. On a finite lattice, deconfinement of these excitations can sometimes be energetically favorable giving rise to a novel compressible edge liquid state with broken chiral symmetry [Zhan 13]. It would be interesting to realize such edge liquid phase under the specific bow-tie exchanges of our FPL model and to analyze its stability in the vicinity of the critical point and also inside the topological liquid phase.

Instead of bosons, if the same model is considered with fermions, the resultant quantum dimer models acquire non-trivial statistics which might have drastic effects on the topological liquid state. Interestingly, such kind of fermionic dimer models can arise in context of describing the metallic state of the hole-doped cuprates at low hole densities [Punk 15]. Studying such a fermionic QDM on non-bipartite lattices itself is an interesting open problem. While in the bipartite case, the fermionic sign problem can be gauged away [Poll 11], energy spectrum for a non-bipartite lattice carries striking differences between the fermionic and the bosonic models. Even the ground state degeneracy at the RK point is lifted for the fermionic case on a finite cluster of triangular lattice posing non-trivial hurdles on the investigation of the topological order if at all there. The structure of the ground state wave function in this case is no more an equal weight superposition like the usual QDM. Solving these puzzles certainly demands more understanding regarding the underlying gauge theory and constitutes an interesting direction for further studies in future. All these models are important ingredients analyzing which would significantly enrich the present cognizance on frustrated magnets, more specifically the quantum spin liquids and shed light on many of their unpredicted behaviors.

# Acknowledgments

The thesis has become a reality due to kind support and assistance from many individuals who never ceased to extend help till the work was finished. It is always pleasurable to express my gratitude to all of them.

First of all I am sincerely grateful to Dr. Frank Pollmann for introducing me to the specific fields related to my thesis and thoroughly supervising the work for the entire period of my stay in Max-Planck-Institut für Physik komplexer Systeme. I enjoyed every bit of discussion with him which helped me a lot gain insight into the subject. I am thankful to Prof. Dr. Roderich Moessner for his continuous support for this work and illuminating comments regarding the other projects I am currently involved in. I also owe gratitude to Prof. Dr. Matthias Vojta and Prof. Dr. Kirill Shtengel for kindly agreeing to referee the thesis and offering invaluable suggestions to improve the work.

I want to express my thanks to all my collaborators in various projects, communications with whom were extremely useful and became an integral part of the thesis. In particular, contributions from Prof. Dr. Karlo Penc, Prof. Dr. Chisa Hotta, Dr. Subhro Bhattacharjee and Dr. Ching-Yu Huang are to be especially acknowledged. I am also thankful to all my other collaborators with whom working has always been a privilege and pleasure.

During the work, I have greatly benefitted from the stimulating discussions and insightful comments from Prof. Dr. Christopher Henley, Prof. Dr. Peter Fulde, Prof. Dr. Eugene Mele, Dr. Joseph Betouras, Dr. Sourin Das, Dr. Arnab Das, Dr. Arnab Sen, Dr. Paul McClarty and many others whose names I could not put in such a limited space. Special thanks are due to all my friends in and outside my institute whose help was imperative and the company has always been a blessing to me.

Last, but certainly not the least, I would like to thank my family members for their extended support and encouragement which inspired me in every aspect of my research not only during the time I worked on the thesis but all along the journey.

# Appendix A

# Pfaffian Method

The Pfaffian method aims at calculating the partition function ($Z$) of the dimer models exactly from which other relevant physical quantities such as correlation functions can be derived. In order to construct the Pfaffian, we need to create an antisymmetric matrix $M$, called Kasteleyn matrix, and the partition function can be conveniently expressed as a linear combination of the Pfaffians of four different Kasteleyn matrices $M_{(a,b)}$ where $a, b = 0(1)$ implies periodic (anti-periodic) boundary conditions along the horizontal and vertical directions. The elements of the matrix $M$ are defined to satisfy Kasteleyn's clockwise-odd rule: the number of arrows pointing in the clockwise direction around the faces is always odd. A matrix element $M_{ij}$ is nonzero only if sites $i$ and $j$ are connected by a bond. If $M_{ij} = 1$, the arrow points from $i$ to $j$ and if $M_{ij} = -1$, the arrow points from $j$ to $i$. The number of dimer coverings ( or equivalently the partition function) is given by

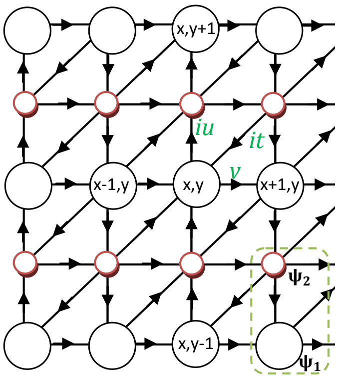

Figure A.1: The square lattice with diagonal bonds and a two-site (black and red circles) unit cell. Also shown are the directions of the Kasteleyn arrows which satisfy the clockwise odd rule described in the text.

$Z = |Pf[M]|$, where $Pf[M]$ is the Pfaffian of matrix $M$ where: $Pf[M] = (\det[M])^{1/2}$. The determinant can be calculated by using Fourier transformation of a fermionic path integral expressed in terms of Grassmann variables.

## A.1 Partition function from the action of Grassmann variables

As pointed in chapter 3, Grassmann variable $\psi_i$ is defined on every lattice site $i$, and the action can be defined as $S = \sum_{i<j} M_{ij}\psi_i\psi_j$. One should take note of the fact that both the square and the triangular lattice geometry can be fitted to a single framework by incorporating diagonal bonds in a square lattice structure with certain fugacity $t \in [0,1]$. On a more general footing, the vertical and horizontal bonds can also also assigned fugacities $u$ and $v$ respectively. Keeping $u = v = 1$, the quantity $t$ smoothly interpolates between a square lattice to a triangular lattice when tuned from 0 to 1. The unit cell, in this case, has to contain two sites, and in the present context it is chosen to be doubled in the vertical direction as shown in Figure. A.1. A unit cell is associated with the position vector $\vec{R}_i$ with an index $\alpha = 1,2$ locating the two sites within the unit cell. The two fermions in the unit cell at $\vec{R}_i$ are denoted as $\psi_{\alpha,\vec{R}_i}$ with $\alpha = 1,2$. The action in terms of the Grassmann variables $\psi$ can be written as

$$S = \frac{1}{2}\sum_{\vec{R}_i,\alpha}\sum_{\vec{R}_j,\beta} M^{\alpha\beta}_{\vec{R}_i\vec{R}_j}\psi_{\alpha,\vec{R}_i}\psi_{\beta,\vec{R}_j} \tag{A.1}$$

with $M^{\alpha\beta}_{\vec{R}_i\vec{R}_j} = -M^{\beta\alpha}_{\vec{R}_j\vec{R}_i}$. Periodic boundary enforces the condition: $M^{\alpha\beta}_{\vec{R}_i\vec{R}_j} = M^{\alpha\beta}(\vec{R}_i - \vec{R}_j)$, and the elements of matrix $M$ multiplied by proper weight are given by

$$M^{12}(0) = M^{21}(\hat{y}) = iu \;\; ; \;\; M^{11}(\hat{x}) = M^{22}(\hat{x}) = v \;\; ; \;\; M^{21}(\hat{x}+\hat{y}) = -M^{12}(\hat{x}) = it. \tag{A.2}$$

Fourier transforming the Grassmann variables by the relation

$$\tilde{\psi}_{\alpha,\vec{k}} = \sum_{\vec{R}_i} e^{i\vec{k}\cdot\vec{R}_i}\psi_{\alpha,\vec{R}_i}, \tag{A.3}$$

the partition function is expressed as $Z = \int [D\psi]\exp(S) = Pf[M]$ with

$$S = \frac{1}{2}\sum_{\vec{k},\alpha,\beta}\tilde{\psi}_{\alpha,\vec{k}}\tilde{M}^{\alpha,\beta}_{\vec{k}}\tilde{\psi}_{\beta,-\vec{k}} \tag{A.4}$$

where $\tilde{M}_{\vec{k}}$ is a $2\times 2$ matrix:

$$\tilde{M}_{\vec{k}} = \begin{pmatrix} 2iv\sin k_x & g(\vec{k}) \\ g^*(\vec{k}) & 2iv\sin k_x \end{pmatrix} \tag{A.5}$$

with $g(\vec{k}) = i[u - te^{ik_x} - ue^{-ik_y} - te^{-i(k_x+k_y)}]$ and $g(\vec{k}) = -g^*(-\vec{k})$. It is straightforward to calculate the partition function which follows from $Z^2 = \det[M]$ where $\det[M] = \prod_{\vec{k}}\det\tilde{M}_{\vec{k}}$ and $\det\tilde{M}_{\vec{k}} = -4v^2\sin^2 k_x - 4u^2\sin^2(k_y/2) - 4t^2\cos^2(k_x + k_y/2)$. Subject to the periodic boundary conditions, the Pfaffians are the square root of the determinants specified by the Kasteleyn matrices of lattice edges with, or without, the reversal of arrows on edges connecting two opposite boundaries. A closer inspection of the Kasteleyn matrices $M(a,b)$ with proper boundary conditions reveals that the boundary Kasteleyn matrices will depend on the boundary conditions (periodic or antiperiodic) with phase factors along the horizontal and vertical direction. These together give rise to a prefactor $\kappa = \pm 1$ in front of $M(a,b)$ while contributing to $Z$. Finally, the number of total dimer coverings is given by [Kast 61]

$$\begin{aligned} Z = \frac{1}{2}( &- Pf[M(0,0)] + Pf[M(0,1)] \\ &+ Pf[M(1,0)] + Pf[M(1,1)]). \end{aligned} \tag{A.6}$$

The magnitude of the wave vectors $\vec{k}$ depends on the boundary conditions $a$ and $b$ of lattice $L_x \times L_y$, such as $k_x = 2\pi(l_x + a/2)/L_x$ and $k_y = 2\pi(l_y + b/2)/L_y$ where $l_x = 0, 1, \ldots, L_x - 1$ and $l_y = 0, 1, \ldots, L_y - 1$.

## A.2 Correlation functions

For any dimer covering of the lattice, the bond is either occupied by a dimer or not, so the number of dimers on each bond can only take the value 0 or 1. Because the unit cell at most contains only one dimer, the probability of finding a dimer on a bond oriented along $\hat{y}$ in a unit cell at $\vec{R}_i$ is given by

$$\mathcal{P}(\vec{R}_i) = |\langle \psi_{1,\vec{R}_i} \psi_{2,\vec{R}_i} \rangle|, \tag{A.7}$$

which is averaged over all positions on the lattice. In a similar way, the dimer-dimer correlation function can also be expressed in terms of the Grassmann variables,

$$D(r) = \langle \psi_{1,\vec{R}_i} \psi_{2,\vec{R}_i} \psi_{1,\vec{R}_j} \psi_{2,\vec{R}_j} \rangle, \tag{A.8}$$

where we consider a case of $\vec{R}_j = \vec{R}_i + r\hat{x}$. Using Wick decomposition it becomes

$$D(r) = \langle \psi_{1,\vec{R}_i} \psi_{2,\vec{R}_i} \rangle \langle \psi_{1,\vec{R}_j} \psi_{2,\vec{R}_j} \rangle - \langle \psi_{1,\vec{R}_i} \psi_{1,\vec{R}_j} \rangle \langle \psi_{2,\vec{R}_i} \psi_{2,\vec{R}_j} \rangle + \langle \psi_{1,\vec{R}_i} \psi_{2,\vec{R}_j} \rangle \langle \psi_{2,\vec{R}_i} \psi_{1,\vec{R}_j} \rangle. \tag{A.9}$$

after which (3.6) applies straightforward. The individual Green function elements can also be read from the matrix $M$ using $G_{ij} \equiv \langle \psi_{\vec{R}_i} \psi_{\vec{R}_j} \rangle = (M^{-1})_{\vec{R}_j \vec{R}_i} = -(M^{-1})_{\vec{R}_i \vec{R}_j}$. By using (A.3), the Green function can be written in the Fourier basis as

$$G_{\alpha,\vec{R}_i;\beta,\vec{R}_j} = \sum_{\vec{k}_i,\vec{k}_j} e^{-i(\vec{k}_i \cdot \vec{R}_i + \vec{k}_j \cdot \vec{R}_j)} \langle \tilde{\psi}_{\alpha,\vec{k}_i} \tilde{\psi}_{\beta,\vec{k}_j} \rangle \tag{A.10}$$

where we know $\langle \tilde{\psi}_{\alpha,\vec{k}_i} \tilde{\psi}_{\beta,\vec{k}_j} \rangle = \delta_{\vec{k}_j,-\vec{k}_i} (\tilde{M}^{-1})^{\alpha,\beta}_{\vec{k}_i}$ from (A.4). Finally, the two-point function can be represented in terms of $g(\vec{k})$ and $\det \tilde{M}_{\vec{k}}$ in the momentum space, namely,

$$\begin{aligned} \langle \tilde{\psi}_{1,\vec{k}} \tilde{\psi}_{1,-\vec{k}} \rangle = \langle \tilde{\psi}_{2,\vec{k}} \tilde{\psi}_{2,-\vec{k}} \rangle &= \frac{2i \sin(k_x)}{\det \tilde{M}_{\vec{k}}} \\ \langle \tilde{\psi}_{1,\vec{k}} \tilde{\psi}_{2,-\vec{k}} \rangle &= -\frac{g^*(\vec{k})}{\det \tilde{M}_{\vec{k}}} \\ \langle \tilde{\psi}_{2,\vec{k}} \tilde{\psi}_{1,-\vec{k}} \rangle &= -\frac{g(\vec{k})}{\det \tilde{M}_{\vec{k}}} \end{aligned} \tag{A.11}$$

By doing a further Fourier transform, we can determine the real space Green function,

$$\langle \psi_{\alpha,\vec{R}_i} \psi_{\beta,\vec{R}_j} \rangle = \int d\vec{k} e^{-i\vec{k}\cdot(\vec{R}_i - \vec{R}_j)} \langle \tilde{\psi}_{\alpha,\vec{k}} \tilde{\psi}_{\beta,-\vec{k}} \rangle \tag{A.12}$$

$$= \int_0^{2\pi} dk_x \int_0^{2\pi} dk_y e^{-i\vec{k}\cdot(\vec{R}_i - \vec{R}_j)} \langle \tilde{\psi}_{\alpha,\vec{k}} \tilde{\psi}_{\beta,-\vec{k}} \rangle \tag{A.13}$$

Numerical integration of the above functions leads to Table. I in chapter 3.

# Appendix B

# Pauling Estimate for Residual Entropy of Dimer Models

Pauling estimate provides the approximate size of the ground state manifold taking into account the local constraints. It is useful for calculating the residual entropy in a frustrated model as we shall see below.

## B.1 Ground state degeneracy for dimer models at different fillings

For classical dimer model on a triangular lattice [Fend 02] the degeneracy can be exactly calculated using the Pfaffian method which is described in Appendix A. However, extending it to the generalized dimer models is quite non-trivial on non-bipartite lattices for which we can make an estimate as given in Table I below. The first column reads the bosonic filling fraction $f$. The second one gives the number of dimer configuration for a given triangular lattice site for that particular filling. Looking at the triangular lattice, with site $N$, it is clear that we can choose the dimer orientation freely at $N/7$ sites (see Figure. B.1 left panel). This gives the lower bound of the ground state entropy per site as shown in the third column of table I and plotted in blue in Figure. B.1 right panel. A slightly better estimate (given in the fourth column and plotted in red in Figure. B.1 right panel) is obtained

| Filling, f | No. of config. for each triangular lat. site, g | Ent. lower bound $S/N = (\log g)/7$ | Pauling estimate | Exact Result |
|---|---|---|---|---|
| 1/6=1 dim. | 6 | 0.25597 | 0.293384 | 0.4286 |
| 1/3=2 dim. | 15 | 0.38686 | 0.532338 | - |
| 1/2=3 dim. | 20 | 0.42796 | 0.61086 | - |
| 2/3=4 dim. | 15 | 0.38686 | 0.532338 | - |
| 5/6=5 dim. | 6 | 0.25597 | 0.293384 | 0.4286 |

Table I: Listed is the residual entropy/site for various dimer fillings on a triangular lattice. The calculation procedure is sketched in the text.

by looking at the nearest-neighbors and satisfying the constraints (Pauling estimate). This works as follows:

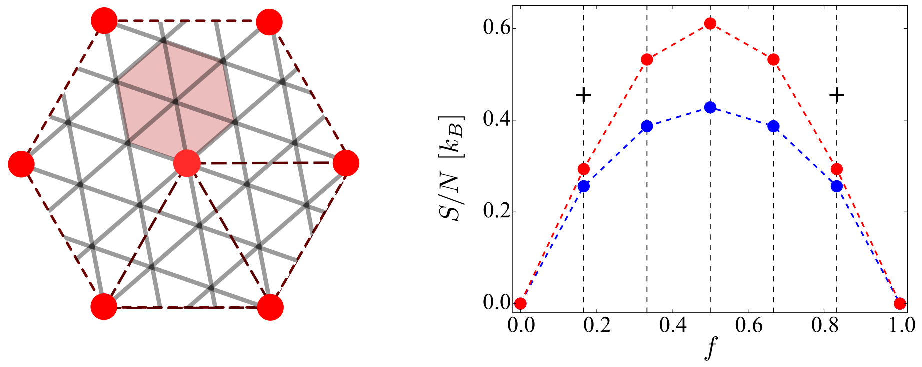

Figure B.1: Left: The red dots denote the chosen $N/7$ for which the dimer orientation can be selected freely. The shaded region denotes the $\sqrt{3} \times \sqrt{3}$ unit cell. Right: The lower bound (blue) and the Pauling estimate (red) for the entropy/site as given in Table I. The '+' marks are for the exact values known only for 1/6 and 5/6 filling [Fend 02].

$1/6$ **and** $5/6$ **filling :** We take the $N/3$ sites sitting on the $\sqrt{3} \times \sqrt{3}$ lattice (shown by the shaded hexagon in Figure. B.1 left panel). Each of them can have six dimer configurations. For these six configurations, the probability that its six neighbors obey the constraint of one dimer per site is given by

$$\frac{1}{6} \cdot \frac{5}{6} \cdot \frac{5}{6} \cdot \frac{5}{6} \cdot \frac{5}{6} \cdot \frac{5}{6} \cdot 6 = \left(\frac{5}{6}\right)^5 \tag{B.1}$$

Therefore the number of configuration is given by

$$\Omega_{1/6} = \left[6 \cdot \left(\frac{5}{6}\right)^5\right]^{N/3} \qquad \Rightarrow \qquad \frac{S}{N} = 0.293384 \tag{B.2}$$

$1/3$ **and** $2/3$ **filling :** Here, each of the $N/3$ sites can assume 15 configurations. For these configurations, the probability that its six nearest-neighbors obey the constraint is

$$\frac{5}{15} \cdot \frac{5}{15} \cdot \frac{10}{15} \cdot \frac{10}{15} \cdot \frac{10}{15} \cdot \frac{10}{15} \cdot 15 \tag{B.3}$$

which gives

$$\Omega_{1/3} = \left[15 \cdot 5 \cdot \frac{2^4}{3^5}\right]^{N/3} \qquad \Rightarrow \qquad \frac{S}{N} = 0.532338 \tag{B.4}$$

$1/2$ **filling :** Here each of the $N/3$ sites have 20 states. The probability for the neighbors to satisfy the constraint is

$$\left(\frac{1}{2}\right)^6 \cdot 20 \tag{B.5}$$

giving

$$\Omega_{1/2} = \left[20^2 \cdot \left(\frac{1}{2}\right)^6\right]^{N/3} \qquad \Rightarrow \qquad \frac{S}{N} = 0.61086 \tag{B.6}$$

The exact value of $S/N$ is known [Fend 02] only for the $1/6$ filled case (and equivalently for the $5/6$ filling) which is given in the last column of Table I and marked '+' in Figure. B.1 right panel.

## B.2 Effective model in connection to the gauge theory

The aim of this section is to derive the effective Hamiltonian in (5.9) given in chapter 5. We start with the labeling scheme of $\mathcal{F}_\triangle = \left(\sigma_1^x \sigma_2^x \sigma_5^x\right)$ and $\mathcal{F}_\triangledown = \left(\sigma_5^x \sigma_3^x \sigma_4^x\right)$, shown in Figure. 5.3(a), to write down the partition function for the Hamiltonian in (5.3) as

$$\mathcal{Z} = Tr\left[e^{-\beta\mathcal{H}_{\text{eff}}}\right] = \sum_{\{\sigma^z\}} \langle\{\sigma^z\}|e^{\beta g \sum_\alpha \mathcal{F}_\triangle^{(\alpha)} \mathcal{F}_\triangledown^{(\alpha)}} \hat{\mathcal{P}}|\{\sigma^z\}\rangle \tag{B.7}$$

where $\hat{\mathcal{P}} = \prod_\alpha \hat{\mathcal{P}}_\alpha$. Using the usual Trotter decomposition, we can write as

$$\mathcal{Z} = \sum_{\{\sigma_1^z\}} \cdots \sum_{\{\sigma_N^z\}} \langle\{\sigma_1^z\}|e^{\Delta\tau g \sum_\alpha \mathcal{F}_\triangle^{(\alpha)} \mathcal{F}_\triangledown^{(\alpha)}} \hat{\mathcal{P}}|\{\sigma_2^z\}\rangle \cdots \langle\{\sigma_N^z\}|e^{\Delta\tau g \sum_\alpha \mathcal{F}_\triangle^{(\alpha)} \mathcal{F}_\triangledown^{(\alpha)}} \hat{\mathcal{P}}|\{\sigma_1^z\}\rangle \tag{B.8}$$

For each slice we can introduce a auxiliary field and use the following identity

$$e^{\frac{(b+c)^2}{2a}} = C \int_{-\infty}^{\infty} dx e^{-\frac{a}{2}x^2 + x(b+c)} \tag{B.9}$$

we get,

$$\begin{aligned}\mathcal{Z} =& C \sum_{\{\sigma_1^z\}} \cdots \sum_{\{\sigma_N^z\}} \int \left[\prod_\alpha dx_1^{(\alpha)}\right] \cdots \int \left[\prod_\alpha dx_N^{(\alpha)}\right] e^{-\frac{1}{2g\Delta\tau} \sum_\alpha \sum_{\tau=1}^N (x_\tau^{(\alpha)})^2} \\ & \langle\{\sigma_1^z\}|e^{\sum_\alpha x_1^{(\alpha)}\left(\mathcal{F}_\triangle^{(\alpha)} + \mathcal{F}_\triangledown^{(\alpha)}\right)} \hat{\mathcal{P}}|\{\sigma_2^z\}\rangle \cdots \langle\{\sigma_N^z\}|e^{\sum_\alpha x_N^{(\alpha)}\left(\mathcal{F}_\triangle^{(\alpha)} + \mathcal{F}_\triangledown^{(\alpha)}\right)} \hat{\mathcal{P}}|\{\sigma_1^z\}\rangle\end{aligned} \tag{B.10}$$

To proceed further we need make the following approximations. We assume that the auxiliary fields fluctuations are small, so that at the zeroth order we can replace them by their non-zero mean values $\bar{x}$ which is independent of time. However this naive approximation is clearly wrong because this would lead then lead to processes that can change the number of bosons per hexagon from the value constrained by $\mathcal{H}_\text{V}$, which is clearly energetically costly. So, we cannot naively assume that the $x$ fields are all constant because their fluctuations impose the above constraint of number of bosons per hexagon. Since the details of their fluctuations probably does not affect the physics of our interest, we shall replace the $x$ fields by their saddle point value and at the same time introduce a projector $\hat{Q}$ which projects to the sector where the constraint, as imposed by $\mathcal{H}_{\mathrm{V}}$, is obeyed. Hence we have:

$$\mathcal{Z} \approx C \sum_{\{\sigma_1^z\}} \cdots \sum_{\{\sigma_N^z\}} \langle\{\sigma_1^z\}| e^{\bar{x}\sum_\alpha \left(\mathcal{F}_\vartriangle^{(\alpha)} + \mathcal{F}_\triangledown^{(\alpha)}\right)} \hat{Q}\hat{\mathcal{P}} |\{\sigma_2^z\}\rangle \cdots \langle\{\sigma_N^z\}| e^{\bar{x}\sum_\alpha \left(\mathcal{F}_\vartriangle^{(\alpha)} + \mathcal{F}_\triangledown^{(\alpha)}\right)} \hat{Q}\hat{\mathcal{P}} |\{\sigma_1^z\}\rangle \tag{B.11}$$

The role of the projectors is now to ensure that the dynamics occur in the low-energy sector where the constraints are obeyed. We can implement the action of this projection softly by using a potential term that energetically penalizes states which deviates from the constraint. In the Hamiltonian Language, this is equivalent to introducing the modified effective Hamiltonian given in (5.9) of chapter 5. Note that the strong-coupling effective Hamiltonian (5.3) and the modified Hamiltonian (5.9) are equivalent in the limit $V_{\mathrm{eff}}/g_{\mathrm{eff}} \to \infty$. This treatment is true for any general commensurate filling of the dimers on the triangular lattice. Nevertheless, we use it for the fully packed loop (FPL) model on the triangular lattice and realize the low-energy effective theory in terms of the emergent vison excitations.

# Appendix C

# Dynamic Sublattice Rule and Valence Bond Approach

In this appendix we first prove that the effective ring-exchange Hamiltonian ($\alpha = 1$) in (6.3) conserves the magnetization on the dynamic sublattices. Then we will provide the irreducible representation table concerning the symmetries of the 36 site kagome cluster which is used for the numerical simulations presented in chapter 6. At the end we will discuss the valence bond approach to find the ground state in the short loop phase.

## C.1 Proof for dynamic sublattice rule

The rules for the "dynamic sublattice" are simple: (i) neighboring electrons have different sublattice labels and (ii) next-nearest-neighbor electrons have the same sublattice label on each hexagon of the kagome lattice (see Figure. 6.3). Once we have the configuration which fulfills (i) and (ii), the effective Hamiltonian $\mathcal{H}_{\text{ring}}$ preserves this rule. A flippable hexagon involves necessarily only loop segments of the same kind which is demanded by (ii). Also the protruding bonds coming out of a flippable hexagon are always exactly of the other kind to which the hexagon is made of. Let us assume without loss of generality an $A$-$A$-$A$ configuration on the flipped hexagon. Then the six protruding bonds will essentially be labeled by $B$. Flipping the loop segments around a hexagon does not change the positions relative to each other and thus (i) and (ii) are fulfilled in the resulting hexagon configuration. Next we have to check the six neighboring hexagons. The three hexagons which loose a loop segment are trivially fulfilling the conditions. For the hexagons which gain a loop segment, we need to argue a little more. The neighboring links of the added segment are necessarily occupied by a $B$ segment since the initial configuration was a valid closely-packed loop configuration and it fulfilled (i). Since the neighboring segments are of the $B$ type, we know that the next-nearest-neighboring segments are of the $A$ type or empty. Thus the resulting configurations fulfills (i) and (ii).

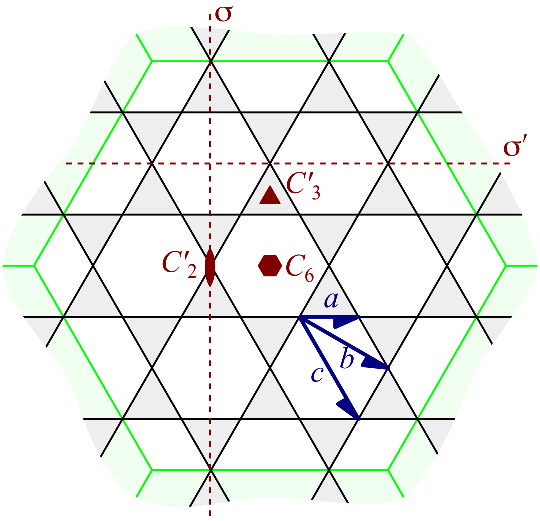

Figure C.1: Description of the $N = 36$ site cluster with periodic boundary conditions. The symmetries of the point group are denoted by dark red: the hexagon denotes the rotation center of order six ($C_6$), the triangle the rotation center of order three ($C'_3$), while the oval the rotation center of order 2 ($C'_2$). Dashed lines are the reflections $\sigma$ and $\sigma'$. Dark blue lines with half arrow denote glide reflections.

## C.2 Irreducible representations of the 36 site cluster

The symmetry group elements of the 36 site cluster with periodic boundary conditions are shown in Fig. C.1 which form the wallpaper group **p6m**, with the point group $\mathcal{D}_6$. The 36 site cluster consists of 12 unit cells, and since the order of the $\mathcal{D}_6$ is 12, the total number of the symmetry group elements is $12 \times 12 = 144$. The character table is as follows:

| IR | $I$ | $6\sigma$ | $18\sigma'$ | $9C'_2$ | $3C_6^3$ | $6T_1$ | $12c$ | $12a$ | $18b$ | $6a^3$ | $3T_1T_2$ | $2T_1^2$ | $24C_6$ | $16C'_3$ | $8C_6^2$ | BZ |
|---|---|---|---|---|---|---|---|---|---|---|---|---|---|---|---|---|
| 1 | 1 | 1 | 1 | 1 | 1 | 1 | 1 | 1 | 1 | 1 | 1 | 1 | 1 | 1 | 1 | Γ |
| 2 | 1 | 1 | −1 | −1 | −1 | 1 | 1 | 1 | −1 | 1 | 1 | 1 | −1 | 1 | 1 | Γ |
| 3 | 1 | −1 | 1 | −1 | −1 | 1 | −1 | −1 | 1 | −1 | 1 | 1 | −1 | 1 | 1 | Γ |
| 4 | 1 | −1 | −1 | 1 | 1 | 1 | −1 | −1 | −1 | −1 | 1 | 1 | 1 | 1 | 1 | Γ |
| 5 | 2 | 2 | 0 | 0 | 0 | −1 | −1 | −1 | 0 | 2 | 2 | −1 | 0 | −1 | 2 | $K$ |
| 6 | 2 | −2 | 0 | 0 | 0 | −1 | 1 | 1 | 0 | −2 | 2 | −1 | 0 | −1 | 2 | $K$ |
| 7 | 2 | 0 | 0 | 2 | 2 | 2 | 0 | 0 | 0 | 0 | 2 | 2 | −1 | −1 | −1 | Γ |
| 8 | 2 | 0 | 0 | −2 | −2 | 2 | 0 | 0 | 0 | 0 | 2 | 2 | 1 | −1 | −1 | Γ |
| 9 | 4 | 0 | 0 | 0 | 0 | −2 | 0 | 0 | 0 | 0 | 4 | −2 | 0 | 1 | −2 | $K$ |
| 10 | 3 | 1 | 1 | −1 | 3 | −1 | 1 | −1 | −1 | −1 | −1 | 3 | 0 | 0 | 0 | $M$ |
| 11 | 3 | 1 | −1 | 1 | −3 | −1 | 1 | −1 | 1 | −1 | −1 | 3 | 0 | 0 | 0 | $M$ |
| 12 | 3 | −1 | 1 | 1 | −3 | −1 | −1 | 1 | −1 | 1 | −1 | 3 | 0 | 0 | 0 | $M$ |
| 13 | 3 | −1 | −1 | −1 | 3 | −1 | −1 | 1 | 1 | 1 | −1 | 3 | 0 | 0 | 0 | $M$ |
| 14 | 6 | 2 | 0 | 0 | 0 | 1 | −1 | 1 | 0 | −2 | −2 | −3 | 0 | 0 | 0 | |
| 15 | 6 | −2 | 0 | 0 | 0 | 1 | 1 | −1 | 0 | 2 | −2 | −3 | 0 | 0 | 0 | |

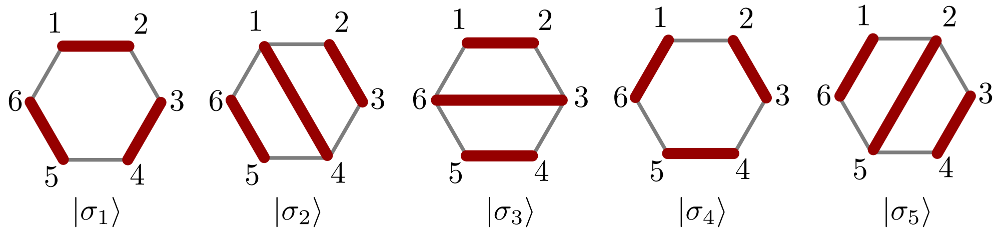

Figure C.2: The basis elements of the singlet space for a periodic six-site AF coupled chain.

where we also specify the point(s) in the Brillouin zone it belongs to.

## C.3 Valence bond approach

The aim is to calculate the ground state energy and the wavefunction of an antiferromagnetically (AF) coupled six-site Heisenberg chain in the variational valence bond approach under periodic boundary condition. A valence bond is the singlet between two spins at lattice sites $i$ and $j$ denoted as $[ij] = \frac{1}{\sqrt{2}}(|\uparrow\rangle_i|\downarrow\rangle_j - |\downarrow\rangle_i|\uparrow\rangle_j)$. The Hamiltonian in (6.5)

$$\mathcal{H}_{\text{spin}} = J\sum_{\langle i,j\rangle}\left(2S_iS_j + \frac{1}{2}n_in_j\right) \equiv J\sum_{\langle i,j\rangle}(1 - Q_{ij}) \tag{C.1}$$

can be written as a sum of operators $Q_{ij}$ which directly act on the singlet bonds with the following effects [Faze 99]

$$Q_{ij}[ij] = 2[ij] \quad \text{and} \quad Q_{jk}[ij][kl] = [jk][li]. \tag{C.2}$$

For further calculations we set $J = 1$. The ground state of an AF coupled chain can be argued to be a singlet by Marshall theorem [Auer 12]. One can construct a non-orthogonal singlet basis $\{|\sigma_1\rangle, |\sigma_2\rangle, \cdots, |\sigma_{N_D}\rangle\}$ to express the ground state whose dimension is $N_D = \frac{1}{N/2+1}\binom{N}{N/2}$ for an N-site chain. For the six-site problem, the basis is pictorially shown in Figure. C.2. The Hamiltonian in (C.1) in this basis has the following matrix form

$$\mathcal{H} = \begin{pmatrix} 0 & -1 & -1 & 0 & -1 \\ -2 & 2 & 0 & -2 & 0 \\ -2 & 0 & 2 & -2 & 0 \\ 0 & -1 & -1 & 0 & -1 \\ -2 & 0 & 0 & -2 & 2 \end{pmatrix}.$$

whose ground state energy density is $\mathcal{E}_{\text{GS}} = (1 - \sqrt{13})/6 \sim -0.4343$ being in well agreement with the ED results in chapter 6. The ground state wave function is given by

$$|\psi_{\text{GS}}\rangle = \frac{1}{4}(1 + \sqrt{13})|\sigma_1\rangle + |\sigma_2\rangle + |\sigma_3\rangle + \frac{1}{4}(1 + \sqrt{13})|\sigma_4\rangle + |\sigma_5\rangle\,. \tag{C.3}$$

It is to be noted that longer the valence bond in a basis (e.g. $|\sigma_2\rangle$, $|\sigma_3\rangle$ and $|\sigma_5\rangle$) is, lesser is its projection onto the ground state. The contribution of such long-range singlets becomes higher in the excited states. For an $N$ site kagome cluster at one-third filling, there will be $N_e = 2N/3$ electrons forming $N_l = N/9$ non-interacting loops of length six. The overall ground state wave function is, thus, an outer product of each loop and written as

$$|\Psi_0\rangle = \prod_{\otimes}^{N_l} |\psi_{\mathrm{GS}}\rangle \, . \tag{C.4}$$

# Bibliography

[Agua 08] M. Aguado and G. Vidal. "Entanglement renormalization and topological order". *Physical Review Letters*, Vol. 100, No. 7, p. 070404, 2008. 2

[Ahar 73] A. Aharony. "Critical Behavior of Anisotropic Cubic Systems". *Physical Review B*, Vol. 8, pp. 4270–4273, Nov 1973. 48

[Alet 05] F. Alet, J. L. Jacobsen, G. Misguich, V. Pasquier, F. Mila, and M. Troyer. "Interacting classical dimers on the square lattice". *Physical Review Letters*, Vol. 94, No. 23, p. 235702, 2005. 15

[Alet 06] F. Alet, Y. Ikhlef, J. L. Jacobsen, G. Misguich, and V. Pasquier. "Classical dimers with aligning interactions on the square lattice". *Physical Review E*, Vol. 74, p. 041124, Oct 2006. 15

[Amic 08] L. Amico, R. Fazio, A. Osterloh, and V. Vedral. "Entanglement in many-body systems". *Reviews of Modern Physics*, Vol. 80, No. 2, p. 517, 2008. 33

[Ande 04] P. W. Anderson, P. Lee, M. Randeria, T. Rice, N. Trivedi, and F. Zhang. "The physics behind high-temperature superconducting cuprates: the'plain vanilla'version of RVB". *Journal of Physics: Condensed Matter*, Vol. 16, No. 24, p. R755, 2004. 2

[Ande 56] P. Anderson. "Ordering and antiferromagnetism in ferrites". *Physical Review*, Vol. 102, No. 4, p. 1008, 1956. 7, 50

[Ande 73] P. W. Anderson. "Resonating valence bonds: A new kind of insulator". *Materials Research Bulletin*, Vol. 8, No. 2, pp. 153–60, 1973. v, 1, 2, 5

[Ande 87a] P. W. Anderson. "The resonating valence bond state in La2CuO4 and superconductivity". *Science*, Vol. 235, No. 4793, pp. 1196–1198, 1987. 2, 5

[Ande 87b] P. Anderson, G. Baskaran, Z. Zou, and T. Hsu. "Resonating–valence-bond theory of phase transitions and superconductivity in La 2 CuO 4-based compounds". *Physical Review Letters*, Vol. 58, No. 26, p. 2790, 1987. 2

[Ande 97] P. W. Anderson *et al. The Theory of Superconductivity in the High-Tc Cuprate Superconductors*. Vol. 446, Princeton University Press Princeton, NJ, 1997. 2

[Aria 03] J. M. Arias, J. Dukelsky, and J. E. García-Ramos. “Quantum Phase Transitions in the Interacting Boson Model: Integrability, Level Repulsion, and Level Crossing”. *Physical Review Letters*, Vol. 91, p. 162502, Oct 2003. 58

[Armi 10] N. Armitage, P. Fournier, and R. Greene. “Progress and perspectives on electron-doped cuprates”. *Reviews of Modern Physics*, Vol. 82, No. 3, p. 2421, 2010. 1

[Auer 12] A. Auerbach. *Interacting Electrons and Quantum Magnetism.* Springer Science & Business Media, 2012. 83

[Bale 02] L. Balents, M. Fisher, and S. Girvin. “Fractionalization in an easy-axis Kagome antiferromagnet”. *Physical Review B*, Vol. 65, No. 22, p. 224412, 2002. 2, 5, 27, 30, 40, 41, 43, 68

[Bale 05] L. Balents, L. Bartosch, A. Burkov, S. Sachdev, and K. Sengupta. “Competing orders and non-Landau-Ginzburg-Wilson criticality in (Bose) Mott transitions”. *Progress of Theoretical Physics Supplement*, Vol. 160, pp. 314–336, 2005. 1, 29

[Bale 10] L. Balents. “Spin liquids in frustrated magnets”. *Nature*, Vol. 464, No. 7286, pp. 199–208, 2010. 1, 5

[Bane 14] D. Banerjee, M. Bögli, C. Hofmann, F.-J. Jiang, P. Widmer, and U.-J. Wiese. “Interfaces, strings, and a soft mode in the square lattice quantum dimer model”. *Physical Review B*, Vol. 90, No. 24, p. 245143, 2014. 12

[Batc 94] M. T. Batchelor, J. Suzuki, and C. Yung. “Exact results for Hamiltonian walks from the solution of the fully packed loop model on the honeycomb lattice”. *Physical Review Letters*, Vol. 73, No. 20, p. 2646, 1994. 27

[Batc 96] M. Batchelor, H. Blöte, B. Nienhuis, and C. Yung. “Critical behaviour of the fully packed loop model on the square lattice”. *Journal of Physics A: Mathematical and General*, Vol. 29, No. 16, p. L399, 1996. 8, 27

[Baxt 82] R. Baxter. “Exactly solvable models in statistical mechanics”. 1982. 5, 7, 15

[Bedn 86] J. G. Bednorz and K. A. Müller. “Possible highT c superconductivity in the Ba- La- Cu- O system”. *Zeitschrift für Physik B Condensed Matter*, Vol. 64, No. 2, pp. 189–193, 1986. 1

[Bern 04] B. Bernu and D. Ceperley. “Multi-spin exchange model: the near melting transition of the two-dimensional Wigner crystal”. *Journal of Physics: Condensed Matter*, Vol. 16, No. 11, p. S701, 2004. 30

[Bern 92] B. Bernu, C. Lhuillier, and L. Pierre. “Signature of Néel order in exact spectra of quantum antiferromagnets on finite lattices”. *Physical Review Letters*, Vol. 69, pp. 2590–2593, Oct 1992. 58

[Blan 84a] D. Blankschtein, M. Ma, and A. N. Berker. “Fully and partially frustrated simple-cubic Ising models: Landau-Ginzburg-Wilson theory”. *Physical Review B*, Vol. 30, pp. 1362–1365, Aug 1984. 45

[Blan 84b] D. Blankschtein, M. Ma, A. N. Berker, G. S. Grest, and C. Soukoulis. “Orderings of a stacked frustrated triangular system in three dimensions”. *Physical Review B*, Vol. 29, No. 9, p. 5250, 1984. 45

[Blot 89] H. Blote and B. Nienhuis. “Critical behaviour and conformal anomaly of the O (n) model on the square lattice”. *Journal of Physics A: Mathematical and General*, Vol. 22, No. 9, p. 1415, 1989. 27

[Blot 94] H. Blöte and B. Nienhuis. “Fully packed loop model on the honeycomb lattice”. *Physical Review Letters*, Vol. 72, No. 9, p. 1372, 1994. 27

[Bran 76] B. Brandow. “Theory of mott insulators”. *International Journal of Quantum Chemistry*, Vol. 10, No. S10, pp. 417–434, 1976. 1

[Brez 74] E. Brézin, J. Le Guillou, and J. Zinn-Justin. “Discussion of critical phenomena for general n-vector models”. *Physical Review B*, Vol. 10, No. 3, p. 892, 1974. 48

[Cana 00] B. Canals and C. Lacroix. “Quantum spin liquid: The Heisenberg antiferromagnet on the three-dimensional pyrochlore lattice”. *Physical Review B*, Vol. 61, No. 2, p. 1149, 2000. 6

[Cana 98] B. Canals and C. Lacroix. “Pyrochlore antiferromagnet: A three-dimensional quantum spin liquid”. *Physical Review Letters*, Vol. 80, No. 13, p. 2933, 1998. 6

[Cast 08] C. Castelnovo, R. Moessner, and S. L. Sondhi. “Magnetic monopoles in spin ice”. *Nature*, Vol. 451, No. 7174, pp. 42–45, 2008. 5

[Cast 12] C. Castelnovo, R. Moessner, and S. Sondhi. “Spin ice, fractionalization and topological order”. *Annual Review of Condensed Matter Physics*, Vol. 3, pp. 35–55, 2012. 6

[Chen 14] G. Chen, H.-Y. Kee, and Y. B. Kim. “Spin susceptibility anomaly in cluster Mott insulators on a partially-filled anisotropic Kagome lattice: applications to LiZn2Mo3O8”. *arXiv preprint arXiv:1408.1963*, 2014. 69

[Chen 15] G. Chen, H.-Y. Kee, and Y. Kim. “Cluster Mott insulator and two Curie-Weiss regimes on an anisotropic Kagome lattice”. *arXiv preprint arXiv:1504.01396*, 2015. 69

[Cira 11] J. I. Cirac, D. Poilblanc, N. Schuch, and F. Verstraete. “Entanglement spectrum and boundary theories with projected entangled-pair states”. *Physical Review B*, Vol. 83, p. 245134, Jun 2011. 34

[Depe 12] S. Depenbrock, I. P. McCulloch, and U. Schollwoeck. “Nature of the spin-liquid ground state of the s= 1/2 Heisenberg model on the kagome lattice”. *Physical Review Letters*, Vol. 109, No. 6, p. 067201, 2012. 2, 13

[Diep 04] H. T. Diep. *Frustrated Spin Systems*. World Scientific, 2004. 5

[Eise 10] J. Eisert, M. Cramer, and M. B. Plenio. “Colloquium: Area laws for the entanglement entropy”. *Reviews of Modern Physics*, Vol. 82, No. 1, p. 277, 2010. 2, 33

[F Ve 04] J. I. C. F. Verstraete. “Renormalization algorithms for Quantum-Many Body Systems in two and higher dimensionsn”. *arXiv:cond-mat/0407066*, 2004. 15

[Faze 99] P. Fazekas. “Electron Correlation and Magnetism”. *Lecture Notes in Physics*, Vol. 5, p. 650, 1999. 57, 83

[Fend 02] P. Fendley, R. Moessner, and S. L. Sondhi. “Classical dimers on the triangular lattice”. *Physical Review B*, Vol. 66, p. 214513, Dec 2002. v, 15, 19, 30, 67, 77, 78, 79

[Ferh 14] K. Ferhat and A. Ralko. “Phase diagram of the $\frac{1}{3}$-filled extended Hubbard model on the kagome lattice”. *Physical Review B*, Vol. 89, p. 155141, Apr 2014. 10

[Fish 61] M. Fisher. “Statistical mechanics of dimers on a plane lattice”. *Physical Review*, Vol. 124, No. 6, pp. 1664–1672, 1961. 15

[Fish 63] M. E. Fisher and J. Stephenson. “Statistical mechanics of dimers on a plane lattice. II. Dimer correlations and monomers”. *Physical Review*, Vol. 132, No. 4, p. 1411, 1963. 51

[Fish 89] M. P. A. Fisher, P. B. Weichman, G. Grinstein, and D. S. Fisher. “Boson localization and the superfluid-insulator transition”. *Physical Review B*, Vol. 40, pp. 546–570, Jul 1989. 1

[Frad 13] E. Fradkin. *Field Theories of Condensed Matter Physics*. Cambridge University Press, 2013. 2, 13, 39

[Frad 90] E. Fradkin and S. Kivelson. “Short range resonating valence bond theories and superconductivity”. *Modern Physics Letters B*, Vol. 4, No. 03, pp. 225–232, 1990. 13

[Fuld 02] P. Fulde, K. Penc, and N. Shannon. “Fractional charges in pyrochlore lattices”. *Annalen der Physik*, Vol. 11, No. 12, pp. 892–900, 2002. 6

[Furu 07] S. Furukawa and G. Misguich. “Topological entanglement entropy in the quantum dimer model on the triangular lattice”. *Physical Review B*, Vol. 75, No. 21, p. 214407, 2007. 34

[Gu 08] Z.-C. Gu, M. Levin, and X.-G. Wen. “Tensor-entanglement renormalization group approach as a unified method for symmetry breaking and topological phase transitions”. *Physical Review B*, Vol. 78, p. 205116, Nov 2008. 3, 17

[Han 12] T.-H. Han, J. S. Helton, S. Chu, D. G. Nocera, J. A. Rodriguez-Rivera, C. Broholm, and Y. S. Lee. “Fractionalized excitations in the spin-liquid state of a kagome-lattice antiferromagnet”. *Nature*, Vol. 492, No. 7429, pp. 406–410, 2012. 13

[Heid 05] D. Heidarian and K. Damle. “Persistent supersolid phase of hard-core bosons on the triangular lattice”. *Physical Review Letters*, Vol. 95, No. 12, p. 127206, 2005. 27

[Henl 04] C. L. Henley. “From classical to quantum dynamics at Rokhsar–Kivelson points”. *Journal of Physics: Condensed Matter*, Vol. 16, No. 11, p. S891, 2004. 11

[Henl 89] C. L. Henley. “Ordering due to disorder in a frustrated vector antiferromagnet”. *Physical Review Letters*, Vol. 62, No. 17, p. 2056, 1989. 5

[Henl 97] C. L. Henley. “Relaxation time for a dimer covering with height representation”. *Journal of Statistical Physics*, Vol. 89, No. 3-4, pp. 483–507, 1997. 11

[Herm 04] M. Hermele, M. P. A. Fisher, and L. Balents. “Pyrochlore photons: The $U(1)$ spin liquid in a $S = \frac{1}{2}$ three-dimensional frustrated magnet”. *Physical Review B*, Vol. 69, p. 064404, Feb 2004. 6

[Huh 11] Y. Huh, M. Punk, and S. Sachdev. “Vison states and confinement transitions of Z 2 spin liquids on the kagome lattice”. *Physical Review B*, Vol. 84, No. 9, p. 094419, 2011. 47

[Inde 06] M. Indergand, A. Läuchli, S. Capponi, and M. Sigrist. “Modeling bond-order wave instabilities in doped frustrated antiferromagnets: Valence bond solids at fractional filling”. *Physical Review B*, Vol. 74, p. 064429, Aug 2006. 57

[Isak 06a] S. V. Isakov, S. Wessel, R. G. Melko, K. Sengupta, and Y. B. Kim. “Hard-Core Bosons on the Kagome Lattice: Valence-Bond Solids and Their Quantum Melting”. *Physical Review Letters*, Vol. 97, p. 147202, 2006. 27, 28

[Isak 06b] S. Isakov, Y. B. Kim, and A. Paramekanti. “Spin-liquid phase in a spin-1/2 quantum magnet on the kagome lattice”. *Physical Review Letters*, Vol. 97, No. 20, p. 207204, 2006. 27

[Isak 11] S. V. Isakov, M. B. Hastings, and R. G. Melko. “Topological entanglement entropy of a Bose-Hubbard spin liquid”. *Nature Physics*, Vol. 7, No. 10, pp. 772–775, 2011. 34

[Isak 12] S. V. Isakov, R. G. Melko, and M. B. Hastings. “Universal signatures of fractionalized quantum critical points”. *Science*, Vol. 335, No. 6065, pp. 193–195, 2012. 48

[Ivan 04] D. Ivanov. “Vortexlike elementary excitations in the Rokhsar-Kivelson dimer model on the triangular lattice”. *Physical Review B*, Vol. 70, No. 9, p. 094430, 2004. 42

[Jack 76] R. Jackiw and C. Rebbi. “Solitons with fermion number 1/2”. *Physical Review D*, Vol. 13, No. 12, p. 3398, 1976. 6

[Jaub 11] L. Jaubert, M. Haque, and R. Moessner. “Analysis of a fully packed loop model arising in a magnetic Coulomb phase”. *Physical Review Letters*, Vol. 107, No. 17, p. 177202, 2011. 27

[Jian 08] H. C. Jiang, Z. Y. Weng, and T. Xiang. “Accurate Determination of Tensor Network State of Quantum Lattice Models in Two Dimensions”. *Physical Review Letters*, Vol. 101, p. 090603, Aug 2008. 18

[Jian 12] H.-C. Jiang, Z. Wang, and L. Balents. “Identifying topological order by entanglement entropy”. *Nature Physics*, Vol. 8, No. 12, pp. 902–905, 2012. 2, 34

[Jian 13] H.-C. Jiang, R. R. Singh, and L. Balents. “Accuracy of topological entanglement entropy on finite cylinders”. *Physical Review Letters*, Vol. 111, No. 10, p. 107205, 2013. 34

[Kast 61] P. Kasteleyn. “The statistics of dimers on a lattice. I. The number of dimer arrangements on a quadratic lattice”. *Physica*, Vol. 27, No. 12, pp. 1209–1225, 1961. v, 15, 75

[Kawa 84] H. Kawamura. “Spin-Wave Analysis of the Antiferromagnetic Plane Rotator Model on the Triangular Lattice–Symmetry Breaking in a Magnetic Field”. *Journal of the Physical Society of Japan*, Vol. 53, No. 8, pp. 2452–2455, 1984. 5

[Ketl 73] I. Ketley and D. Wallace. “A modified epsilon expansion for a Hamiltonian with cubic point-group symmetry”. *Journal of Physics A: Mathematical, Nuclear and General*, Vol. 6, No. 11, p. 1667, 1973. 48

[Kita 03] A. Y. Kitaev. “Fault-tolerant quantum computation by anyons”. *Annals of Physics*, Vol. 303, No. 1, pp. 2–30, 2003. 13

[Kita 06] A. Kitaev and J. Preskill. “Topological entanglement entropy”. *Physical Review Letters*, Vol. 96, No. 11, p. 110404, 2006. 2, 33

[Kive 87] S. A. Kivelson, D. S. Rokhsar, and J. P. Sethna. “Topology of the resonating valence-bond state: Solitons and high-T c superconductivity”. *Physical Review B*, Vol. 35, No. 16, p. 8865, 1987. 2, 5

[Klei 95] H. Kleinert and V. Schulte-Frohlinde. “Exact five-loop renormalization group functions of $\theta$ 4-theory with O (N)-symmetric and cubic interactions. Critical exponents up to Ïţ 5”. *Physics Letters B*, Vol. 342, No. 1, pp. 284–296, 1995. 48

[Kogu 79] J. B. Kogut. “An introduction to lattice gauge theory and spin systems”. *Reviews of Modern Physics*, Vol. 51, No. 4, p. 659, 1979. 28

[Kond 95] J. Kondev and C. L. Henley. “Four-coloring model on the square lattice: A critical ground state”. *Physical Review B*, Vol. 52, No. 9, p. 6628, 1995. 27

[Land 80] L. L. D. Landau and E. E. M. Lifshits. *Statistical Physics*. Vol. 5, Butterworth-Heinemann, 1980. 11, 39, 48

[Laug 83] R. B. Laughlin. “Anomalous quantum Hall effect: an incompressible quantum fluid with fractionally charged excitations”. *Physical Review Letters*, Vol. 50, No. 18, p. 1395, 1983. 5, 6

[Laug 88] R. Laughlin. “The relationship between high-temperature superconductivity and the fractional quantum Hall effect”. *Science*, Vol. 242, No. 4878, pp. 525–533, 1988. 5

[Leun 96] P. Leung, K. Chiu, and K. J. Runge. “Columnar dimer and plaquette resonating-valence-bond orders in the quantum dimer model”. *Physical Review B*, Vol. 54, No. 18, p. 12938, 1996. 11, 12

[Levi 06] M. Levin and X.-G. Wen. “Detecting topological order in a ground state wave function”. *Physical Review Letters*, Vol. 96, No. 11, p. 110405, 2006. 2, 33

[Levi 07] M. Levin and C. P. Nave. “Tensor Renormalization Group Approach to Two-Dimensional Classical Lattice Models”. *Physical Review Letters*, Vol. 99, p. 120601, Sep 2007. 3, 16, 17

[Li 08] H. Li and F. D. M. Haldane. “Entanglement spectrum as a generalization of entanglement entropy: Identification of topological order in non-abelian fractional quantum hall effect states”. *Physical Review Letters*, Vol. 101, No. 1, p. 010504, 2008. 2

[Lieb 62] E. Lieb and D. Mattis. “Ordering energy levels of interacting spin systems”. *Journal of Mathematical Physics*, Vol. 3, No. 4, pp. 749–751, 1962. 58

[Lieb 67] E. H. Lieb. “Exact solution of the problem of the entropy of two-dimensional ice”. *Physical Review Letters*, Vol. 18, No. 17, p. 692, 1967. 7

[Ma 00] S.-K. Ma. *Modern Theory of Critical Phenomena*. Da Capo Press, 2000. 11, 16, 39, 48

[Miel 92] A. Mielke. “Exact ground states for the Hubbard model on the Kagome lattice”. *Journal of Physics A: Mathematical and General*, Vol. 25, No. 16, p. 4335, 1992. 52

[Miel 93] A. Mielke and H. Tasaki. “Ferromagnetism in the Hubbard model”. *Communications in Mathematical Physics*, Vol. 158, No. 2, pp. 341–371, 1993. 52

[Milo 89] M. Milovanovic, S. Sachdev, and R. Bhatt. “Effective field theory of local moment formation in disordered metals”. *Physical Review Letters*, Vol. 63, pp. 82–85, 1989. 1

[Misg 02] G. Misguich, D. Serban, and V. Pasquier. “Quantum dimer model on the kagome lattice: Solvable dimer-liquid and ising gauge theory”. *Physical Review Letters*, Vol. 89, No. 13, p. 137202, 2002. 27

[Misg 08] G. Misguich and F. Mila. “Quantum dimer model on the triangular lattice: Semiclassical and variational approaches to vison dispersion and condensation”. *Physical Review B*, Vol. 77, No. 13, p. 134421, 2008. v, 2

[Moes 01a] R. Moessner and S. L. Sondhi. “Resonating Valence Bond Phase in the Triangular Lattice Quantum Dimer Model”. *Physical Review Letters*, Vol. 86, pp. 1881–1884, Feb 2001. v, vi, 1, 2, 3, 12, 13, 15, 27, 31, 32, 36

[Moes 01b] R. Moessner, S. L. Sondhi, and P. Chandra. “Phase diagram of the hexagonal lattice quantum dimer model”. *Physical Review B*, Vol. 64, p. 144416, Sep 2001. 8, 12, 53, 57

[Moes 01c] R. Moessner, S. L. Sondhi, and E. Fradkin. “Short-ranged resonating valence bond physics, quantum dimer models, and Ising gauge theories”. *Physical Review B*, Vol. 65, No. 2, p. 024504, 2001. 2, 5, 13, 39

[Moes 03] R. Moessner and S. L. Sondhi. “Three-dimensional resonating-valence-bond liquids and their excitations”. *Physical Review B*, Vol. 68, p. 184512, Nov 2003. 6

[Moes 98] R. Moessner and J. Chalker. “Properties of a classical spin liquid: the Heisenberg pyrochlore antiferromagnet”. *Physical Review Letters*, Vol. 80, No. 13, p. 2929, 1998. 5

[Mott 49] N. F. Mott. “The basis of the electron theory of metals, with special reference to the transition metals”. *Proceedings of the Physical Society. Section A*, Vol. 62, No. 7, p. 416, 1949. 1

[Muld 10] A. Mulder, R. Ganesh, L. Capriotti, and A. Paramekanti. “Spiral order by disorder and lattice nematic order in a frustrated Heisenberg antiferromagnet on the honeycomb lattice”. *Physical Review B*, Vol. 81, No. 21, p. 214419, 2010. 28

[Newm] E. Newman and G. Barkema. *Monte Carlo Methods in Statistical Physics*. 20, 21

[Nish 10] S. Nishimoto, M. Nakamura, A. O'Brien, and P. Fulde. "Metal-insulator transition of fermions on a kagome lattice at 1/3 filling". *Physical Review Letters*, Vol. 104, No. 19, p. 196401, 2010. 8

[OBri 10] A. O'Brien, F. Pollmann, and P. Fulde. "Strongly correlated fermions on a kagome lattice". *Physical Review B*, Vol. 81, No. 23, p. 235115, 2010. 8, 51

[Orus 09] R. Orús and G. Vidal. "Simulation of two-dimensional quantum systems on an infinite lattice revisited: Corner transfer matrix for tensor contraction". *Physical Review B*, Vol. 80, p. 094403, Sep 2009. 17

[Orus 14] R. Orús. "A practical introduction to tensor networks: Matrix product states and projected entangled pair states". *Annals of Physics*, Vol. 349, pp. 117–158, 2014. 16, 34

[Para 02] A. Paramekanti, L. Balents, and M. P. Fisher. "Ring exchange, the exciton Bose liquid, and bosonization in two dimensions". *Physical Review B*, Vol. 66, No. 5, p. 054526, 2002. 30

[Paul 35] L. Pauling. "The structure and entropy of ice and of other crystals with some randomness of atomic arrangement". *Journal of the American Chemical Society*, Vol. 57, No. 12, pp. 2680–2684, 1935. 30

[Penc 96] K. Penc, H. Shiba, F. Mila, and T. Tsukagoshi. "Ferromagnetism in multiband Hubbard models: From weak to strong Coulomb repulsion". *Physical Review B*, Vol. 54, pp. 4056–4067, Aug 1996. 52

[Plak 10] N. Plakida. *High-Temperature Cuprate Superconductors: Experiment, Theory, and Applications*. Vol. 166, Springer Science & Business Media, 2010. 1

[Poil 07] D. Poilblanc, K. Penc, and N. Shannon. "Doped singlet-pair crystal in the Hubbard model on the checkerboard lattice". *Physical Review B*, Vol. 75, p. 220503, Jun 2007. 6, 8, 10, 11, 56

[Poll 06] F. Pollmann and P. Fulde. "On confined fractional charges: A simple model". *EPL (Europhysics Letters)*, Vol. 75, No. 1, p. 133, 2006. 7

[Poll 07] F. Pollmann, J. J. Betouras, E. Runge, and P. Fulde. "Charge degrees in the quarter-filled checkerboard lattice". *Journal of Magnetism and Magnetic Materials*, Vol. 310, No. 2, pp. 966–968, 2007. 7

[Poll 08] F. Pollmann, P. Fulde, and K. Shtengel. "Kinetic Ferromagnetism on a Kagome Lattice". *Physical Review Letters*, Vol. 100, p. 136404, Apr 2008. 6, 10, 52, 56

[Poll 11] F. Pollmann, J. J. Betouras, K. Shtengel, and P. Fulde. "Fermionic quantum dimer and fully-packed loop models on the square lattice". *Physical Review B*, Vol. 83, No. 15, p. 155117, 2011. 69

[Poll 14] F. Pollmann, K. Roychowdhury, C. Hotta, and K. Penc. “Interplay of charge and spin fluctuations of strongly interacting electrons on the kagome lattice”. *Physical Review B*, Vol. 90, p. 035118, Jul 2014. 3, 10

[Poly 77] A. M. Polyakov. “Quark confinement and topology of gauge theories”. *Nuclear Physics B*, Vol. 120, No. 3, pp. 429–458, 1977. 2

[Powa 13] M. Powalski, K. Coester, R. Moessner, and K. P. Schmidt. “Disorder by disorder and flat bands in the kagome transverse field Ising model”. *Physical Review B*, Vol. 87, p. 054404, Feb 2013. 30

[Prio 01] D. J. Priour, M. P. Gelfand, and S. L. Sondhi. “Disorder from disorder in a strongly frustrated transverse-field Ising chain”. *Physical Review B*, Vol. 64, p. 134424, Sep 2001. 30

[Punk 15] M. Punk, A. Allais, and S. Sachdev. “A quantum dimer model for the pseudogap metal”. *arXiv preprint arXiv:1501.00978*, 2015. 69

[Ralk 05] A. Ralko, M. Ferrero, F. Becca, D. Ivanov, and F. Mila. “Zero-temperature properties of the quantum dimer model on the triangular lattice”. *Physical Review B*, Vol. 71, No. 22, p. 224109, 2005. v, 2, 12, 13, 15, 31

[Ralk 08] A. Ralko, D. Poilblanc, and R. Moessner. “Generic Mixed Columnar-Plaquette Phases in Rokhsar-Kivelson Models”. *Physical Review Letters*, Vol. 100, p. 037201, Jan 2008. 57

[Rami 08] A. P. Ramirez. “Quantum spin liquids: A flood or a trickle?”. *Nature Physics*, Vol. 4, No. 6, pp. 442–443, 2008. 5

[Read 89] N. Read and B. Chakraborty. “Statistics of the excitations of the resonating-valence-bond state”. *Physical Review B*, Vol. 40, No. 10, p. 7133, 1989. 13, 28

[Rokh 88] D. S. Rokhsar and S. A. Kivelson. “Superconductivity and the Quantum Hard-Core Dimer Gas”. *Physical Review Letters*, Vol. 61, pp. 2376–2379, Nov 1988. v, 1, 2, 8, 11, 27, 31, 53

[Romm 97] S. Rommer and S. Östlund. “Class of ansatz wave functions for one-dimensional spin systems and their relation to the density matrix renormalization group”. *Physical Review B*, Vol. 55, No. 4, p. 2164, 1997. 16

[Royc 15a] K. Roychowdhury, S. Bhattacharjee, and F. Pollmann. “Z2 topological liquid of hard-core bosons on a kagome lattice at 1/3 filling”. *arXiv preprint arXiv:1505.05998*, 2015. 3, 13

[Royc 15b] K. Roychowdhury and C.-Y. Huang. “Tensor renormalization group approach to classical dimer models”. *Physical Review B*, Vol. 91, p. 205418, May 2015. 3

[Rung 04] E. Runge and P. Fulde. “Charge degrees of freedom in frustrated lattice structures”. *Physical Review B*, Vol. 70, p. 245113, Dec 2004. 6, 7, 30

[Sach 07] S. Sachdev. *Quantum Phase Transitions*. Wiley Online Library, 2007. 58

[Sach 08] S. Sachdev. “Quantum magnetism and criticality”. *Nature Physics*, Vol. 4, No. 3, pp. 173–185, 2008. 2

[Sach 89] S. Sachdev. “Spin-Peierls ground states of the quantum dimer model: A finite-size study”. *Physical Review B*, Vol. 40, No. 7, p. 5204, 1989. 11

[Sach 92] S. Sachdev. “Kagomé-and triangular-lattice Heisenberg antiferromagnets: Ordering from quantum fluctuations and quantum-disordered ground states with unconfined bosonic spinons”. *Physical Review B*, Vol. 45, No. 21, p. 12377, 1992. 2

[Sand 07] A. W. Sandvik. “Evidence for deconfined quantum criticality in a two-dimensional Heisenberg model with four-spin interactions”. *Physical Review Letters*, Vol. 98, No. 22, p. 227202, 2007. 48

[Sent 00] T. Senthil and M. P. Fisher. “Z2 gauge theory of electron fractionalization in strongly correlated systems”. *Physical Review B*, Vol. 62, No. 12, p. 7850, 2000. 39

[Sent 01] T. Senthil and M. P. A. Fisher. “Fractionalization in the Cuprates: Detecting the Topological Order”. *Physical Review Letters*, Vol. 86, pp. 292–295, Jan 2001. 5, 13, 28

[Sent 04] T. Senthil, A. Vishwanath, L. Balents, S. Sachdev, and M. P. Fisher. “Deconfined quantum critical points”. *Science*, Vol. 303, No. 5663, pp. 1490–1494, 2004. 5, 28

[Shan 04] N. Shannon, G. Misguich, and K. Penc. “Cyclic exchange, isolated states, and spinon deconfinement in an X X Z Heisenberg model on the checkerboard lattice”. *Physical Review B*, Vol. 69, No. 22, p. 220403, 2004. 27

[Shas 81] B. S. Shastry and B. Sutherland. “Exact ground state of a quantum mechanical antiferromagnet”. *Physica B+C*, Vol. 108, No. 1, pp. 1069–1070, 1981. 5

[Shec 12] J. P. Sheckelton, J. R. Neilson, D. G. Soltan, and T. M. McQueen. “Possible valence-bond condensation in the frustrated cluster magnet LiZn2Mo3O8”. *Nature Materials*, Vol. 11, No. 6, pp. 493–496, 2012. 69

[Shen 05] D. Sheng and L. Balents. “Numerical evidences of fractionalization in an easy-axis two-spin Heisenberg antiferromagnet”. *Physical Review Letters*, Vol. 94, No. 14, p. 146805, 2005. 2, 27, 32

[Shen 82] E. F. Shender. *Soviet Physics Journal of Experimental and Theoretical Physics*, Vol. 56, p. 178, 1982. 30

[Shi 06] Y.-Y. Shi, L.-M. Duan, and G. Vidal. “Classical simulation of quantum many-body systems with a tree tensor network”. *Physical Review A*, Vol. 74, p. 022320, Aug 2006. 15

[Slag 14] K. Slagle and C. Xu. “Quantum phase transition between the Z 2 spin liquid and valence bond crystals on a triangular lattice”. *Physical Review B*, Vol. 89, No. 10, p. 104418, 2014. 39

[Stru 11] G. Strübi and D. A. Ivanov. “Vison excitations in near-critical quantum dimer models”. *EPL (Europhysics Letters)*, Vol. 94, No. 5, p. 57003, 2011. 42

[Su 79] W. Su, J. Schrieffer, and A. J. Heeger. “Solitons in polyacetylene”. *Physical Review Letters*, Vol. 42, No. 25, p. 1698, 1979. 5, 6

[Sylj 06] O. F. Syljuåsen. “Plaquette phase of the square-lattice quantum dimer model: Quantum Monte Carlo calculations”. *Physical Review B*, Vol. 73, p. 245105, Jun 2006. 12

[The ] The GAP Group. “GAP–Groups, Algorithms, and Programming, Version 4.7.5; 2014”. (http://www.gap-system.org/gap.html). 47

[Thou 65] D. Thouless. “Exchange in solid 3He and the Heisenberg Hamiltonian”. *Proceedings of the Physical Society*, Vol. 86, No. 5, p. 893, 1965. 30

[Trou 08] F. Trousselet, D. Poilblanc, and R. Moessner. “Mixed columnar-plaquette crystal of correlated fermions on the two-dimensional pyrochlore lattice at fractional filling”. *Physical Review B*, Vol. 78, No. 19, p. 195101, 2008. 6, 8

[Tsui 82] D. C. Tsui, H. L. Stormer, and A. C. Gossard. “Two-dimensional magnetotransport in the extreme quantum limit”. *Physical Review Letters*, Vol. 48, No. 22, p. 1559, 1982. 6

[Vann 77] J. Vannimenus and G. Toulouse. “Theory of the frustration effect. II. Ising spins on a square lattice”. *Journal of Physics C: Solid State Physics*, Vol. 10, No. 18, p. L537, 1977. 5

[Vers 02] F. Verstraete, J. Dehaene, B. De Moor, and H. Verschelde. “Four qubits can be entangled in nine different ways”. *Physical Review A*, Vol. 65, No. 5, p. 052112, 2002. 15

[Vers 04] F. Verstraete and J. I. Cirac. “Renormalization algorithms for quantum-many body systems in two and higher dimensions”. *arXiv preprint cond-mat/0407066*, 2004. 34

[Vida 07] G. Vidal. “Entanglement Renormalization”. *Physical Review Letters*, Vol. 99, p. 220405, Nov 2007. 15

[Vida 08] G. Vidal. “Class of Quantum Many-Body States That Can Be Efficiently Simulated”. *Physical Review Letters*, Vol. 101, p. 110501, Sep 2008. 15

[Vill 79] J. Villain. “Insulating spin glasses”. *Zeitschrift für Physik B Condensed Matter*, Vol. 33, No. 1, pp. 31–42, 1979. 5

[Vill 80] J. Villain, R. Bidaux, J.-P. Carton, and R. Conte. “Order as an effect of disorder”. *Journal de Physique*, Vol. 41, No. 11, pp. 1263–1272, 1980. 5, 30

[Wann 73] G. Wannier. “Antiferromagnetism. the triangular ising net”. *Physical Review B*, Vol. 7, No. 11, p. 5017, 1973. 5

[Wen 02] X.-G. Wen. “Quantum orders and symmetric spin liquids”. *Physical Review B*, Vol. 65, No. 16, p. 165113, 2002. 2

[Wen 04] X.-G. Wen. *Quantum field theory of many-body systems from the origin of sound to an origin of light and electrons*. Vol. 1, 2004. 13

[Wen 10] J. Wen, A. Rüegg, C.-C. J. Wang, and G. A. Fiete. “Interaction-driven topological insulators on the kagome and the decorated honeycomb lattices”. *Physical Review B*, Vol. 82, p. 075125, Aug 2010. 57

[Wen 89] X.-G. Wen. “Vacuum degeneracy of chiral spin states in compactified space”. *Physical Review B*, Vol. 40, No. 10, p. 7387, 1989. 11

[Wen 90a] X. G. Wen and Q. Niu. “Ground-state degeneracy of the fractional quantum Hall states in the presence of a random potential and on high-genus Riemann surfaces”. *Physical Review B*, Vol. 41, pp. 9377–9396, May 1990. 5, 11

[Wen 90b] X.-G. Wen. “Chiral Luttinger liquid and the edge excitations in the fractional quantum Hall states”. *Physical Review B*, Vol. 41, No. 18, p. 12838, 1990. 11

[Wen 90c] X.-G. Wen. “Topological orders in rigid states”. *International Journal of Modern Physics B*, Vol. 4, No. 02, pp. 239–271, 1990. 2, 5, 8, 11, 13

[Wen 91] X. G. Wen. “Mean-field theory of spin-liquid states with finite energy gap and topological orders”. *Physical Review B*, Vol. 44, pp. 2664–2672, Aug 1991. 2, 5, 8

[Woyn 87] F. Woynarovich and H.-P. Eckle. “Finite-size corrections and numerical calculations for long spin 1/2 Heisenberg chains in the critical region”. *Journal of Physics A: Mathematical and General*, Vol. 20, No. 2, p. L97, 1987. 56

[Yan 11] S. Yan, D. A. Huse, and S. R. White. “Spin-liquid ground state of the S= 1/2 Kagome Heisenberg antiferromagnet”. *Science*, Vol. 332, No. 6034, pp. 1173–1176, 2011. 2, 13

[Zamf 02] N. V. Zamfir, P. von Brentano, R. F. Casten, and J. Jolie. “Test of two-level crossing at the $N = 90$ spherical-deformed critical point”. *Physical Review C*, Vol. 66, p. 021304, Aug 2002. 58

[Zhan 13] X.-F. Zhang, S. Eggert, *et al.* “Chiral Edge States and Fractional Charge Separation in a System of Interacting Bosons on a Kagome Lattice”. *Physical Review Letters*, Vol. 111, No. 14, p. 147201, 2013. 69

[Zhao 10] H. Zhao, Z. Xie, Q. Chen, Z. Wei, J. Cai, and T. Xiang. “Renormalization of tensor-network states”. *Physical Review B*, Vol. 81, No. 17, p. 174411, 2010. 16

# Versicherung

Hiermit versichere ich, dass ich die vorliegende Arbeit ohne unzulässige Hilfe Dritter und ohne Benutzung anderer als der angegebenen Hilfsmittel angefertigt habe; die aus fremden Quellen direkt oder indirekt übernommenen Gedanken sind als solche kenntlich gemacht. Die Arbeit wurde bisher weder im Inland noch im Ausland in gleicher oder ähnlicher Form einer anderen Prüfungsbehörde vorgelegt. Diese Arbeit wurde unter der wissenschaftlichen Betreuung von Dr. Frank Pollmann und Prof. Dr. Roderich Moessner am Max-Planck-Institut für Physik komplexer Systeme in Dresden angefertigt. Ich erkläre hiermit, dass keine früheren erfolglosen Promotionsverfahren stattgefunden haben. Ich erkenne die Promotionsordnung der Fakultät für Mathematik und Naturwissenschaften der Technische Universität Dresden an.

Dresden, 1. September 2015.